Fundamentals on the Construction and Performance of Shaped Charges

by
Prof. Dr. Manfred Held

TDW, Schrobenhausen, Bavaria, Germany

(With 34 figures in text.)

Nobel-Hefte, January–March 1991, page 14–40.

Prof. Dr. Manfred Held passed away from a sudden heart attack on the 8th of February 2011. A detailed biography is to be found at `https://apps.dtic.mil/sti/tr/pdf/ADA554529.pdf`.

Contents

List of Symbols **3**

1 Construction of a Shaped Charge, Introduction **5**
1.1 General Information 5
1.2 Theoretical Maximum Penetration Depth 5

2 Phenomenology of a Shaped Charge **7**

3 The Hydrodynamical Theory of Penetration of a Shaped Charge Jet **16**
3.1 Penetration with Constant Jet Velocity 16
3.2 Penetration of the Jet with a Velocity Gradient 21
3.2.1 Case I. Crater Base Formation with Continuous Jet 24
3.2.2 Case III. Crater Base Formation with particulated Jet 30
3.2.3 Case II. Crater Base Formation with First Continuous, then Particulated Jet 34
3.2.4 Equation matrix for selection when calculating shaped charges . . 38
3.2.5 Theoretical maximum DOP performance $\mathbf{P}_m$ 40
3.2.6 Description of Graphical Representation 40
3.2.7 Influence of Maximum Jet Tip Speed $v_{j,0}$ on the DOP Performance 42

4 Validation of the Hydrodynamical Theory of Penetration of a Shaped Charge Jet into Concrete and Sand in Comparison to Steel **44**
4.1 General Remarks 44
4.2 Experiments 50
4.2.1 Blast Experiments against Blocks of Concrete 50
4.2.2 Blast Experiments in Sand 65

5 Summary **75**

References **77**

List of Symbols

$\mathfrak{A}$	defined according to Equation 59
$\mathfrak{B}$	defined according to Equation 73
L	jet length
p_j	dynamic pressure according to the Bernoulli equation
p_T	total pressure
$\mathbf{P}$	depth-of-penetration performance or -effect, crater depth, penetration depth; or simply depth-of-penetration (DOP)
$\mathbf{P}_m$	maximum depth-of-penetration (DOP) performance or -effect, maximum crater depth
$t, t_j, t_\mathbf{P}$	time, time interval regarding jet or penetration depth
t_p	particulation time; time span, during which the jet disintegrates in small(er) particles and/or lumps
u	crater base velocity, velocity (of shaped charge jet) at tip of piercing hole
v_j	(shaped charge) jet velocity, impact velocity of jet, velocity of the tip of the jet as it contacts the target plate
$v_{j,\min}$	(shaped charge jet) minimum effective residual jet velocity
$v_{j,0}$	(shaped charge) maximum jet tip speed, velocity of the tip of the jet at the intersection of the projectile and target
$\mathcal{Z}$	distance from the virtual origin located in shaped charge to the blast object or target, respectively

γ	defined according to Equation 5
ρ_j	density of shaped charged jet
ρ_T	density of target

$_0$	final or highest state regarding impact, velocity or time
$_{1,2,3}$	numbering of target or blast object, respectively, i.e. target no. 1, target no. 2, ...
$_C$	Concrete

$_j$	(shaped charge) jet
$_S$	Sand
$_{St}$	Steel
$_T$	Target

Abstract

After a short description of the construction, design and function of a shaped charge, the formulæ for the penetration of a shaped charge jet into different materials are derived in a detailed, understandable and reproducible manner. Within the framework of the derivation the depth-of-penetration (DOP) performance **P** plays an important role in characterizing the shaped charge jet. From a table or search matrix, respectively, one can readily find the formulæ for penetration such as function of time or cratering velocity or residual jet velocity, or, inversely the formulæ for continuous and particulated jet penetration, as well as for a jet that first penetrates as a continuous and later as a particulated jet. These formulæ enable the prediction of the DOP of shaped charges in different materials. Tests with concrete and sand have demonstrated the validity of these formulæ, as well as their limitations. In this way, the phenomenon "shaped charge" can be very well (or certainly: better) understood from the analytical description of the penetration process on the basis of rather simple and fundamental physical principles.

1 Construction of a Shaped Charge, Introduction

1.1 General Information

A modern shaped charge consists of the actual explosive charge and its lining, the ignition elements and the spacer. These components are held together by a casing.

The explosive charge is usually cone-shaped towards the blast object. This cavity also gives the charge type the name "hollow out charge", or "hollow charge" for short.

1.2 Theoretical Maximum Penetration Depth

The conical chamber (6, Figure 1) with an apex angle (5) in the range of 30° to 120° is generally provided with a rotationally symmetrical lining (3) made of a ductile and heavy material, e.g. copper or tantalum with a wall thickness of e.g. 2 mm. This is referred to as a "lined hollow charge". There is always a spacer (9) in front of the cavity (6), as the distance between the charge (2) and the explosive object (6), i.e. the standoff distance, significantly determines the DOP effect or the penetration performance of the shaped charge, respectively. Shaped charges are used in both civil and military blasting technology to direct the blasting effect of a High Explosive (HE) or material, respectively, in a targeted and concentrated manner in a desired direction. Typical applications include the perforation of drill pipes and steel plates, the separation of steel girders and reinforced concrete bridge elements during demolition blasting, the tapping of blast furnaces, etc. Hollow charges also include cutting or roof loads.

For the DOP performance of a shaped charge, precise axial ignition, which takes place via corresponding transfer and booster charges, is important. If the rotational symmetry is not maintained in even just one of the four basic components, namely the ignition point (1), the explosive charge (2), the lining (3) and the casing (4), the DOP performance is significantly reduced and a more cutting effect with reduced DOP performance is obtained.

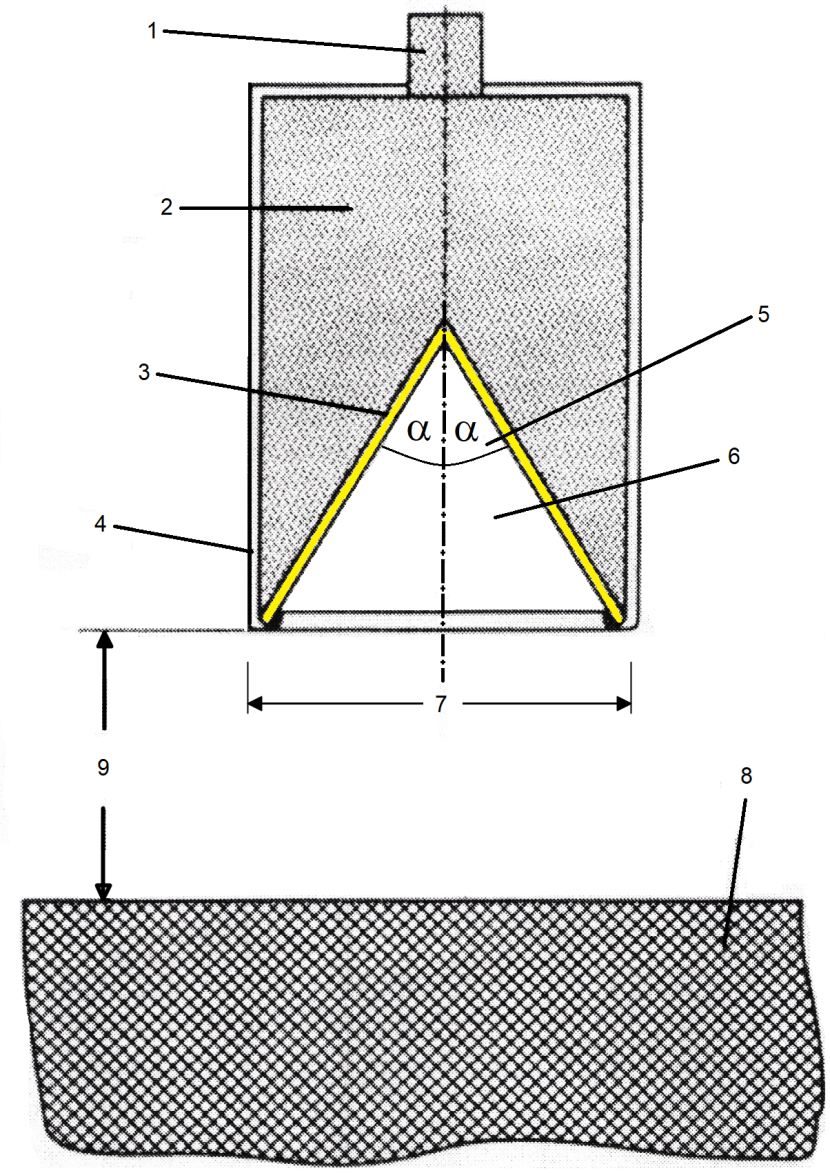

Figure 1: Shaped charge with essential construction features

1 Ignition point, Fuse, Detonator
2 Explosive charge, HE
3 Liner, liner metal
4 Casing
5 apex angle $= 2 \cdot \alpha$
6 Rotationally symmetrical, conical cavity
7 Charge diameter
8 Target, blast object
9 Distance of ignition, Standoff distance

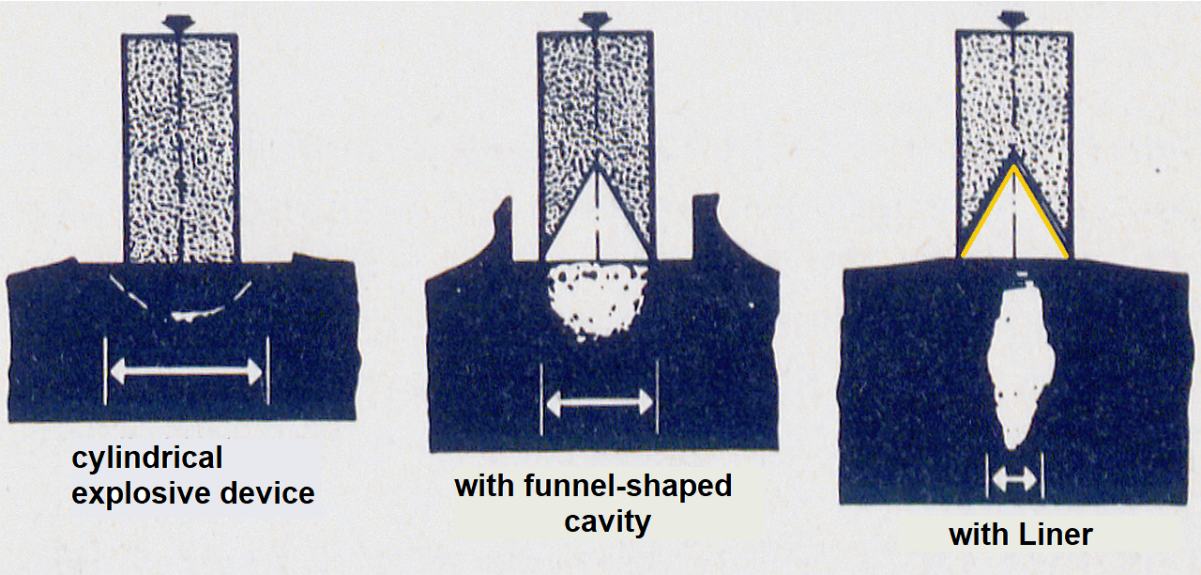

Figure 2: Morphological changes and effect on a target of a cylindrical explosive device, a cylindrical explosive device with cavity and a cylindrical explosive device with cavity and liner (lined cavity). Note the reduction in horizontal "impact area" and the increase in vertical "depth effect" from left to right

2 Phenomenology of a Shaped Charge

For an overview see also [9].
A cylindrical explosive charge placed on a steel block without spacing causes a wide, shallow indentation in the steel corresponding to the charge diameter (caliber)[1] (see Figure 2, left part). Surprisingly, a funnel-shaped cavity in the charge towards the blast object creates a depth that corresponds approximately to the charge diameter (see Figure 2, right part), [7], despite the lower total amount of explosive charge.

Especially where part of the explosive charge has been removed, a deeper, albeit smaller in diameter, cavity is created in the explosive object than with a pure pressure charge. If one compares the effect of a hollow charge with a lining (Figure 2, right part), one will find a deep hole channel of two to three times the charge diameter, but with a further reduced cross-section, [12].

Figure 7 shows the different detonation stages of a shaped charge with a lined cavity. These stages are explained in what is following. Further on Figure 3 and Figure 4 show the dependency of the apex/cone angle $2 \cdot \alpha$ on the formation of the shaped charge jet. Depending on which apex angle is selected for the design, the jet is elongated and stretched differently and exhibits a changing morphology, respectively. If one assumes the drawn relations on Figure 4 to be realistic, a statistical evaluation (see Figure 5) results in

$$\text{initial cone angel } = \text{const.} \cdot \text{length}^{-1.734}\,; \mathrm{R}^2 = 0,996\,.$$

[1]Note: In shaped charge technology, the diameter of the explosive charge (caliber) is used as a fixed value to express the distance from the explosive object and the penetration capacity of the shaped charge. One then speaks of "caliber distance" and "caliber power".

The value of the constant depends on the unit of measure of jet length.
Finally, Figure 6 shows the target section of a shaped charge after it has been blasted on the former.

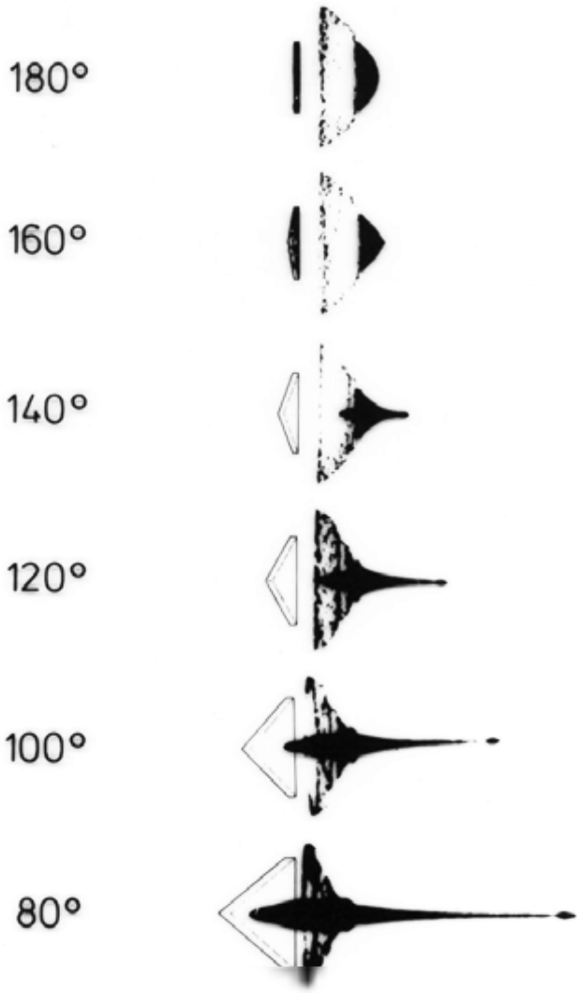

Figure 3: Different apex angles $= 2 \cdot \alpha$, left column, and corresponding characteristics of the formation of the appropriate shaped charge jet, right column

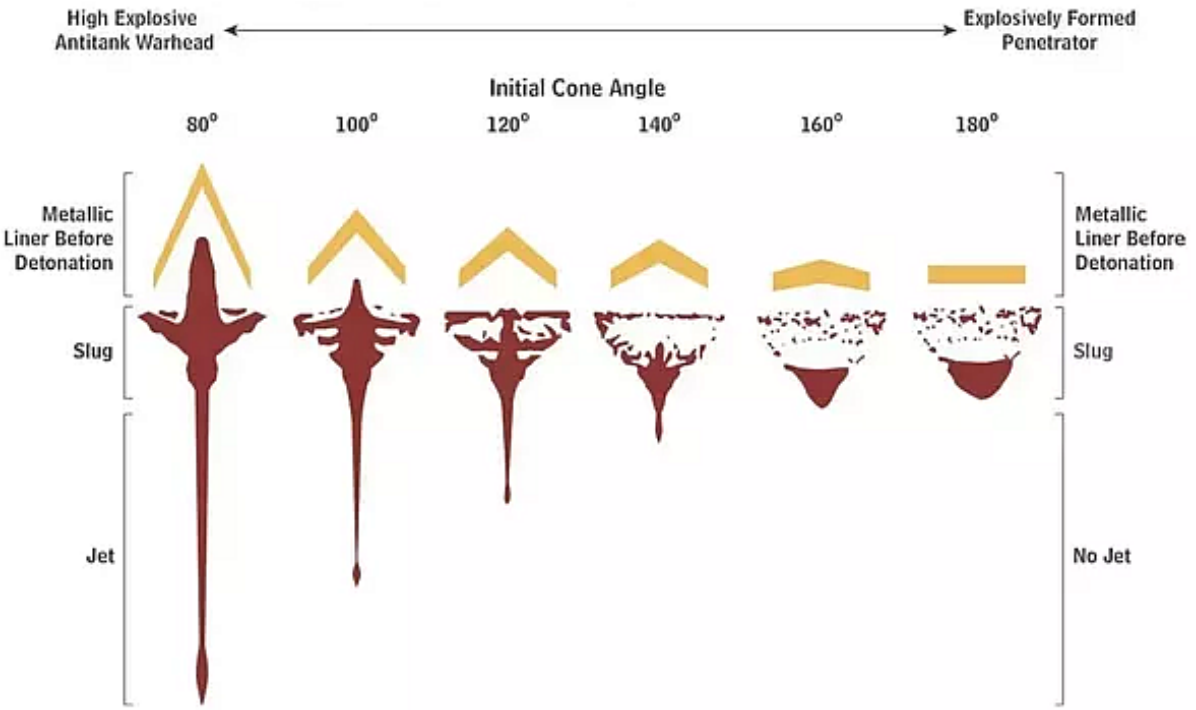

Figure 4: Effect of shaped charge cone angles on jet and slug formation analogously to Figure 3 with illustrative notes; taken from [13]

An engineer unfamiliar with shaped charge technology would, as is normally expected, also expect a smaller charge to have a smaller effect. This may be based on the assumption that: On the one hand the amount of explosive is reduced in the unlined shaped charge and the distance from the center of gravity of the explosive charge to the explosive object is increased. On the other hand the cavity is also shielded against the pressure effect by the lining material introduced. However, it is surprising that this results in an increase in the DOP effect and shows that special effects are obviously at work here. The comparison of the explosive effect of the differently formed charges shows that the formation of a cavity and the insertion of a lining obviously results in a concentration effect with increased DOP performance at the expense of the respective width effect (Figure 2).

If the time sequence of the crater formation in the material to be blasted is measured, [8], with electrical short-circuit probes, the time-to-distance diagram shown in Figure 8 is obtained. For the penetration of an approximately 600 mm thick steel plate, a time of about 350 µs is required. This means an average cratering velocity of around $1.7\,\mathrm{mm\,\mu s^{-1}}$ or $1700\,\mathrm{m\,s^{-1}}$. This astonishingly high mean crater base velocity is even about $4000\,\mathrm{m\,s^{-1}}$ at the beginning of the penetration process. These high cratering velocities show that the penetration of steel plates by means of a “hollow charge jet” cannot be a thermodynamic process, since heat conduction phenomena and melting processes cannot take place at such high velocities. On the other hand, the detonation wave front of a detonating cylindrical explosive charge of the same diameter in contact with the steel plate would only be effective for about 10 µs, [3]. This means that a shaped charge acts on the explosive object for about 35 times longer than a cylindrical charge that is only placed on top. The “concen-

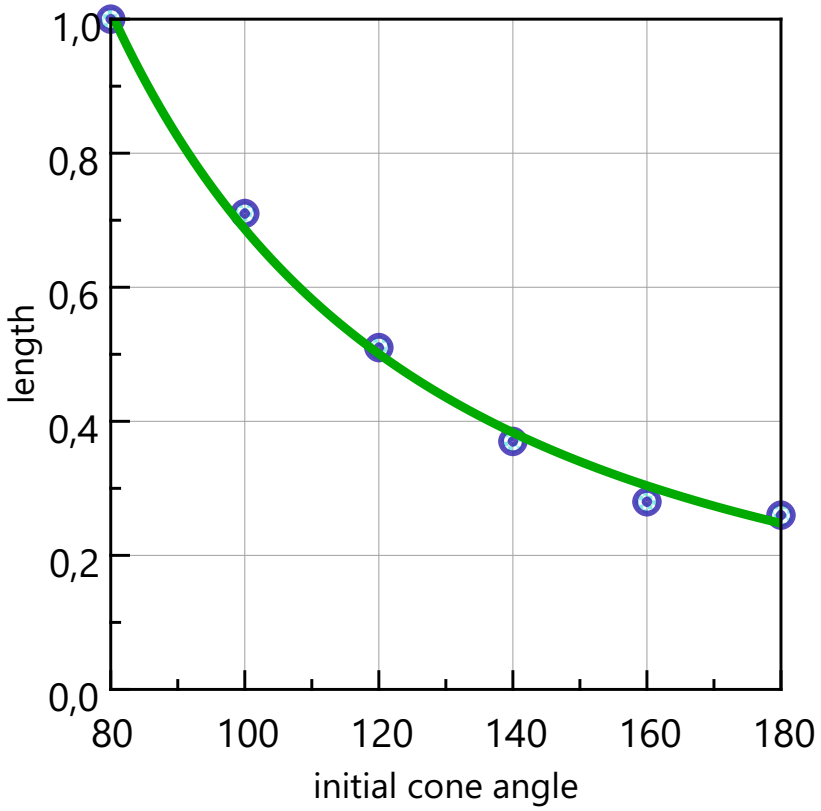

Figure 5: Evaluation of dependence of jet length from initial cone length according to plot in Figure 4. The maximum jet length at 80° was set arbitrarily to one, as only the power is significant

tration of the effect" on the one hand and the "extension of the duration of action" on the other are obviously two essential factors for the blasting performance of the shaped charge.

A third special feature is the so-called distance curve of the shaped charge (see Figure 9), [3]; with increasing distance of the shaped charge base from the blast object up to a value of four to eight times the charge diameter, the DOP performance first increases, but then decreases again. This phenomenon shows that an "effect transformer" obviously occurs here, which results in a maximum DOP effect at a certain distance.

By means of X-ray flash photography, this effect transformer can be captured and – despite the extremely bright detonation flash and the present swaths of the detonating explosive charge – the deformation of the lining and the formation of the jet can be easily followed and observed. Figure 10 shows a series of X-ray flash images with increasing time difference between the detonation of the explosive charge at the tip of the funnel and the X-ray flash triggering. The copper lining, which is accelerated towards the axis during the detonation of the explosive charge and converges along a collapse line can be clearly seen. This forms the "hollow charge jet" with 10 % to 20 % of the lining mass at peak velocities above $8000\,\mathrm{m\,s^{-1}}$ with copper as the lining material and the high-mass remainder, which has velocities of $300\,\mathrm{m\,s^{-1}}$ to $1000\,\mathrm{m\,s^{-1}}$ and is called slug or "carrot".

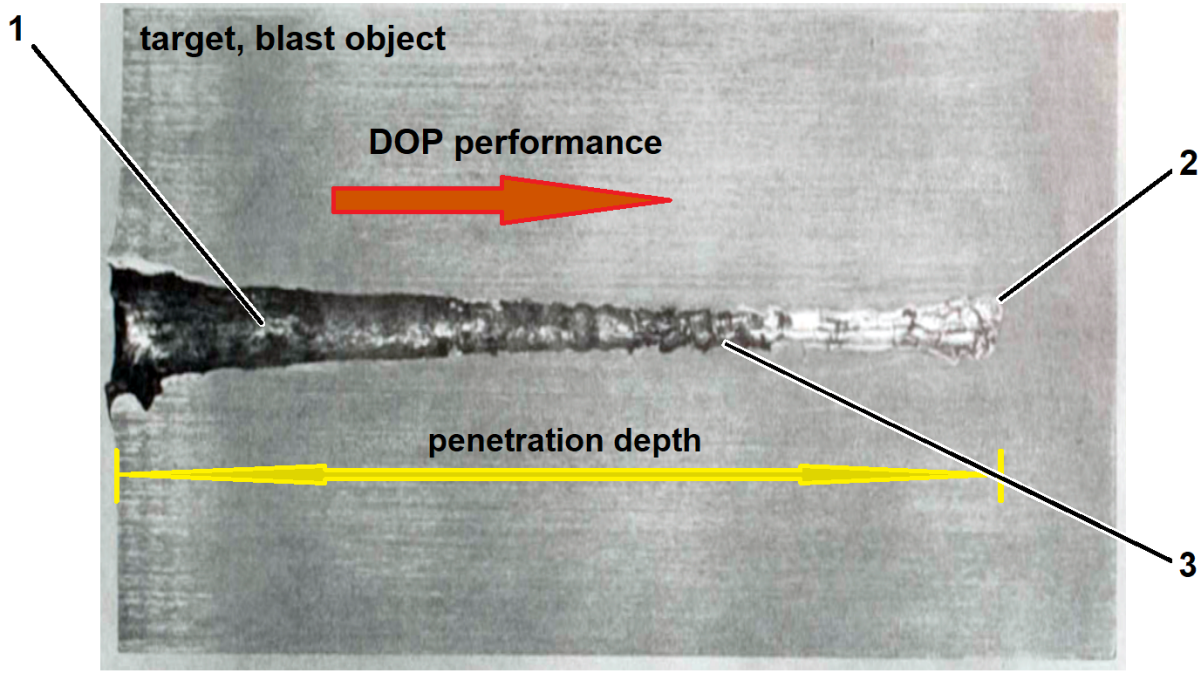

Figure 6: Longitudinal section of a steel plate pierced by a shaped charge jet; taken from [11]. Additionally shown is the "process" of DOP performance that finally results in a decidedly penetration depth.

1 hole-shaped channel
2 crater base
3 crater wall

This means that there is a velocity gradient from the jet tip to the slug, which causes the continuous elongation and longitudinal expansion of the jet. Based on this series of X-ray images in Figure 10, the three hollow charge phenomena listed above can be made clearly understandable.

1. the *concentration effect* due to the fact that the Cu lining is accelerated towards the axis and the jet only forms there with its high speed,

2. the *long duration of action* due to the fact that a long jet is formed, which now also acts against the target for a long period of time,

3. the *stronger effect only at a greater distance*, because only then has the jet stretched or elongated considerably.

Unfortunately, the stretching and elongation of the jet does not continue indefinitely, but rather it splits – depending on the material and several other, but less important design and material parameters – after a certain time or in a certain time interval (Figure 11). The result is what is known as a particulated shaped charge jet.

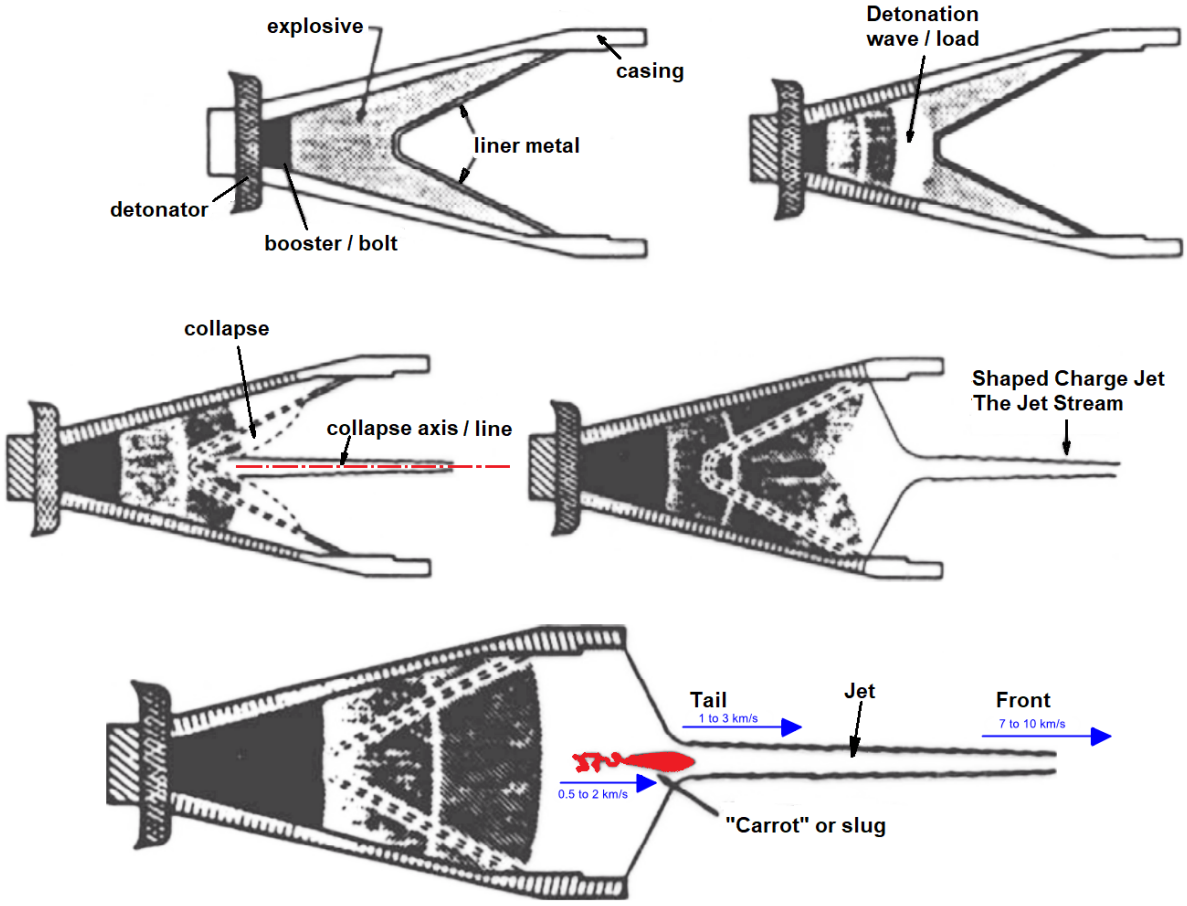

Figure 7: Detonation stages of a hollow charge with a lining from top left to bottom right; taken from [14]

Before tearing, copper now exhibits strains of over 1000 %. To this day, it is still completely unexplained why copper, which produces a maximum strain of 80 % in static tests, now produces 10 to 15 times greater strain values under these extreme loading conditions.

The tearing of the shaped charge jet only takes place once, its length –or more precisely the sum of the lengths of the individual jet particles– remains constant. From now on, the DOP performance of the shaped charge jet should theoretically remain constant as a first approximation. However, the exact alignment of the shaped charge jet in the charge axis causes difficulties, and then wobble and transverse drift effects occur, especially during disintegration due to shear fracture phenomena, whereby the jet or the jet particles no longer effective in an exactly axial manner. As the standoff distance between the shaped charge and the explosive object increases, these angular deviations lead to greater transverse drift, which results in a touching with the wall of the hole in the narrow hole-shaped channels. At these high impact velocities, the corresponding jets parts or jet particles then completely atomize. This explains the increasing decrease in DOP performance with increasing standoff distance.

If a continuous, still contiguous shaped charge jet hits the surface of a material to

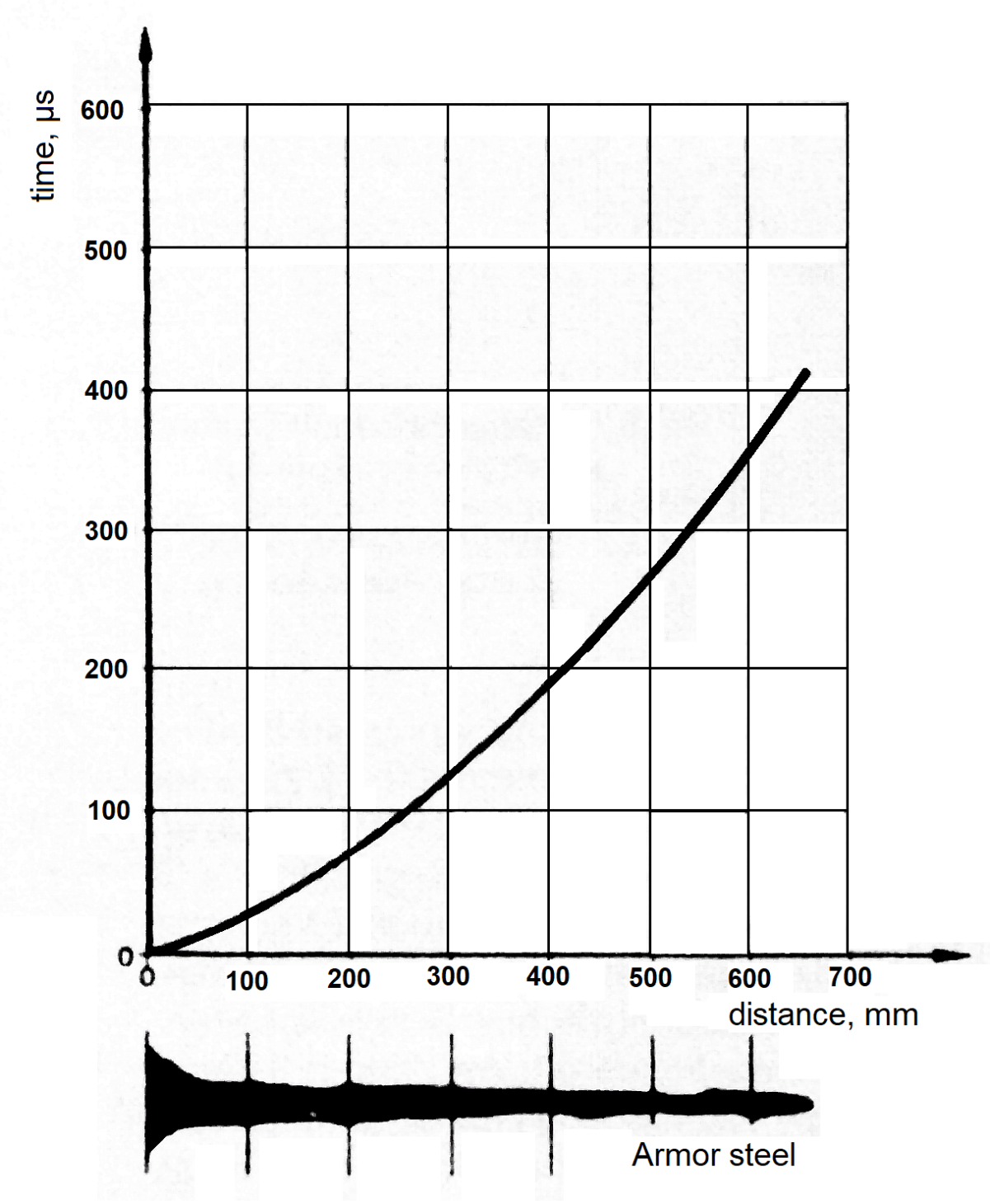

Figure 8: Time-to-distance plot of crater base formation of a shaped charge with a diameter of 100 mm. The functional relationship is described by time $\propto$ const.$\cdot$(distance)$^{\frac{3}{2}}$ with the constant being in this case approximately 0.024

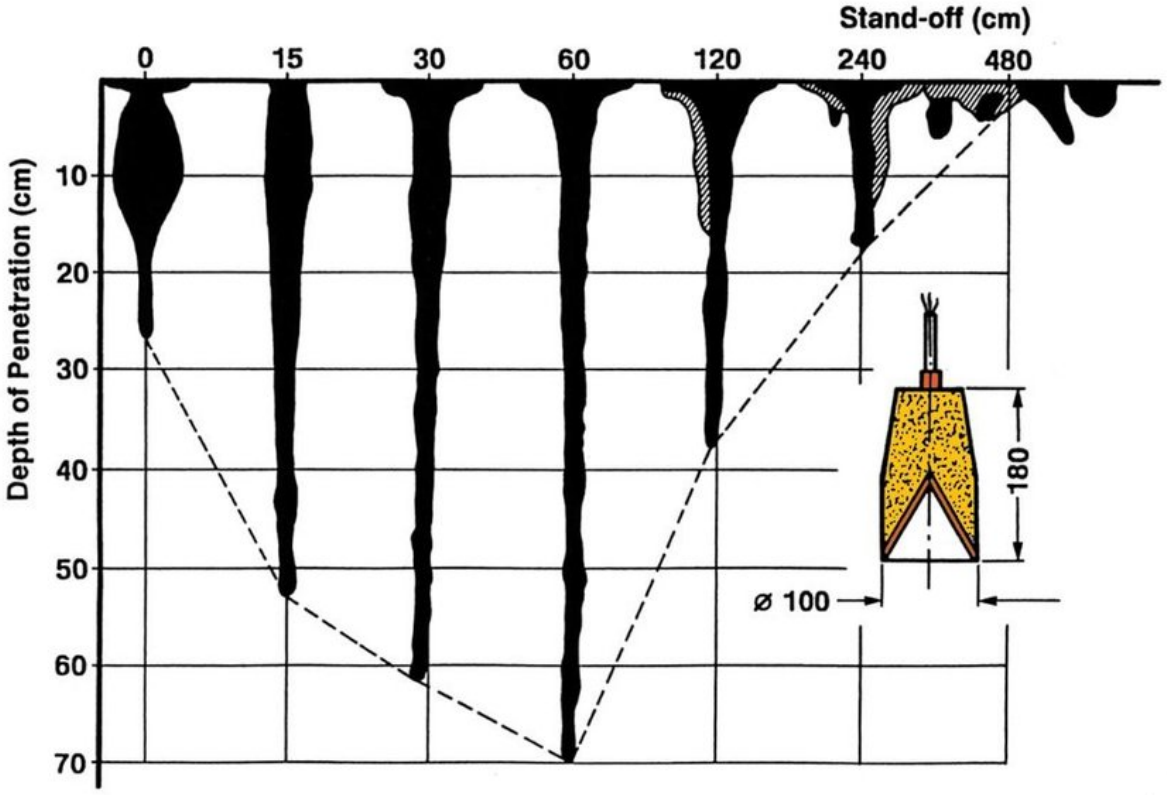

Figure 9: DOP performance as a function of distance, the so-called distance curve, together with the crater profiles with respect to the individual blast distances; from a distance of 1.20 m, an elliptical hole is formed (indicated by the hatched area), and at 4.80 m, several bullet channels occur

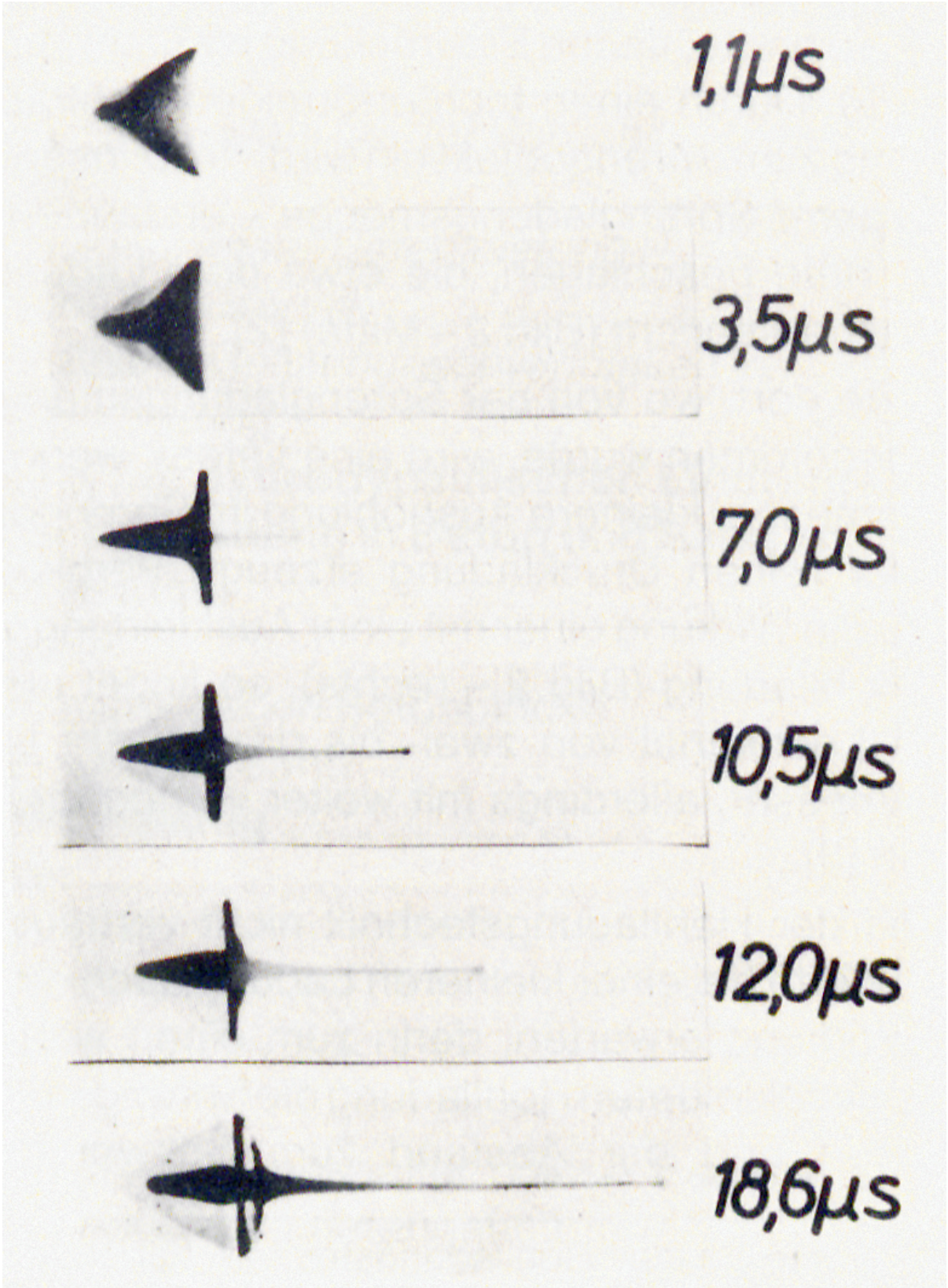

Figure 10: X-ray flash images of the jet formation of a shaped charge with a diameter of 35 mm at different times

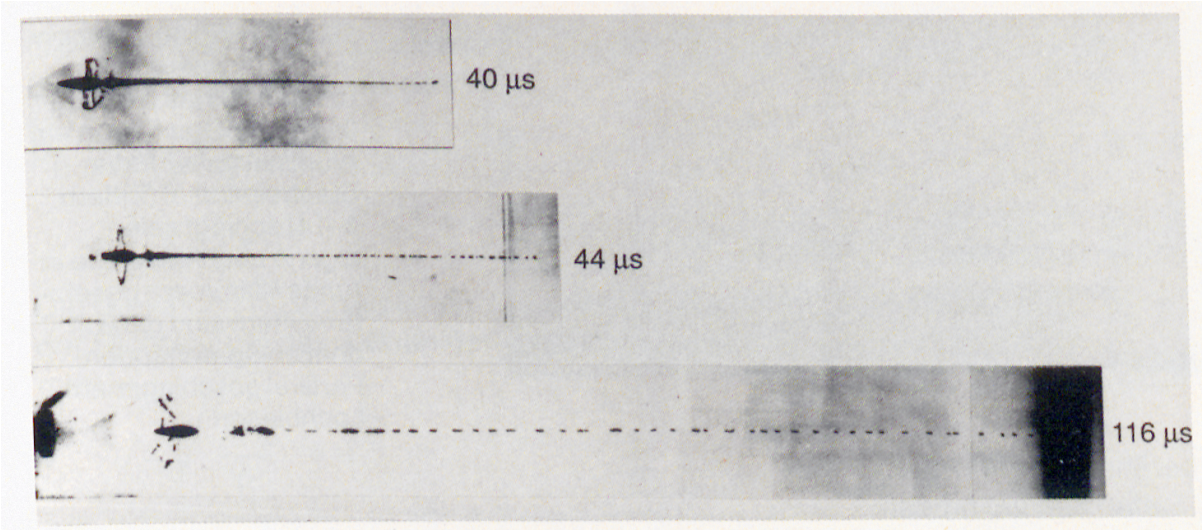

Figure 11: X-ray flash images of the same charge type as in Figure 10 at later time intervals with the start of particulation

be blasted, dynamic pressures of over 100 GPa or 1 Mbar or 10 000 kp mm^{-2} occur at velocities of several 1000 m s^{-1}. These are values that are far above the strength of even the hardest steel. An impression of the penetration of the continuous, contiguous shaped charge jet into a block of duralumin is shown in Figure 12. Particular attention should be drawn to the narrow hole-shaped channel through which the jet must pass without touching the wall so that it can convert its full energy into further penetration capacity.

However, even a shaped charge jet that splits up into single parts still has a good penetration and piercing capacity if the particles or fragments hit the crater base in a well aligned manner (Figure 13). Each individual jet particle strikes its own so-called pinhole.

3 The Hydrodynamical Theory of Penetration of a Shaped Charge Jet

3.1 Penetration with Constant Jet Velocity

First, the penetration of a shaped charge jet, which strikes the blast object at high speed, without elongation or stretching with a given length L that is constant before penetration, is to be considered (Figure 14, top). Furthermore, a purely hydrodynamic penetration should be assumed. This means that both the strength of the shaped charge jet and that of the material to be blasted are completely negligible. Due to the high dynamic pressures occurring at high speeds present here, this simplification is certainly permissible in a first approximation. This is validated by the good agreement of experiments with measurement of crater base formation compared to theory using this assumption, at least at these high velocities. When the shaped charge jet penetrates the material at high speed, it is consumed by degradation from the respective tip by so-called erosion (Figure 14, center).

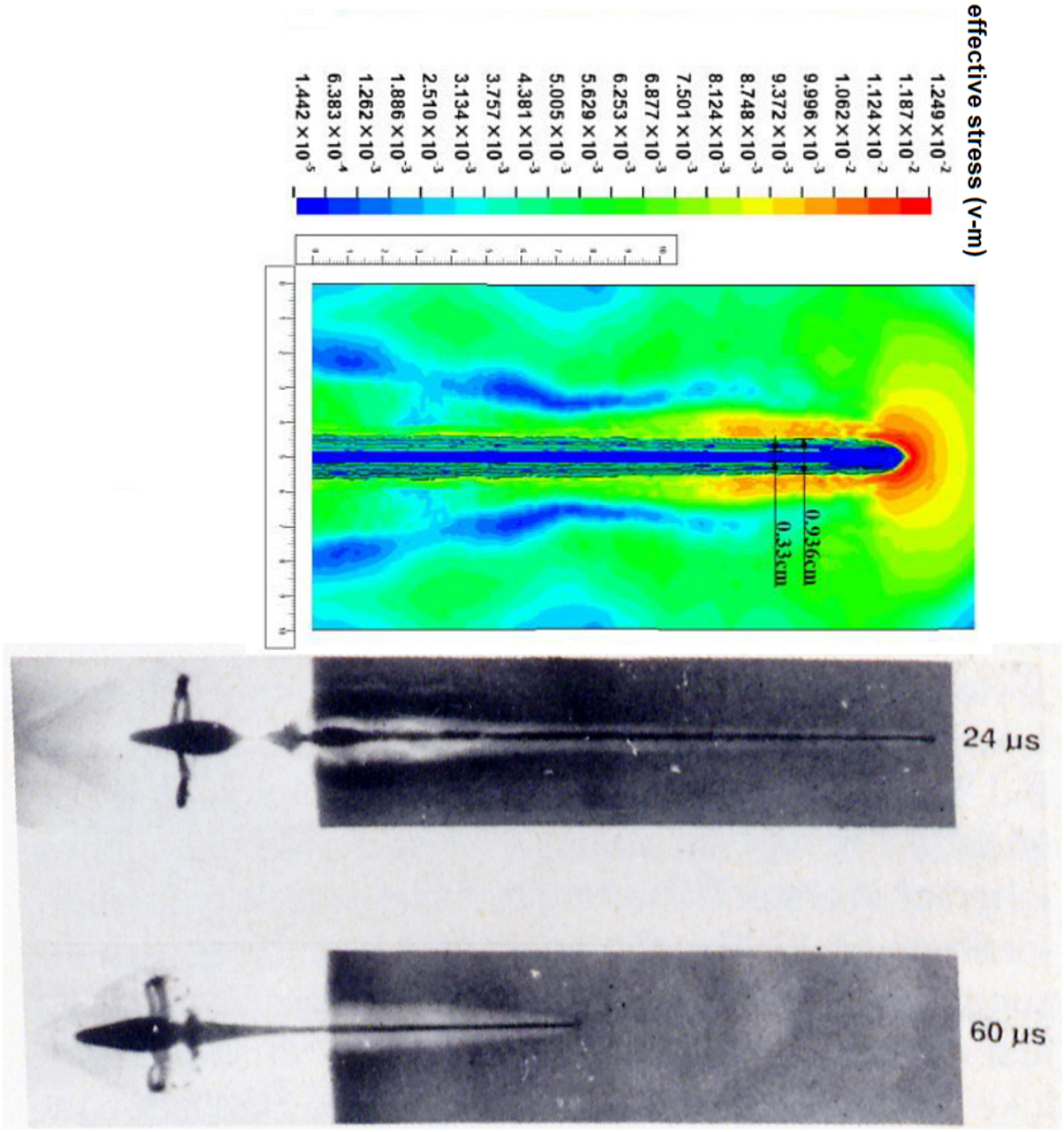

Figure 12: X-ray flash images of the penetration of a shaped charge jet into aluminum at two different times. A precisely trailing shaped charge jet that does not touch the crater wall can fully develop its kinetic energy at the bottom of the crater base. At the top there is attached a simulation by the FEM calculation program LS-DYNA, [15], which shows the jet aperture during the quasi-stationary phase of jet penetration.

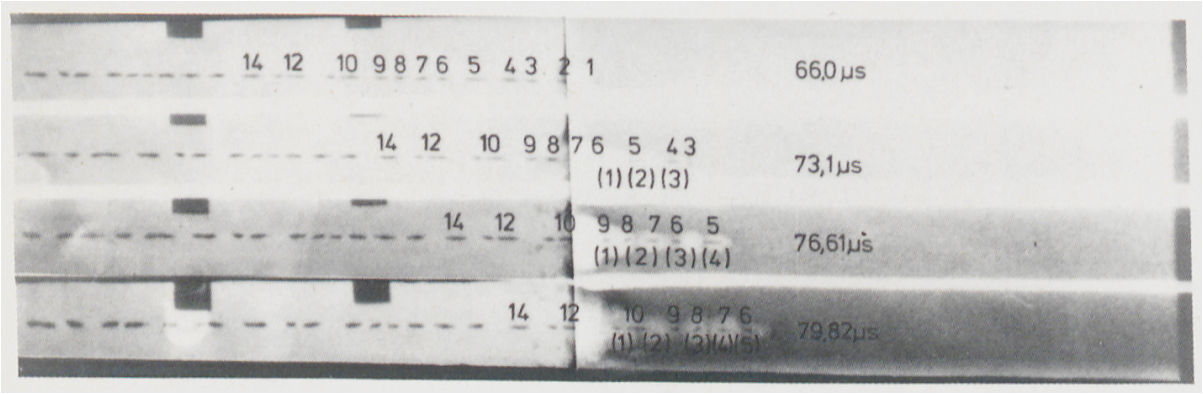

Figure 13: X-ray flash images of the "successive penetration" of a particulated shaped charge jet into an aluminum target. Each jet particle (numbers 1 to 14) punches its own pinhole. The numbers in round brackets are the pinholes punched by the corresponding particle

The process, which in itself is transient in the laboratory system, can be converted into a "stationary" one by a Galilei transformation from the stagnation point or the respective crater base.

Here, the material of the target with the density ρ_T flows towards the stagnation point at the crater base velocity u. The jet with the density ρ_j moves with the difference of the jet velocity v_j, reduced by the crater base velocity u, i.e. with $v_j - u$ also towards this stagnation point (Figure 14, center). The dynamic pressure p_j for the jet can be given by the Bernoulli equation according to:

$$p_j = \frac{1}{2} \cdot \rho_j \cdot (v_j - u)^2 \tag{1}$$

The total pressure p_T that results at the point of impact caused by the material flowing backward towards the stagnation point, is therefore

$$p_\mathrm{T} = \frac{1}{2} \cdot \rho_\mathrm{T} \cdot u^2 \,. \tag{2}$$

The dynamic pressure p_j in the jet and in the object p_T, respectively, must now have the same value, so that:

$$\begin{gathered} p_j = p_\mathrm{T} \\ \frac{1}{2} \cdot \rho_j \cdot (v_j - u)^2 = \frac{1}{2} \cdot \rho_\mathrm{T} \cdot u^2 \,. \end{gathered} \tag{3}$$

Equation 3 can now be rearranged to give

$$v_j - u = \sqrt{\frac{\rho_\mathrm{T}}{\rho_j}} \cdot u \,. \tag{4}$$

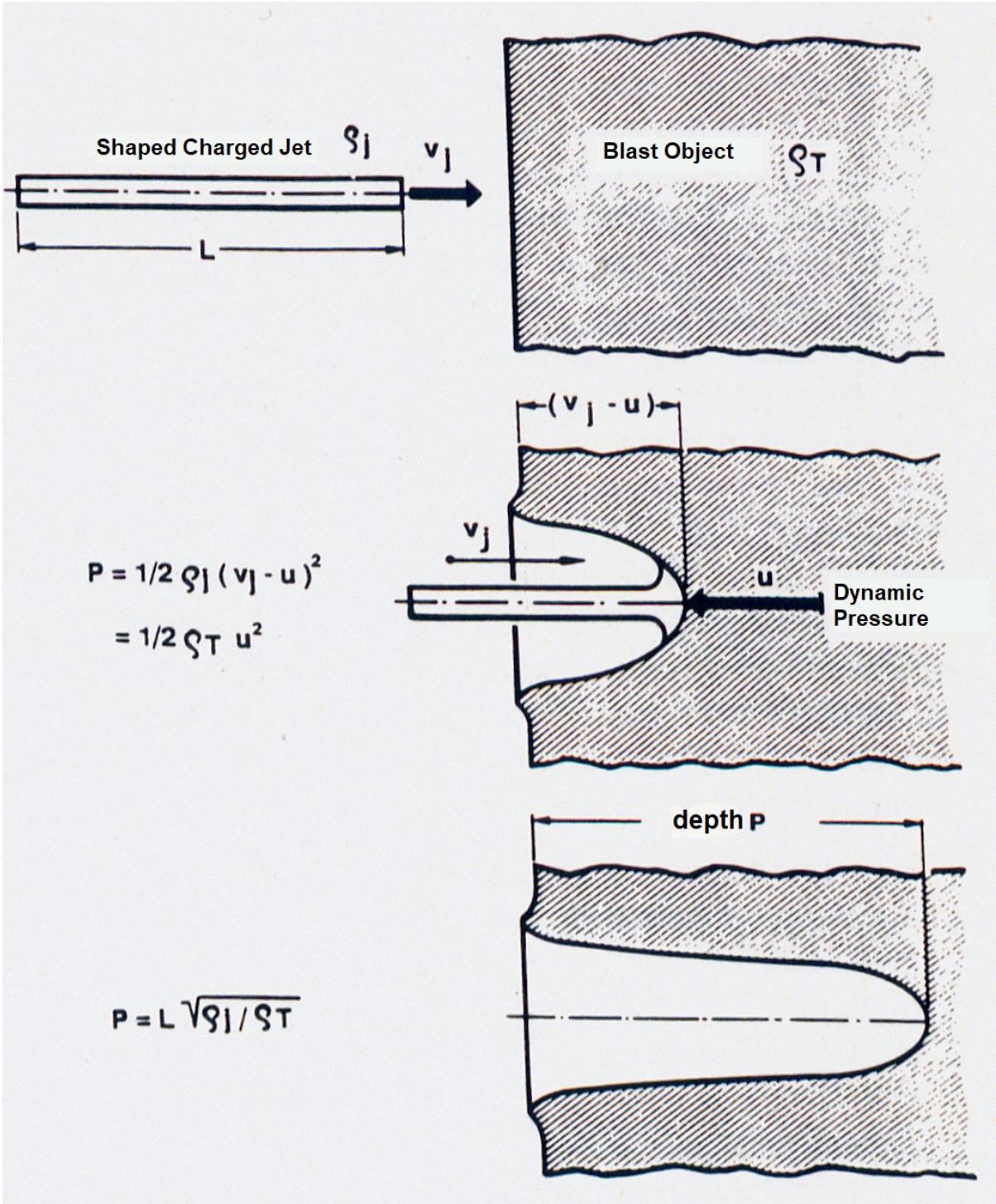

Figure 14: Penetration of a shaped charge jet without velocity gradient in a massive target

From this equation the crater base velocity u can be separated, where

$$\gamma \equiv \sqrt{\frac{\rho_{\mathrm{T}}}{\rho_j}} \tag{5}$$

is set.

$$\begin{aligned} v_j &= u \cdot \left(1 + \sqrt{\frac{\rho_{\mathrm{T}}}{\rho_j}}\right) \\ &= u \cdot (1 + \gamma) \end{aligned} \tag{6}$$

$$u = \frac{v_j}{\left(1 + \sqrt{\frac{\rho_{\mathrm{T}}}{\rho_j}}\right)} = \frac{v_j}{(1+\gamma)} \tag{7}$$

From Equation 7 it is seen immediately that for the same density of the jet and the material the crater base velocity u will become half the impact velocity v_j.

Assuming a constant jet velocity v_j during penetration and thus a constant crater base velocity, the depth-of-penetration (DOP) performance or -effect $\mathbf{P}$ can be derived from the jet length L. The time intervals t_j for complete erosion, i.e. the complete consumption of the jet of length L and $t_{\mathbf{P}}$ for the maximum crater depth $\mathbf{P}_m$, are as follows:

$$t_j = \frac{L}{(v_j - u)} \tag{8a}$$

$$t_{\mathbf{P}_m} = \frac{\mathbf{P}_m}{u}\,. \tag{8b}$$

Since the time t_j for the consumption of the jet on the one hand and the time $t_{\mathbf{P}_m}$ for the formation of the crater base on the other must now be identical under the above conditions, Equation 8a and Equation 8b can be set equal:

$$\frac{L}{(v_j - u)} = \frac{\mathbf{P}_m}{u} \tag{9}$$

Equation 9 may now simply be rearranged to give

$$\mathbf{P}_m = L \cdot \frac{u}{(v_j - u)}\,. \tag{10}$$

By rearranging Equation 10 and replacing the velocities with the densities from Equation 4, the following known expression is obtained:

$$\mathbf{P}_m = L \cdot \sqrt{\frac{\rho_j}{\rho_{\mathrm{T}}}}\,. \tag{11}$$

Considering Equation 5 yields

$$\mathbf{P}_m = \frac{L}{\gamma}\,. \tag{12}$$

Equation 11 is a very well-known and frequently used formula for hydrodynamic penetration, which provides the DOP performance from the product of the length L of the shaped charge jet and the square root of the ratio of jet density to material density. The impact velocity itself plays no role in the DOP performance of hydrodynamic penetration. However, since Equation 11 is derived from very simplified assumptions, such as in particular no velocity gradient and therefore constant jet length, it does not provide an exact statement in practice for the DOP performance of shaped charge jets, although it is very illustrative for trend statements.

According to Equation 11, if the density ρ_{TX} of the material or target X to be blasted changes, but the charge parameters remain constant, i.e. constant length L and jet density ρ_j, the DOP performance $\mathbf{P}_{\mathrm{X}}$ would change to a DOP performance $\mathbf{P}_{\mathrm{S}}$, e.g. in steel S with density ρ_{TS}, as follows:

$$\frac{\mathbf{P}_{\mathrm{X}}}{\mathbf{P}_{\mathrm{S}}} = \sqrt{\frac{\rho_{\mathrm{TS}}}{\rho_{\mathrm{TX}}}}\,. \tag{13}$$

If a density of steel of $7.85\,\mathrm{g\,cm^{-3}}$ is used for ρ_{TS}, the above formula would result in an increase of the DOP performance with a factor of about 1.8 and 2.45 for concrete with a density of $2.4\,\mathrm{g\,cm^{-3}}$ and sand with a density of $1.3\,\mathrm{g\,cm^{-3}}$ respectively.

3.2 Penetration of the Jet with a Velocity Gradient

In order to keep the derivation of the following formulæ clear, the simplified assumption is made that the shaped charge jet originates at "one" time and "one" place, in the so-called virtual (apparent) origin. The distance from the virtual origin to the blast object will be denoted by $\mathcal{Z}_0$. $\mathcal{Z}_0$ is slightly different from the ignition or standoff distance, which is otherwise measured from the base of the shaped charge (Figure 15).

Furthermore, for the sake of simplicity, the initially continuously stretching jet should disintegrate or break-up, respectively, into individual parts at an experimentally determined point in time, the so-called particulation time t_p.

When a crater is formed by a shaped charge jet, a distinction must be made between three different cases (Figure 16):

1. Case I: The crater in the blast object is formed exclusively by a continuously stretching shaped charge jet, which implies a rather small ignition distance or standoff distance, respectively, in practice.

2. Case II: Formation of the hole-shaped channel (hole-opening phase) by an initially continuously stretching shaped charge jet, which subsequently disintegrates into individual particles or fragments, respectively. This is the most common case in practice.

3. Case III: Crater formation exclusively by a particulated shaped charge jet that only occurs at a relatively large standoff distance between the shaped charge and the blast object.

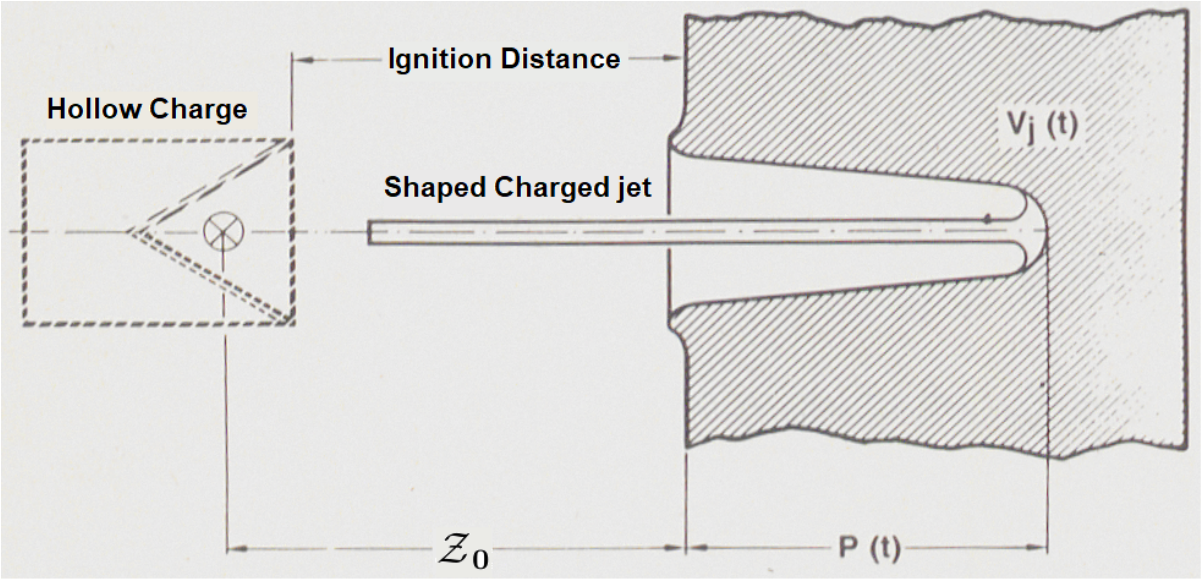

Figure 15: Formation of a shaped charge jet at a designated time and place – the so-called "virtual origin" – with jet elongation and penetration into a target

In the following, the formulæ for the DOP performance **P** are derived as a function of time, the velocity v_j of the jet at the bottom of the crater and the crater base velocity u. However, the formulæ are also solved according to the respective variable, such as the time required to perforate a blast object or the exit velocity according to its specified thickness.

For a better understanding, the derivations are made in such a way that the individual steps can also be understood by someone who is not too experienced in mathematics. Although these derivations and formulæ were already known in the years 1963 to 1965 [1, 5, 6], they were hardly used in practice. Even today, they are only applied and used by a few scientists because they often do not know the formulæ or are afraid to apply them as they do not have an overview of the area of validity. The fact that the respective physical background and the derivations are explained in detail gives the interested person – scientist or experimental engineer – the opportunity to sound out the limits of the applied theory himself. This enables them to use the formulæ correctly for the tasks assigned to them. The use of the formulæ in practice was perhaps also delayed by the fact that calculating with exponents in form of rational numbers required the use of slide rules and, for more precise calculations, logarithmic tables, which was cumbersome. Calculating with exponents is greatly simplified by using scientific calculators. Determining the distance-time diagram of a crater base formation can be done very quickly and reliably with such a tool or even with a small home computer.

The first significant simplification of the theory presented is that the shaped charge jet originates at a point in time at a location known as the virtual origin (Figure 15). This simplification is permissible for large separations or standoff distances, respectively, between the charge and the blast object and is also valid for many charge designs. This

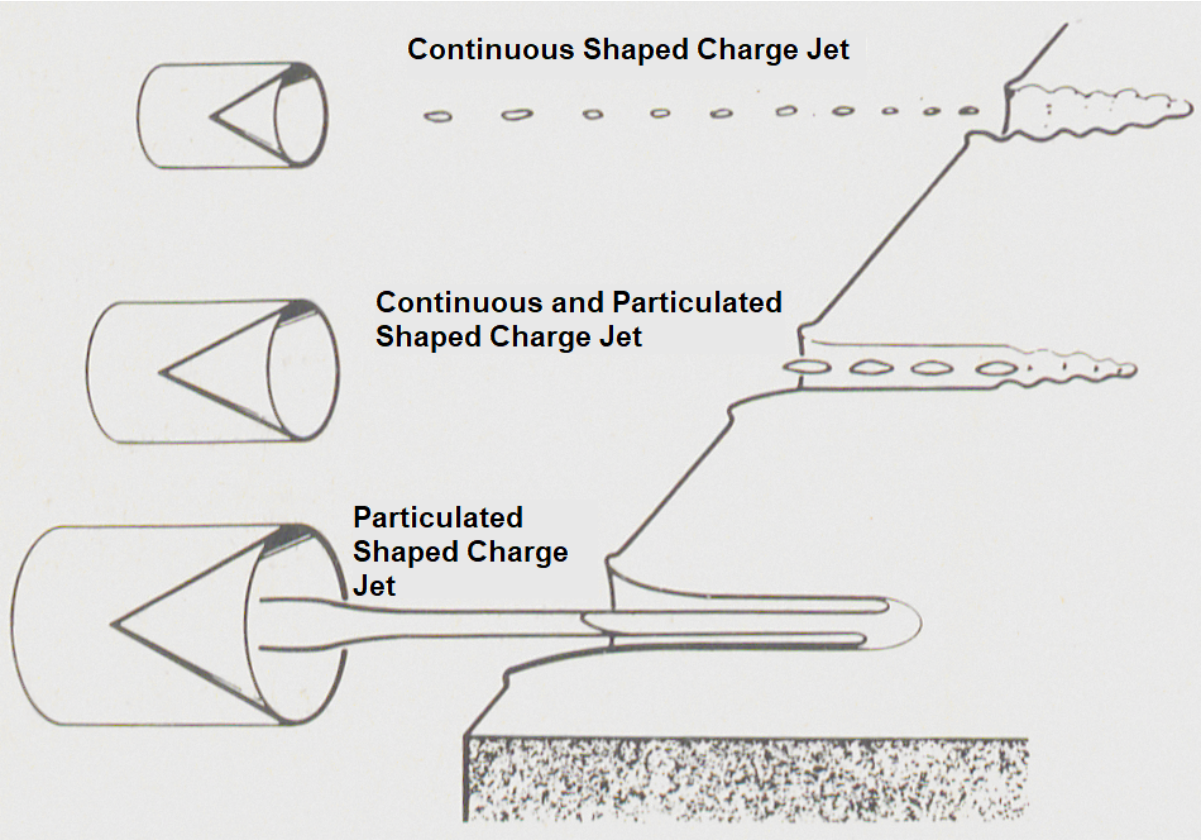

Figure 16: Crater formation (hole-opening phase) by continuously elongating jet or, first continuously elongating and then particulated jet or by a shaped charge jet completely disintegrated into individual particles

assumption is not valid, for example, for a trumpet-shaped lining that is blasted at a small standoff distance of one to two times the charge diameter from the blast object. The tip area of the jet is formed deeper from within the liner than the residual jet from the base area. If the DOP capabilities of such complex lining geometries are to be calculated in advance at a close range, then the distance-to-time curve of the collapse process must be used. Calculating the jet velocities from such a distance-to-time profile would be difficult with a scientific pocket calculator, but presents no problems with a personal computer nowadays used. However, this refinement of the program will not be considered here, as it is only a correction, although it may well be important in some cases. It would further complicate the derivation unnecessarily and considerably, thereby losing some of its clarity.

3.2.1 Case I. Crater Base Formation with Continuous Jet

As can be seen in Figure 15, the jet with its linear velocity gradient and with the jet velocity $v_j(t)$ hits the crater base at the penetration depth $\mathbf{P}$ just at time t, whereby the material to be blasted away moves with the crater base velocity u. In this case, the jet with its velocity v_j originated at the virtual origin at time $t = 0$. The distance traveled by the jet at velocity $v_{j,T}$ during the time interval t is equal to the sum of the distance $\mathcal{Z}_0$ of the virtual origin from the material surface and the crater depth $\mathbf{P}$ at time t. This means that one can write for this:

$$\mathbf{P}(t) + \mathcal{Z}_0 = v_j(t) \cdot t \,. \tag{14}$$

The bracket (t) indicates that the values always apply at time t. This information is now omitted in the following description. Equation 14 can of course be rearranged to solve for the individual parameters, such as jet velocity v_j or time t:

$$v_j = \frac{\mathbf{P} + \mathcal{Z}_0}{t} \,, \tag{15a}$$

$$t = \frac{\mathbf{P} + \mathcal{Z}_0}{v_j} \,. \tag{15b}$$

The following simple relationship applies to the maximum jet tip speed $v_{j,0}$ or the arrival time t of the jet tip at the surface of the object:

$$v_{j,0} = \frac{\mathcal{Z}}{t_0} \tag{16}$$

$$t_0 = \frac{\mathcal{Z}_0}{v_{j,0}} \tag{17a}$$

$$\mathcal{Z}_0 = v_{j,0} \cdot t_0 \,. \tag{17b}$$

From Equation 14 the DOP performance $\mathbf{P}$ at time t is obtained according to

$$\mathbf{P} = v_j \cdot t - \mathcal{Z}_0 \,. \tag{18}$$

If we differentiate the penetration depth $\mathbf{P}$ with respect to time t, we get the crater base velocity u. Here we have two time-dependent variables, namely the jet speed v_j and the time t itself. When differentiating, each individual time-dependent term must now be differentiated separately and added together. This results in

$$u = \frac{\mathrm{d}\,\mathbf{P}}{\mathrm{d}t} = \frac{\mathrm{d}v_j}{\mathrm{d}t} \cdot t + v_j \cdot \frac{\mathrm{d}t}{\mathrm{d}t} \,. \tag{19}$$

Equation 7 can now be used for the crater base velocity u. Although it was originally established for a constant jet velocity, it also applies when the crater base velocity u

changes as a function of time. This means that Equation 7 can be used for u to obtain:

$$\frac{v_j}{(1+\gamma)} = \frac{\mathrm{d}v_j}{\mathrm{d}t} \cdot t + v_j \tag{20}$$

Now, the jet velocity v_j can be summarized to give:

$$-\frac{\mathrm{d}v_j}{\mathrm{d}t} \cdot t = \left(\frac{1+\gamma}{(1+\gamma)} - \frac{1}{(1+\gamma)}\right) \cdot v_j$$

which is

$$-\frac{\mathrm{d}v_j}{\mathrm{d}t} \cdot t = \frac{\gamma}{(1+\gamma)} \cdot v_j \,. \tag{21}$$

By separation of the jet velocity v_j and time t the following differential equation is obtained:

$$\frac{\mathrm{d}v_j}{v_j} = -\frac{\gamma}{(1+\gamma)} \cdot \frac{\mathrm{d}t}{t} \,. \tag{22}$$

This can now be integrated for the jet velocity v_j and the time t, with the boundary condition that the jet hits the object with the maximum jet tip speed $v_{j,0}$ at time t_0 and is located at the crater base with the velocity v_j at time t.

With these boundary conditions the integral with the limits may be written in the form:

$$\int_{v_j=v_{j,0}}^{v_j=v_j} \frac{\mathrm{d}v_j}{v_j} = -\frac{\gamma}{(1+\gamma)} \cdot \int_{t=t_0}^{t=t} \frac{\mathrm{d}t}{t} \,. \tag{23}$$

Integration of Equation 23 yields

$$\ln\left(v_j\right) - \ln\left(v_{j,0}\right) = -\frac{\gamma}{(1+\gamma)} \cdot \left[\ln\left(t\right) - \ln\left(t_0\right)\right] \,. \tag{24}$$

The natural logarithms can be combined to give

$$\ln\left(\frac{v_j}{v_{j,0}}\right) = -\frac{\gamma}{(1+\gamma)} \cdot \ln\left(\frac{t}{t_0}\right) \,. \tag{25}$$

Equation 25 can now be exponentialized to give

$$\frac{v_j}{v_{j,0}} = \left(\frac{t}{t_0}\right)^{-\frac{\gamma}{(1+\gamma)}}$$

or using the formalism of the reciprocal

$$\frac{v_j}{v_{j,0}} = \left(\frac{t_0}{t}\right)^{\frac{\gamma}{(1+\gamma)}} \,. \tag{26}$$

This equation can be solved for v_j and a constant of the triple pair $v_{j,0}$, t_0 or $\mathcal{Z}_0$ can be

replaced. This allows the following variations to be written for Equation 26:

$$v_j = v_{j,0} \cdot \left(\frac{t_0}{t}\right)^{\frac{\gamma}{(1+\gamma)}} \tag{27a}$$

$$\begin{aligned} v_j &= \frac{\mathcal{Z}_0}{t_0} \cdot \left(\frac{t_0}{t}\right)^{\frac{\gamma}{(1+\gamma)}} \\ &= \mathcal{Z}_0 \cdot t_0^{-\frac{1}{(1+\gamma)}} \cdot t^{-\frac{\gamma}{(1+\gamma)}} \end{aligned} \tag{27b}$$

$$\begin{aligned} v_j &= v_{j,0} \cdot \left(\frac{\mathcal{Z}_0}{v_{j,0}}\right)^{\frac{\gamma}{(1+\gamma)}} \cdot t^{-\frac{\gamma}{(1+\gamma)}} \\ &= \mathcal{Z}_0^{\frac{\gamma}{(1+\gamma)}} \cdot v_{j,0}^{\frac{1}{(1+\gamma)}} \cdot t^{-\frac{\gamma}{(1+\gamma)}} \, . \end{aligned} \tag{27c}$$

Equation 26 thus gives the shaped charge jet velocity v_j at the crater base after time t with the boundary condition that the jet tip arrives at $\mathcal{Z}_0$, the distance of the virtual origin from the object surface, with a maximum jet tip speed $v_{j,0}$ at time t.

Equation 26 can, of course, also be solved for the time t, which yields:

$$\frac{t_0}{t} = \left(\frac{v_j}{v_{j,0}}\right)^{\frac{1+\gamma}{\gamma}} \tag{28}$$

$$t = t_0 \cdot \left(\frac{v_{j,0}}{v_j}\right)^{\frac{1+\gamma}{\gamma}} \tag{29a}$$

$$\begin{aligned} t &= \frac{\mathcal{Z}_0}{v_{j,0}} \cdot \left(\frac{v_{j,0}}{v_j}\right)^{\frac{1+\gamma}{\gamma}} \\ &= \mathcal{Z}_0 \cdot v_{j,0}^{\frac{1}{\gamma}} \cdot v_j^{-\frac{1+\gamma}{\gamma}} \end{aligned} \tag{29b}$$

$$\begin{aligned} t &= t_0 \cdot \left(\frac{\mathcal{Z}_0}{t_0}\right)^{\frac{1+\gamma}{\gamma}} \cdot v_j^{-\frac{1+\gamma}{\gamma}} \\ &= t_0^{-\frac{1}{\gamma}} \cdot \left(\frac{\mathcal{Z}_0}{v_j}\right)^{\frac{1+\gamma}{\gamma}} \end{aligned} \tag{29c}$$

Equation 27a can be inserted into Equation 18. In this way, the DOP $\mathbf{P}$ as a function of time t with the parameters $v_{j,0}$, t_0, and $\mathcal{Z}_0$ is obtained:

$$\mathbf{P} = v_{j,0} \cdot \left(\frac{t_0}{t}\right)^{\frac{\gamma}{(1+\gamma)}} \cdot t - \mathcal{Z}_0 \, . \tag{30}$$

After some manipulation of Equation 30 we get:

$$\mathbf{P} = v_{j,0} \cdot t_0^{\frac{\gamma}{(1+\gamma)}} \cdot t^{\frac{\gamma}{(1+\gamma)}} - \mathcal{Z}_0 \tag{31a}$$

$$\begin{aligned} \mathbf{P} &= \mathcal{Z}_0 \cdot t_0^{-\frac{1}{(1+\gamma)}} \cdot t^{\frac{1}{(1+\gamma)}} - \mathcal{Z}_0 \\ &= \mathcal{Z}_0 \cdot \left[\left(\frac{t}{t_0} \right)^{\frac{1}{(1+\gamma)}} - 1 \right] \end{aligned} \tag{31b}$$

$$\mathbf{P} = v_{j,0}^{\frac{1}{(1+\gamma)}} \cdot \mathcal{Z}_0^{\frac{\gamma}{(1+\gamma)}} \cdot t^{\frac{1}{(1+\gamma)}} - \mathcal{Z}_0 \ . \tag{31c}$$

By solving Equation 30 or, even better, Equation 31a for t one obtains the necessary time required to reach the DOP $\mathbf{P}$:

$$t^{\frac{1}{(1+\gamma)}} = (\mathbf{P} + \mathcal{Z}_0) \cdot \frac{1}{v_{j,0}} \cdot t_0^{-\frac{\gamma}{(1+\gamma)}} \tag{32}$$

$$t = (\mathbf{P} + \mathcal{Z}_0)^{(1+\gamma)} \cdot v_{j,0}^{-(1+\gamma)} \cdot t_0^{-\gamma} \tag{33a}$$

$$t = (\mathbf{P} + \mathcal{Z}_0)^{(1+\gamma)} \cdot \mathcal{Z}_0^{-(1+\gamma)} \cdot t_0 \tag{33b}$$

$$t = (\mathbf{P} + \mathcal{Z}_0)^{(1+\gamma)} \cdot \mathcal{Z}_0^{-\gamma} \cdot \frac{1}{v_{j,0}} \tag{33c}$$

In order to be able to work in a two-dimensional representation, one must always eliminate one variable from the three variables in Equation 14, the DOP performance $\mathbf{P}$, the jet velocity at the bottom of the crater v_j and the corresponding time t. The elimination of v_j in Equation 14 by Equation 26 resulted in a DOP performance $\mathbf{P}$ as a function of time t in Equation 30.

By replacing the time t in Equation 33c with Equation 15b, the DOP performance $\mathbf{P}$ is obtained as a function of the jet velocity v_j at the bottom of the crater, i.e. the crater base.

$$\frac{(\mathbf{P} + \mathcal{Z}_0)}{v_j} = (\mathbf{P} + \mathcal{Z}_0)^{(1+\gamma)} \cdot \mathcal{Z}_0^{-\gamma} \cdot \frac{1}{v_{j,0}} \tag{34}$$

$$\frac{(\mathbf{P} + \mathcal{Z}_0)}{(\mathbf{P} + \mathcal{Z}_0)^{(1+\gamma)}} = \left(\frac{v_j}{v_{j,0}} \right) \cdot \mathcal{Z}_0^{-\gamma} \tag{35a}$$

$$(\mathbf{P} + \mathcal{Z}_0)^{\gamma} = \left(\frac{v_{j,0}}{v_j} \right) \cdot \mathcal{Z}_0^{\gamma} \tag{35b}$$

$$\begin{aligned} \mathbf{P} &= \mathcal{Z}_0 \cdot \left(\frac{v_{j,0}}{v_j} \right)^{\frac{1}{\gamma}} - \mathcal{Z}_0 \\ \mathbf{P} &= \mathcal{Z}_0 \cdot \left[\left(\frac{v_{j,0}}{v_j} \right)^{\frac{1}{\gamma}} - 1 \right] \end{aligned} \tag{35c}$$

Equation 35c is a very important one, because it expresses the DOP performance $\mathbf{P}$ as a function of the jet velocity v_j with the parameters distance $\mathcal{Z}_0$ of the virtual origin from the surface of the blast object, the maximum jet tip speed $v_{j,0}$ and the square root of the ratio of the densities of the object and jet material.

Equation 35c shows that the DOP performance $\mathbf{P}$ increases linearly with increasing distance $\mathcal{Z}_0$. Furthermore, this shows that the gradient in the $(P - \mathcal{Z}_0)$ diagram is determined by the expression $\left[\left(\frac{v_{j,0}}{v_j}\right)^{\frac{1}{\gamma}} - 1\right]$.

This means that the greater the maximum jet tip speed $v_{j,0}$ and the lower the residual effective jet velocity v_j, the greater the DOP performance at the specified distance. This equation will be discussed in more detail later.

Equation 35b can of course also be solved according to the residual jet velocity v_j after the perforation of a steel plate of thickness $\mathbf{P}$:

$$v_j = v_{j,0} \cdot \left(\frac{\mathcal{Z}_0}{\mathbf{P} + \mathcal{Z}_0}\right)^{\gamma} . \tag{36}$$

As mentioned above, Equation 7 also applies to the crater base velocity u in the case of the elongating and stretching jet.

The jet velocity v_j in Equation 7 can be substituted with Equation 36 to give

$$u = \frac{v_j}{(1+\gamma)} = v_{j,0} \cdot \left(\frac{\mathcal{Z}_0}{\mathbf{P} + \mathcal{Z}_0}\right)^{\gamma} \cdot \frac{1}{(1+\gamma)} . \tag{37}$$

This now gives us the respective crater base velocity u in relation to the perforation distance $\mathbf{P}$. Equation 37 can now also be solved for $\mathbf{P}$, and we thus obtain the DOP performance $\mathbf{P}$ as a function of the crater base velocity u:

$$\begin{aligned} \mathbf{P} &= \mathcal{Z}_0 \cdot \left(\frac{v_{j,0}}{u}\right)^{\frac{1}{\gamma}} \cdot (1+\gamma)^{-\frac{1}{\gamma}} - \mathcal{Z}_0 \\ &= \mathcal{Z}_0 \cdot \left[\left(\frac{v_{j,0}}{u \cdot (1+\gamma)}\right)^{\frac{1}{\gamma}} - 1\right] \end{aligned} \tag{38}$$

By using Equation 7 and Equation 27c, the crater base velocity u is obtained as a function of time t, and by solving Equation 39, the time t is obtained as a function of the cratering velocity u:

$$u = v_{j,0}^{\frac{1}{(1+\gamma)}} \cdot \mathcal{Z}_0^{\frac{\gamma}{(1+\gamma)}} \cdot t^{-\frac{\gamma}{(1+\gamma)}} \cdot \frac{1}{(1+\gamma)} \tag{39}$$

$$t = \mathcal{Z}_0 \cdot v_{j,0}^{\frac{1}{\gamma}} \cdot [(1+\gamma) \cdot u]^{-\frac{1+\gamma}{\gamma}} \tag{40}$$

Instead of solving Equation 39 for time t, one could also have replaced the jet velocity v_j in Equation 29b with $v_j = u \cdot (1+\gamma)$ according to Equation 7 to obtain the same result.

In the following it will be shown that there is equality in the formulæ, regardless of whether one assumes the differential $\frac{\mathrm{d}\,\mathbf{P}}{\mathrm{d}t}$ or the BERNOULLI equation with $u = v_j/(1+\gamma)$ for the crater base velocity u, as proceeded from Equation 37.

If, e.g., one differentiates Equation 31c with respect to time t, the following equation is obtained:

$$\begin{aligned} u &= \frac{\mathrm{d}\,\mathbf{P}}{\mathrm{d}t} \\ &= v_{j,0}^{\frac{1}{(1+\gamma)}} \cdot \mathcal{Z}_0^{\frac{\gamma}{(1+\gamma)}} \cdot \frac{\mathrm{d}t^{\frac{1}{(1+\gamma)}}}{\mathrm{d}t} \,. \end{aligned} \tag{41}$$

Looking at the differential quotient

$$\begin{aligned} \frac{\mathrm{d}t^{\frac{1}{(1+\gamma)}}}{\mathrm{d}t} &= \frac{1}{(1+\gamma)} \cdot t^{\frac{1}{(1+\gamma)}-1} \\ &= t^{-\frac{\gamma}{(1+\gamma)}} \cdot \frac{1}{(1+\gamma)} \end{aligned}$$

only, the following expression for Equation 41 is obtained:

$$u = v_{j,0}^{\frac{1}{(1+\gamma)}} \cdot \mathcal{Z}_0^{\frac{\gamma}{(1+\gamma)}} \cdot t^{-\frac{\gamma}{(1+\gamma)}} \cdot \frac{1}{(1+\gamma)} \,. \tag{42}$$

Equation 42 and Equation 39 are identical. The result is therefore the same regardless of whether the DOP performance $\mathbf{P}$ is differentiated with respect to time or whether the BERNOULLI equation (Equation 7) is used.

Validity of Continuous Jet Penetration The above formulæ are only valid as long as the jet penetrates continuously. As soon as the jet particulates, the formulæ given here can no longer be applied. In other words, the jet particulation time t_p must be greater than the time t for the continuously penetrating jet. The maximum penetration depth $\mathbf{P}_m$ is determined by the minimum jet velocity $\mathrm{v_{j,min.}}$. It is therefore the case that the particulation time t_p must be greater than the time for the minimum effective jet part $\mathrm{v_{j,min.}}$, which has to bridge the distance of the maximum DOP performance $\mathbf{P}$ and also the distance $\mathcal{Z}_0$ between the virtual origin and the target:

$$t_p \geqq \frac{\mathbf{P}_m + \mathcal{Z}_0}{\mathrm{v_{j,min.}}} \tag{43}$$

For the sum $(\mathbf{P}_m + \mathcal{Z}_0)$ we can insert Equation 35c in the last formula which gives

$$t_p \geqq \frac{\mathcal{Z}_0 \cdot \left(\frac{v_{j,0}}{\mathrm{v_{j,min.}}}\right)^{\frac{1}{\gamma}}}{\mathrm{v_{j,min.}}} \,. \tag{44}$$

Solving the last equation for $\mathcal{Z}_0$ we get

$$\mathcal{Z}_0 \geqq t_p \cdot \mathrm{v_{j,min.}} \cdot \left(\frac{\mathrm{v_{j,min.}}}{v_{j,0}} \right)^{\frac{1}{\gamma}} . \tag{45}$$

The meaning of this formula will be briefly explained using an example. We assume a particulation time t_p of 150 µs, which is typical for a copper jet of a shaped charge with a base diameter of 100 mm. Furthermore, the maximum jet tip speed of the copper jet should be 9 mm µs^{-1} and the minimum effective jet velocity should be 3 mm µs^{-1}. For the sake of simplicity, a blast object made of copper is assumed for the jet, so that the value for $\gamma = \sqrt{\rho_\mathrm{T}/\rho_j} = 1$.

With these data we obtain

$$\mathcal{Z}_0 \leqq 150\,\mu\mathrm{s} \cdot 3\,\mathrm{mm}\,\mu\mathrm{s}^{-1} \cdot \left(\frac{3\,\mathrm{mm}\,\mu\mathrm{s}^{-1}}{9\,\mathrm{mm}\,\mu\mathrm{s}^{-1}} \right)^1 = 150\,\mathrm{mm}\,.$$

This means that the distance of the virtual origin from the target surface must be less than 150 mm. Since the virtual origin for the metal liner with $2\alpha = 60°$ is about ²/₃ from the diameter inside the metal liner, a distance of 65 mm has to be subtracted from the 150 mm to obtain the ignition distance from the base. This results in $150 - 65 = 85$ mm. In other words, this means that the continuous penetration of the jet only occurs under the boundary conditions specified above if the ignition distance is smaller than the charge diameter.

Since, conversely, the DOP performance increases with increasing standoff distance, this value is nowadays always exceeded. In practice, there is no longer only continuous jet penetration, but always the mixed case of first continuous and then particulated penetration, i.e. case 2. However, since case 2 is a mixture of case 1 and case 3, case 3 will be derived and described in detail first for the sake of better understanding.

3.2.2 Case III. Crater Base Formation with particulated Jet

Case 3 applies if the jet tip has already been particulated when it hits the target. This means that the time t must be greater than the particulation time t_p.

This implies that $t = \frac{\mathcal{Z}_0}{v_{j,0}} > t_p$.

The DOP performance of a non-elongating and non-stretching jet is given by Equation 12 with $\mathbf{P} = L/\gamma$. According to Figure 17, the length of a particulated jet is given by

$$L = (v_{j,0} - v_j) \cdot t_p\,. \tag{46}$$

in the time-to-distance diagram.

In other words, the DOP performance $\mathbf{P}$ is obtained here as a function of the jet velocity v_j with the parameters of the maximum jet tip speed $v_{j,0}$, the particulation time t_p and

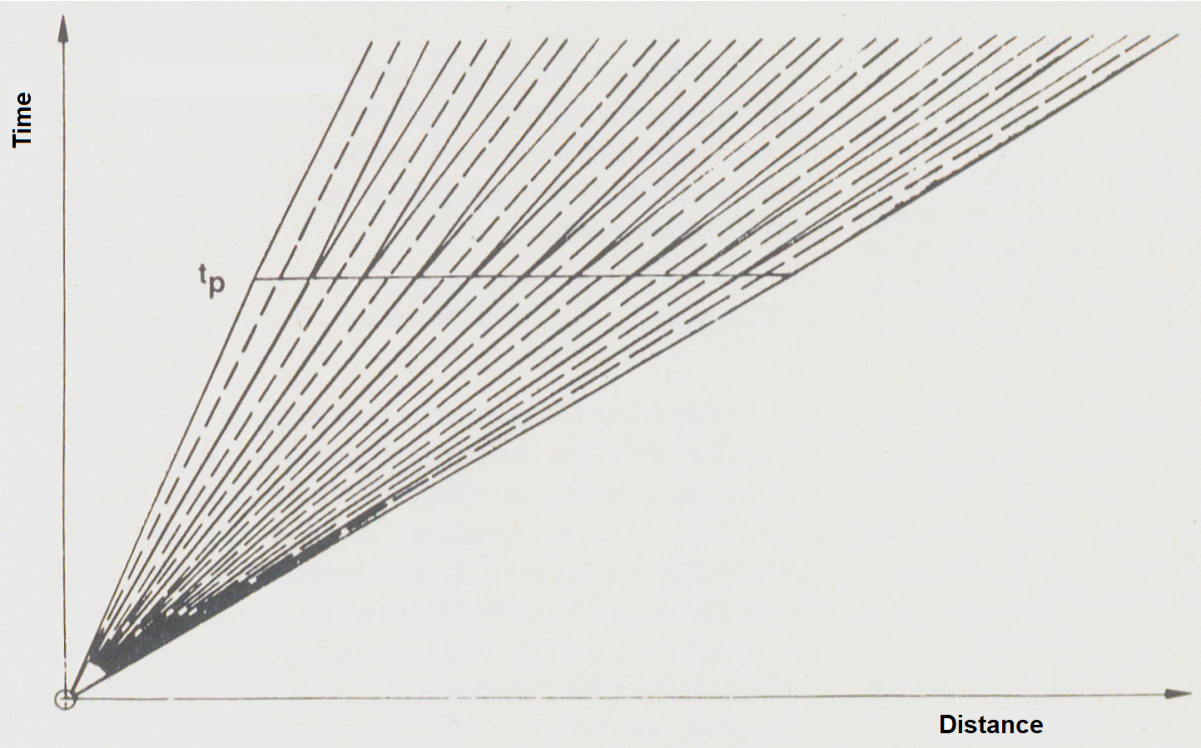

Figure 17: Particulation of an elongating jet at time t_p illustrated in a distance-time diagram

the square root of the ratio of the densities of the blast object and the jet γ:

$$\mathbf{P} = (v_{j,0} - v_j) \cdot \left(\frac{t_p}{\gamma}\right) . \tag{47}$$

Equation 47 can of course now be solved for the speed of the jet v_j again. The result is the top speed v_j of the particulated residual jet that has perforated a plate with thickness $\mathbf{P}$:

$$v_j = v_{j,0} - \mathbf{P} \cdot \left(\frac{\gamma}{t_p}\right) \tag{48}$$

If we want to express the DOP performance as a function of time for a particulated shaped charge jet, we have to replace v_j by Equation 15a and obtain

$$\frac{\mathbf{P} + \mathcal{Z}_0}{t} = v_{j,0} - \frac{P \cdot \gamma}{t_p} \tag{49}$$

From Equation 49 the DOP performance $\mathbf{P}$ as a function of time t can be separated:

$$\mathbf{P} + \mathbf{P} \cdot \gamma \cdot \left(\frac{t}{t_p}\right) = v_{j,0} \cdot t - \mathcal{Z}_0 . \tag{50a}$$

$$\begin{aligned}\mathbf{P} &= \frac{v_{j,0}\cdot t - \mathcal{Z}_0}{\left(1+\gamma\cdot\left(\frac{t}{t_p}\right)\right)} = \frac{v_{j,0}\cdot(t-t_0)}{\left(1+\gamma\cdot\left(\frac{t}{t_0}\right)\right)} \\ &= \frac{v_{j,0}\cdot t_p\cdot(t-t_0)}{(t_p+\gamma\cdot t)}\end{aligned} \tag{50b}$$

The third term of Equation 50b is most commonly found in literature.

By solving Equation 49, the time t is obtained that is necessary for a particulated jet to reach the DOP performance $\mathbf{P}$ in a blast object:

$$t = \frac{\mathbf{P}+\mathcal{Z}_0}{\left(v_{j,0}-\mathbf{P}\cdot\frac{\gamma}{t_p}\right)}\,. \tag{51}$$

In order to obtain the jet velocity v_j for the particulated jet as a function of time at the bottom of the crater, Equation 18 must be inserted into Equation 48:

$$v_j = v_{j,0} - v_j\cdot\gamma\cdot\left(\frac{t}{t_p}\right) - \mathcal{Z}_0\cdot\left(\frac{\gamma}{t_p}\right)\,. \tag{52}$$

Solving Equation 52 for v_j, we obtain:

$$v_j = \frac{v_{j,0}-\mathcal{Z}_0\cdot\left(\frac{\gamma}{t_p}\right)}{\left(1+\gamma\cdot\left(\frac{t}{t_p}\right)\right)} = \frac{v_{j,0}\cdot t_p - \mathcal{Z}_0\cdot\gamma}{(t_p+\gamma\cdot t)}\,. \tag{53}$$

Solving Equation 53 for t, we obtain the former as a function of v_j for a particulated jet:

$$\begin{aligned}t &= \left(\frac{v_{j,0}}{v_j}\right)\cdot\left(\frac{t_p}{\gamma}\right) - \left(\frac{t_p}{\gamma}\right) - \left(\frac{\mathcal{Z}_0}{v_j}\right) \\ &= \left(\frac{t_p}{\gamma}\right)\cdot\left(\frac{v_{j,0}}{v_j}-1\right) - \left(\frac{\mathcal{Z}_0}{v_j}\right)\,.\end{aligned} \tag{54}$$

In order to obtain the crater base velocity u for the particulated jet, the crater depth $\mathbf{P}$ as a function of time t (Equation 50b) must be differentiated with respect to the same, and thus

$$\begin{aligned}u = \frac{\mathrm{d}\,\mathbf{P}}{\mathrm{d}t} &= -\left(\frac{v_{j,0}\cdot t_p}{(t_p+\gamma\cdot t)}\right)\cdot\frac{\mathrm{d}\,(t-t_0)}{\mathrm{d}t} \\ &+ v_{j,0}\cdot t_p\cdot(t-t_0)\cdot\frac{\mathrm{d}\,(t_p+\gamma\cdot t)^{-1}}{\mathrm{d}t}\end{aligned} \tag{55}$$

$$u = \frac{v_{j,0}\cdot t_p}{(t_p+\gamma\cdot t)}\cdot 1 + \frac{v_{j,0}\cdot t_p\cdot(t-t_0)}{(t_p+\gamma\cdot t)^2}\cdot(-1)\cdot\gamma \tag{56a}$$

$$u = \frac{v_{j,0}\cdot t_p\cdot(t_p+\gamma\cdot t) - v_{j,0}\cdot t_p\cdot t\cdot\gamma - v_{j,0}\cdot t_p\cdot t_0\cdot\gamma}{(t_p+\gamma\cdot t)^2} \tag{56b}$$

$$u = \frac{v_{j,0} \cdot t_p \cdot (t_p + \gamma \cdot t_0)}{(t_p + \gamma \cdot t)^2} \tag{56c}$$

Equation 56c can be solved again for time t, whereby t is obtained as a function of the crater base velocity u for a particulated jet:

$$t_p + \gamma \cdot t = \sqrt{\frac{v_{j,0} \cdot t_p \cdot (t_p + \gamma \cdot t_0)}{u}} \tag{57}$$

$$t = \frac{1}{\gamma} \cdot \sqrt{\frac{v_{j,0} \cdot t_p \cdot (t_p + \gamma \cdot t_0)}{u}} - \frac{t_p}{\gamma} \,. \tag{58}$$

For the sake of simplicity the term with the square root will be abbreviated with $\mathfrak{A}$, so:

$$\mathfrak{A} \equiv \sqrt{\frac{v_{j,0} \cdot t_{\mathbf{P}} \cdot (t_p + \gamma \cdot t_0)}{u}} \,. \tag{59}$$

In order to obtain the penetration depth $\mathbf{P}$ as a function of the crater base velocity u, Equation 51 is inserted into Equation 58 with the time t as a function of $\mathbf{P}$, so that we have

$$\frac{\mathbf{P} + \mathcal{Z}_0}{\left(v_{j,0} - \mathbf{P} \cdot \frac{\gamma}{t_p}\right)} = \left(\frac{\mathfrak{A}}{\gamma} - \frac{t_p}{\gamma}\right) \,. \tag{60}$$

By solving Equation 60 for $\mathbf{P}$ we get the following expression:

$$\mathbf{P} + \mathcal{Z}_0 = v_{j,0} \cdot \left(\frac{\mathfrak{A}}{\gamma} - \frac{t_p}{\gamma}\right) - \frac{\mathbf{P} \cdot \gamma}{t_p} \cdot \left(\frac{\mathfrak{A}}{\gamma} - \frac{t_p}{\gamma}\right) \tag{61a}$$

$$\mathbf{P} = \frac{v_{j,0} \cdot \left(\frac{\mathfrak{A}}{\gamma} - \frac{t_p}{\gamma}\right) - \mathcal{Z}_0}{1 + \frac{\gamma}{t_p} \cdot \left(\frac{\mathfrak{A}}{\gamma} - \frac{t_p}{\gamma}\right)} \tag{61b}$$

In order to obtain the crater base velocity u as a function of the penetration depth $\mathbf{P}$ for a particulated shaped charge jet, Equation 60 must be solved for u. Hence

$$\left[\frac{\gamma \cdot (\mathbf{P} + \mathcal{Z}_0)}{v_{j,0} - \mathbf{P} \cdot \frac{\gamma}{t_p}} + t_p\right]^2 = \frac{v_{j,0} \cdot t_p \cdot (t_p + \gamma \cdot t_0)}{u} \tag{62}$$

$$u = \frac{v_{j,0} \cdot t_p \cdot (t_p + \gamma \cdot t_0)}{\left[\frac{\gamma \cdot (\mathbf{P} + \mathcal{Z}_0)}{v_{j,0} - \mathbf{P} \cdot \frac{\gamma}{t_p}} + t_p\right]^2} \,. \tag{63}$$

Finally, the jet velocity v_j is still missing as a function of the crater base velocity u or the latter as a function of the jet velocity v_j for the particulated jet. For this purpose, time t as given by Equation 54 is inserted into Equation 58, whereby v_j is obtained as a function of u, where u is contained in $\mathfrak{A}$:

$$\frac{t_p}{\gamma} \cdot \left(\frac{v_{j,0}}{v_j} - 1\right) - \frac{\mathcal{Z}_0}{v_j} = \frac{\mathfrak{A}}{\gamma} - \frac{t_p}{\gamma} \tag{64}$$

$$\frac{1}{v_j} \cdot \left(\frac{t_p \cdot v_{j,0}}{\gamma} - \mathcal{Z}_0 \right) = \frac{t_p}{\gamma} + \frac{\mathfrak{A}}{\gamma} - \frac{t_p}{\gamma} \tag{65a}$$

$$v_j = \frac{(t_p \cdot v_{j,0} - \gamma \cdot \mathcal{Z}_0)}{\mathfrak{A}} \tag{65b}$$

By resolving Equation 65b to $\mathfrak{A}$ or further to the crater base velocity u one also obtains u as a function of the jet velocity v_j:

$$\mathfrak{A} = \frac{(t_p \cdot v_{j,0} - \gamma \cdot \mathcal{Z}_0)}{v_j} \tag{66}$$

$$u = \frac{v_{j,0} \cdot t_p \cdot (t_p + \gamma \cdot t_0) \cdot v_j^2}{(t_p \cdot v_{j,0} - \gamma \cdot \mathcal{Z}_0)^2} \,. \tag{67}$$

3.2.3 Case II. Crater Base Formation with First Continuous, then Particulated Jet

As is often the case in practice, the most common case is also the most complicated. This case also applies here for the penetration of a shaped charge jet.
The total penetration depth $\mathbf{P}$ is made up of two parts: on the one hand, the continuously penetrating jet part up to the particulation time t_p and, on the other hand, the particulated jet part starting with the jet velocity $v_j(t_p)$.
In general, the total DOP performance can therefore be written as follows: $\mathbf{P}$ (total) = $\mathbf{P}$ (continuous jet) + $\mathbf{P}$ (particulated jet) or

$$\mathbf{P} = \mathbf{P}_c + \mathbf{P}_p \,. \tag{68}$$

Equation 47 must be adapted slightly for the penetration of the particulated jet. Instead of the maximum jet tip speed $v_{j,0}$, the jet velocity $v_j(t_p)$ at the time of particulation t_p is to be used. Equation 68 now reads as follows:

$$\mathbf{P} = \mathbf{P}(t_p) + \frac{(v_j(t_p) - v_j) \cdot t_p}{\gamma} \,. \tag{69}$$

Equation 69 can again be simply solved for to the jet velocity v_j of a jet, which has pierced a material of thickness $\mathbf{P}$, whereby the incoming jet is still continuous and the outgoing jet is then already particulated. Hence

$$v_j = v_j(t_p) - \frac{(\mathbf{P} - \mathbf{P}(t_p)) \cdot \gamma}{t_p} \,. \tag{70}$$

In Equation 69, the DOP performance $\mathbf{P}(t_p)$ can be described up to the particulation time t_p by Equation 31c, although the particulation time t_p must then be used for the time t. Equation 27c can be used for the jet velocity $v_j(t_p)$ at the moment of particulation, but again by using the particulation time t_p for the time t. Equation 69 can thus be written

as follows:

$$\begin{aligned}\mathbf{P} = & v_{j,0}^{\frac{1}{(1+\gamma)}} \cdot \mathcal{Z}_0^{\frac{\gamma}{(1+\gamma)}} \cdot t_p^{\frac{1}{(1+\gamma)}} \\ & - \mathcal{Z}_0 + v_{j,0}^{\frac{1}{(1+\gamma)}} \cdot \mathcal{Z}_0^{\frac{\gamma}{(1+\gamma)}} \cdot t_p^{-\frac{\gamma}{(1+\gamma)}} \cdot \left(\frac{t_p}{\gamma}\right) - \frac{v_j \cdot t_p}{\gamma}\end{aligned} \tag{71}$$

$$\mathbf{P} = \left(1 + \frac{1}{\gamma}\right) \cdot v_{j,0}^{\frac{1}{(1+\gamma)}} \cdot \mathcal{Z}_0^{\frac{\gamma}{(1+\gamma)}} \cdot t_p^{\frac{1}{(1+\gamma)}} - \frac{v_j \cdot t_p}{\gamma} - \mathcal{Z}_0 \tag{72a}$$

$$\mathbf{P} = \frac{(\gamma+1) \cdot (v_{j,0} \cdot t_p)^{\frac{1}{(1+\gamma)}} \cdot \mathcal{Z}_0^{\frac{\gamma}{(1+\gamma)}}}{\gamma} - \frac{v_j \cdot t_p}{\gamma} - \mathcal{Z}_0 \ . \tag{72b}$$

Equation 72b can be presented and written in different variants depending on which values of the three constants, $v_{j,0}$, t_0 or $\mathcal{Z}_0$ are inserted. To simplify the following calculations, an expression $\mathfrak{B}$ is defined according to:

$$\mathfrak{B} \equiv (\gamma+1) \cdot (v_{j,0} \cdot t_p)^{\frac{1}{(1+\gamma)}} \cdot \mathcal{Z}_0^{\frac{\gamma}{(1+\gamma)}} \ , \tag{73}$$

which may also be written in the following variants:

$$\mathfrak{B} = (\gamma+1) \cdot \mathcal{Z}_0 \cdot \left(\frac{t_p}{t_0}\right)^{\frac{1}{(1+\gamma)}} \tag{74a}$$

$$\mathfrak{B} = (\gamma+1) \cdot v_{j,0} \cdot t_0 \cdot \left(\frac{t_p}{t_0}\right)^{\frac{1}{(1+\gamma)}} \tag{74b}$$

$$\mathfrak{B} = (\gamma+1) \cdot v_{j,0} \cdot t_0^{\frac{\gamma}{(1+\gamma)}} \cdot t_p^{\frac{1}{(1+\gamma)}} \ . \tag{74c}$$

Considering these formulæ, Equation 72b may then be written easily in the form:

$$\mathbf{P} = \frac{\mathfrak{B} - v_j \cdot t_p}{\gamma} - \mathcal{Z}_0 \ . \tag{75}$$

Instead of representing the DOP performance $\mathbf{P}$ as a function of the jet velocity v_j, the former may also be represented as a function of the penetrated object $\mathbf{P}$ separated from Equation 72b or in the abbreviated notation from Equation 75. Hence

$$v_j = \frac{(\gamma+1) \cdot (v_{j,0} \cdot t_p)^{\frac{1}{(1+\gamma)}} \cdot \mathcal{Z}_0^{\frac{\gamma}{(1+\gamma)}}}{t_p} - \frac{(\mathbf{P} + \mathcal{Z}_0) \cdot \gamma}{t_p} \tag{76a}$$

$$v_j = \frac{\mathfrak{B} - (\mathbf{P} + \mathcal{Z}_0) \cdot \gamma}{t_p} \, . \tag{76b}$$

In order to obtain the DOP performance $\mathbf{P}$ as a function of the time t, or conversely the time t as a function of the penetration distance $\mathbf{P}$, Equation 15a can be inserted into

Equation 76b. This results in the following equation:

$$\frac{\mathbf{P}+\mathcal{Z}_0}{t} = \frac{\mathfrak{B}-(\mathbf{P}+\mathcal{Z}_0)\cdot\gamma}{t_p} \tag{77}$$

$$(\mathbf{P}+\mathcal{Z}_0)\cdot\left(\frac{t_p}{t}+\gamma\right) = \mathfrak{B} \tag{78a}$$

$$\mathbf{P} = \frac{\mathfrak{B}}{\left(\frac{t_p}{t}+\gamma\right)} - \mathcal{Z}_0 \ . \tag{78b}$$

Solving Equation 77 for t we get

$$t = \frac{t_p\cdot(\mathbf{P}+\mathcal{Z}_0)}{[\mathfrak{B}-(\mathbf{P}+\mathcal{Z}_0)\cdot\gamma]} \ . \tag{79}$$

To obtain the jet velocity v_j as a function of time t, Equation 14 can be inserted into Equation 76b, so that

$$v_j = \frac{\mathfrak{B}-v_j\cdot t\cdot\gamma}{t_p} \tag{80}$$

$$v_j + \frac{v_j\cdot t\cdot\gamma}{t_p} = \frac{\mathfrak{B}}{t_p} \tag{81a}$$

$$v_j = \frac{\mathfrak{B}}{t_p\cdot\left(1+t\cdot\frac{\gamma}{t_p}\right)} = \frac{\mathfrak{B}}{(t_p+t\cdot\gamma)} \ . \tag{81b}$$

To obtain the time t as a function of v_j, we only have to solve Equation 81b for t. We thus get:

$$t = \frac{\mathfrak{B}-v_j\cdot t_p}{v_j\cdot\gamma} \ . \tag{82}$$

In order to obtain the crater base velocity u as a function of time in this case as well, Equation 78b must be differentiated with respect to time:

$$\begin{aligned} u = \frac{\mathrm{d}\,\mathbf{P}}{\mathrm{d}t} &= \frac{\mathrm{d}\left(\frac{\mathfrak{B}}{\frac{t_p}{t}+\gamma}\right)}{\mathrm{d}t} \\ &= -\frac{\mathfrak{B}}{\left(\frac{t_p}{t}+\gamma\right)^2}\cdot\frac{\mathrm{d}\left(\frac{t_p}{t}\right)}{\mathrm{d}t} \end{aligned} \tag{83}$$

$$u = -\frac{\mathfrak{B}}{\left(\frac{t_p}{t}+\gamma\right)^2}\cdot-\frac{t_p}{t^2} = \frac{\mathfrak{B}\cdot t_p}{(t_p+\gamma\cdot t)} \ . \tag{84}$$

By solving Equation 84 for t we get t as a function of the crater base velocity u. Thus:

$$t = \frac{\sqrt{\mathfrak{B}\cdot\frac{t_p}{u}}-t_p}{\gamma} \ . \tag{85}$$

In order to complete the matrix of formulæ, the DOP performance as a function of the crater base velocity u and the latter as a function of the penetration depth $\mathbf{P}$ must be worked out. For this purpose, Equation 78b is used with the DOP performance $\mathbf{P}$ as a function of time t and Equation 85 for the time t as a function of the crater base velocity. From this one obtains:

$$\begin{aligned}\mathbf{P}(u) &= \frac{\mathfrak{B}}{\left(\frac{\gamma \cdot t_p}{\left[\sqrt{\mathfrak{B} \cdot \frac{t_p}{u}} - t_p\right]} + \gamma\right)} - \mathcal{Z}_0 \\ &= \frac{\mathfrak{B}}{\left(\frac{\gamma}{\left[\sqrt{\frac{\mathfrak{B}}{u} \cdot t_p} - 1\right]} + \gamma\right)} - \mathcal{Z}_0 \ . \end{aligned} \tag{86}$$

Solving Equation 86 for u gives:

$$u(\mathbf{P}) = \frac{\frac{\mathfrak{B}}{t_p}}{\left[\frac{1}{\left(\frac{\mathfrak{B}}{\gamma \cdot (\mathbf{P} + \mathcal{Z}_0)} - 1\right)} + 1\right]^2} \cdot \tag{87}$$

In order to obtain the jet velocity v_j as a function of the crater base velocity u for case 2, the jet velocity v_j is used as a function of the time t according to Equation 81b and the time t as a function of the crater base velocity u according to Equation 85. This results in

$$v_j(u) = \frac{\mathfrak{B}}{\left[t_p + \gamma \cdot \frac{\left\{\sqrt{\mathfrak{B} \cdot \frac{t_p}{u}} + t_p\right\}}{\gamma}\right]} \tag{88}$$

$$\begin{aligned} v_j(u) &= \frac{\mathfrak{B}}{\sqrt{\mathfrak{B} \cdot \frac{t_p}{u}}} \\ &= \sqrt{\mathfrak{B} \cdot \frac{u}{t_p}} \, . \end{aligned} \tag{89}$$

By solving Equation 89 for u, the crater base velocity u is obtained as a function of the jet velocity v_j in the form

$$u(v_j) = \frac{v_j^2 \cdot t_p}{\mathfrak{B}} \, . \tag{90}$$

3.2.4 Equation matrix for selection when calculating shaped charges

In the previous section, the DOP capabilities **P**, the times t, the jet velocities v_j and the crater base velocities u were derived as a function of the respective other corresponding partner. This results in a total of 36 formulæ for the three cases – penetration of a continuous, an initially continuous, then particulated and finally a fully particulated jet. To quickly find the desired equation from the derivatives and for quick access to it, the equation matrix according to Table 2 is used, where the ordinate represents the desired quantity , i.e.

1. DOP performance **P**
2. time t
3. jet velocity v_j and
4. crater base velocity u

and where in the abscissa again the respective parameter looked for as part of these four variables is listed for the three possible cases.

For example, if one may want to calculate the DOP performance as a function of time for a continuous jet (case 1), one has to use Equation 30, for case 2 – first continuous and then particulated penetration – Equation 77. The required equation may be found quickly and easily from this matrix.

If there are formulæ with sub-items, e.g. Equation 30, Equation 31a, Equation 31b, etc., this means that these formulæ always give the same final result. However, the reader can choose the equation for which he has the corresponding constants.

Cases	continuous jet				continuous and particulated jet				particulated jet			
	quantity measured and available, respectively											
quantity looked for	**P**	t	v_j	u	**P**	t	v_j	u	**P**	t	v_j	u
P	–	Equation 30	Equation 34	Equation 38	–	Equation 77	Equation 71	Equation 86	–	Equation 49	Equation 47	Equation 60
t	Equation 32	–	Equation 28	Equation 40	Equation 79	–	Equation 82	Equation 85	Equation 51	–	Equation 54	Equation 57
v_j	Equation 36	Equation 26	–	Equation 47	Equation 76b	Equation 80	–	Equation 88	Equation 48	Equation 52	–	Equation 64
u	Equation 37	Equation 39	Equation 7	–	Equation 87	Equation 83	Equation 90	–	Equation 62	Equation 55	Equation 66	–

Table 2: Matrix of formulæ to be determined for all applications depending on the individual variables
$\mathfrak{A}$ = Equation 59
$\mathfrak{B}$ = Equation 73

3.2.5 Theoretical maximum DOP performance P_m

The cratering increase ends when the jet, for whatever reason, no longer provides any increase of power for the DOP effect. This is then given by the minimum effective jet velocity $\mathrm{v_{j,min.}}$. In the formulæ, the jet velocity v_j must then be replaced by the minimum effective jet velocity $\mathrm{v_{j,min.}}$, which then results in the maximum possible DOP performance "at least theoretically".
The maximum DOP performance $\mathbf{P}_m$ as a function of $\mathrm{v_{j,min.}}$ can now be described for the three cases by the formulæ for case 1 by Equation 35c, case 2 by Equation 72b and case 3 by Equation 47. The formulæ will be repeated here for the sake of clarity:

$$\boxed{\text{Case I.:}\quad \mathbf{P}_m = \mathcal{Z}_0 \cdot \left[\left(\frac{v_{j,0}}{\mathrm{v_{j,min.}}} \right)^{\frac{1}{\gamma}} - 1 \right]} \tag{91}$$

$$\boxed{\text{Case II.:}\quad \mathbf{P}_m = \frac{(\gamma+1)\cdot(v_{j,0}\cdot t_p)^{\frac{1}{(1+\gamma)}}}{\gamma} \cdot \frac{\mathcal{Z}_0^{\frac{\gamma}{(1+\gamma)}} - \mathrm{v_{j,min.}} \cdot t_p}{\gamma} - \mathcal{Z}_0} \tag{92}$$

$$\boxed{\text{Case III.:}\quad \mathbf{P}_m = \frac{(v_{j,0} - \mathrm{v_{j,min.}})\cdot t_p}{\gamma}} \tag{93}$$

3.2.6 Description of Graphical Representation

The formulæ derived in the previous chapter can also be graphically illustrated in the DOP performance diagram as a function of the distance $\mathcal{Z}_0$, the so-called distance diagram (Figure 18). This diagram shows quite clearly the possibilities for calculating the residual DOP performance on the one hand and the residual maximum jet tip speeds on the other.

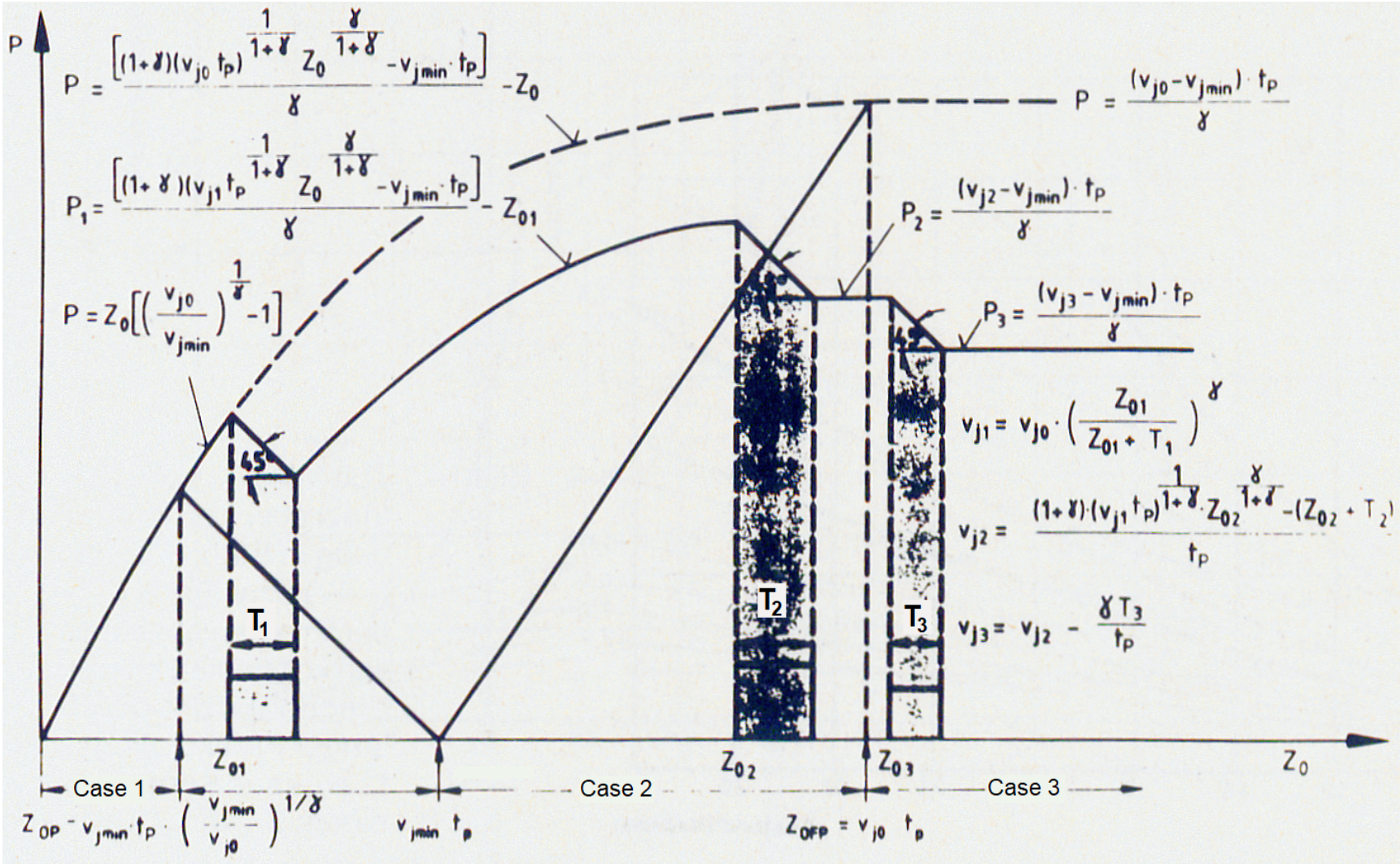

Figure 18: Theoretically possible DOP performance of a shaped charge jet as a function of distance, whereby thin blasting objects with thicknesses T_1, T_2 and T_3 are located at specified distances $\mathcal{Z}_{0,1}$, $\mathcal{Z}_{0,2}$, $\mathcal{Z}_{0,3}$

Thus, according to Equation 35c, the DOP performance for crater formation, for which the continuous jet alone is responsible, increases linearly with the distance $\mathcal{Z}_0$. Beginning with distance

$$\mathcal{Z}_{0,P} = \mathrm{v_{j,min.}} \cdot t_p \cdot \left(\frac{\mathrm{v_{j,min.}}}{v_{j,0}} \right)^{\frac{1}{\gamma}}$$

(Corresponds to Equation 45) the jet first begins to penetrate continuously and then particulated. Equation 72b applies to this case 2. This range extends up to $\mathcal{Z}_{0,P} = v_{j,0} \cdot t_p$, from which point the jet tip is already particulated. Equation 47 then applies to case 3.

If the jet has perforated a target plate of thickness T_1 at a distance $\mathcal{Z}_{0,1}$ with the maximum jet tip speed $v_{j,0}$, Equation 35c must be applied with the now valid residual maximum jet tip speed $v_{j,1}$ instead of $v_{j,0}$ if the exiting jet – case 1 – is still continuous in terms of its shape. However, if the residual DOP performance $\mathbf{P}_1$ already falls into the range of case 2, then Equation 72b must be used. However, instead of the maximum jet tip speed $v_{j,0}$ the residual maximum jet tip speed $v_{j,1}$ according to Equation 36 and instead of $\mathcal{Z}_0$ the distance $\mathcal{Z}_{0,1}$ must be used.

If another plate T_2 is perforated at the distance $\mathcal{Z}_{0,2}$, whereby in this example a particulated shaped charge jet now exits, then Equation 47 must be applied. For the maximum jet tip speed $v_{j,0}$, however, the corresponding residual maximum jet tip speed $v_{j,2}$ must be used. After penetrating the second target plate T_2, $v_{j,2}$ results from Equation 76a, but with $v_{j,1}$ instead of $v_{j,0}$ and $\mathcal{Z}_{0,2}$ instead of $\mathcal{Z}_0$.

If the purely particulated jet has to perforate an additional plate of thickness T_3 at a distance $\mathcal{Z}_{0,3}$, then Equation 47 must be applied again, whereby the residual maximum jet tip speed $v_{j,3}$ can be calculated for the possible residual DOP performance according to Equation 48 with $v_{j,3}$ instead of $v_{j,0}$.

3.2.7 Influence of Maximum Jet Tip Speed $v_{j,0}$ on the DOP Performance

The significance of a high maximum jet tip speed $v_{j,0}$ for high a DOP performance can be determined relatively easily from the previous formulæ. For the sake of simplicity, the jet and target material should be identical so that the value for γ is equal to 1. Furthermore, a constant value of $3\,\mathrm{mm\,\mu s^{-1}}$ should be assumed for $\mathrm{v_{j,min.}}$.

Then for case 1 – cratering exclusively with a continuous jet – the values of numerical Table 3 result for the ratio $\mathbf{P}_m \,/\, \mathcal{Z}_0$ when the maximum jet tip speed $v_{j,0}$ changes.

As can be seen, the DOP performance $\mathbf{P}_m \,/\, \mathcal{Z}_0$ increases with an increase in the jet velocity from the maximum jet tip speed $v_{j,0}$ of $6\,\mathrm{mm\,\mu s^{-1}}$ to $9\,\mathrm{mm\,\mu s^{-1}}$ by a factor of 2 or from $6\,\mathrm{mm\,\mu s^{-1}}$ to $12\,\mathrm{mm\,\mu s^{-1}}$ by a factor of 3.
The ratios are identical for the maximum DOP performances by a fully particulated shaped charge jet (case 3) if the same values as above are used (Table 4).

In case 3 we also see that by increasing the jet speed from $6\,\mathrm{mm\,\mu s^{-1}}$ to $9\,\mathrm{mm\,\mu s^{-1}}$ the theoretical possible DOP increase is twofold and by increasing from $6\,\mathrm{mm\,\mu s^{-1}}$ to

$v_{j,0}$ in $\mathrm{mm\,\mu s^{-1}}$	$\frac{v_{j,0}}{\mathrm{v_{j,min.}}}$	$\frac{\mathbf{P}_m}{\mathcal{Z}_0}$
6	2	1
9	3	2
12	4	3

Table 3: The ratio of maximum DOP performance $\mathbf{P}_m$ to distance $\mathcal{Z}_0$ as a function of the maximum jet tip speed $v_{j,0}$ in case 1

$v_{j,0}$ in $\mathrm{mm\,\mu s^{-1}}$	$(v_{j,0} - \mathrm{v_{j,min.}}) = \mathbf{P}_m \cdot \frac{\gamma}{t_p}$
6	3
9	6
12	9

Table 4: The DOP performance increase as a function of the maximum jet tip speed $v_{j,0}$ in case 3

$12\,\mathrm{mm\,\mu s^{-1}}$ the gain of DOP increase is threefold. The influence of the maximum jet tip speed is therefore identical for case 1 and case 3.

The formulæ at least indicate how important high maximum jet tip speeds are for maximum DOP performance for shaped charges.

4 Validation of the Hydrodynamical Theory of Penetration of a Shaped Charge Jet into Concrete and Sand in Comparison to Steel

4.1 General Remarks

Figure 19 shows the crater formation of a copper jet as a function of the time of a theoretically assumed exclusively continuous shaped charge jet (case 1). This has a maximum jet tip speed $v_{j,0}$ of $8.5\,\mathrm{mm\,\mu s^{-1}}$ against three target materials – steel with a density of $7.85\,\mathrm{g\,cm^{-3}}$, concrete with a density of $2.4\,\mathrm{g\,cm^{-3}}$ and sand with a density of $1.3\,\mathrm{g\,cm^{-3}}$ – and is detonated at a distance of three times the charge diameter (= three caliber distance) from the virtual origin. This diagram in Figure 19 also shows the so-called "jet fan". This means that the intersections of the velocity lines with the crater base formation curves mark the jet velocities that occur at these points and thus become effective there.

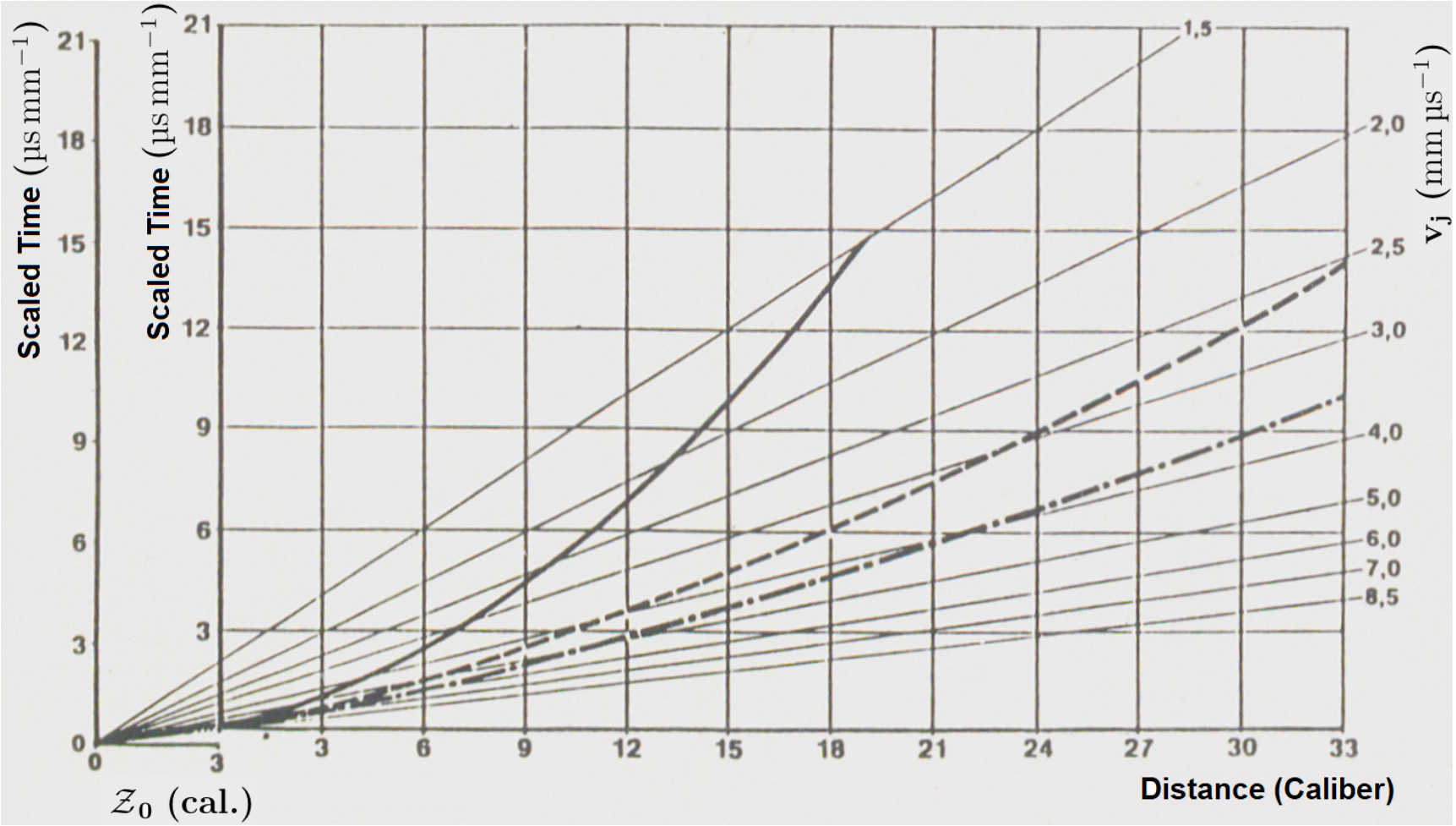

Figure 19: Time-distance curves of theoretical crater formation in steel (solid line), concrete (dashed line), or sand (dashed-dotted line) by a solely continuous shaped charge jet with infinitely long particulation time $t_p = \infty$ made of copper at a $\mathcal{Z}_0$ of 3 calibers

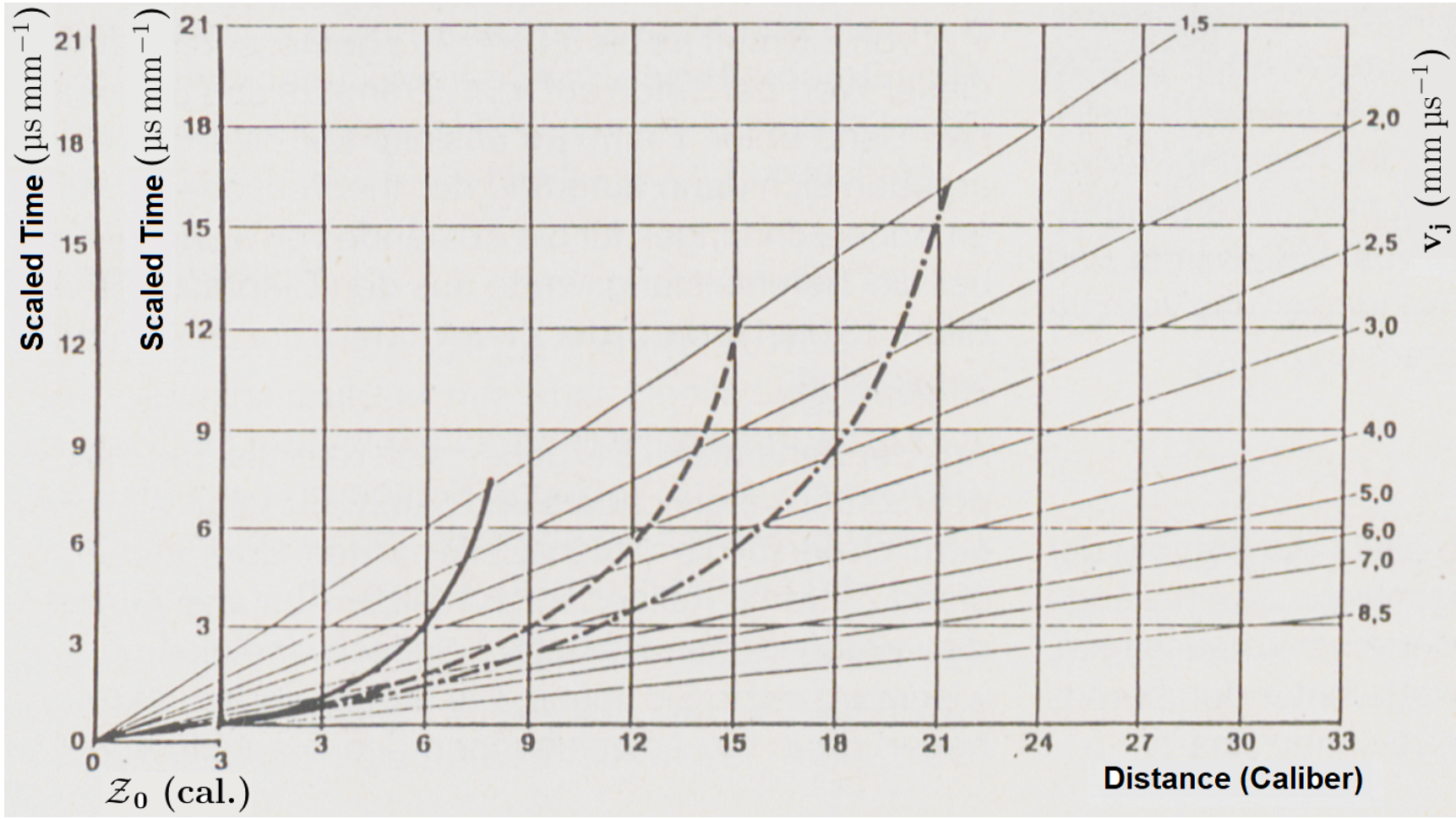

Figure 20: Time-distance curves of theoretical crater formation against steel, concrete and sand by a shaped charge jet made of copper with a scaled particulation time t_p of 1.3 µs mm^{-1} at a $\mathcal{Z}_0$ of 3 calibers

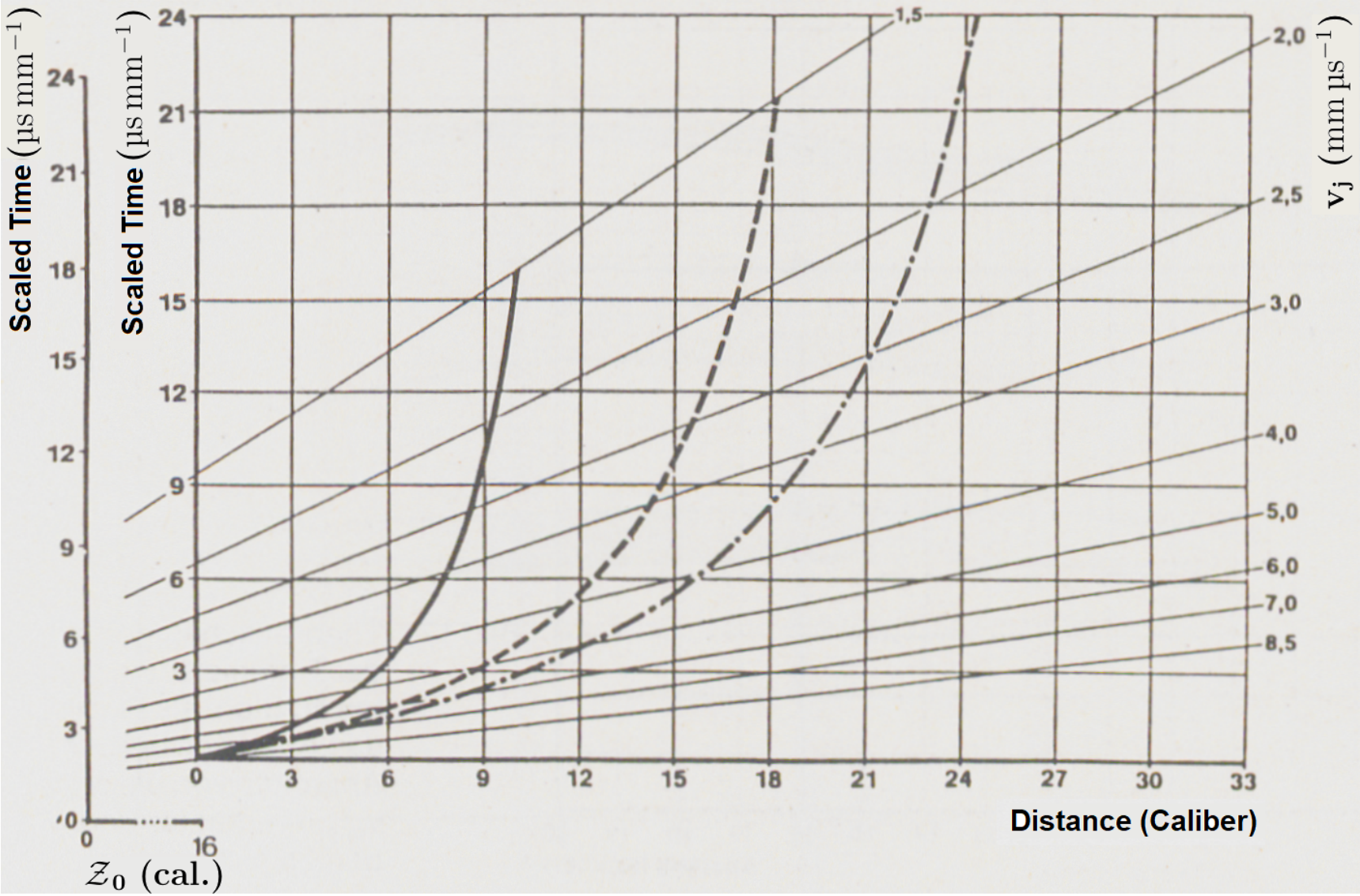

Figure 21: Time-distance curves of theoretical crater formation against steel, concrete and sand by a shaped charge jet made of copper with a scaled particulation time t_p of $1.3\,\mu s\,mm^{-1}$ at a $\mathcal{Z}_0$ of 16 calibers

		DOP Performance			Relations	
$\mathcal{Z}_0$, (cal.)	t_p, ($\mu s\,mm^{-1}$)	Steel, (cal.)	Concrete, (cal.)	Sand, (cal.)	$\mathbf{P}_C\,/\,\mathbf{P}_{St}$	$\mathbf{P}_S\,/\,\mathbf{P}_{St}$
3	∞	(19)	(82)	(530)	(4.3)	(28)
3	1.3	7.6	15	21	2.0	2.8
16	1.3	10	18	24	1.8	2.4

Table 5: Theoretically derived DOP performances and their ratios to each other for steel, concrete and sand at a constant minimum effective residual jet velocity $v_{j,\min}$ of $1.5\,mm\,\mu s^{-1}$

The far more realistic case of crater base formation against the same materials of an initially continuous and, after $1.93\,\mu s\,mm^{-1}$, particulated shaped charge jet (case 2), blasted at the same distance from the virtual origin, is shown in Figure 20. As the shaped charge jet no longer stretches and elongates infinitely, the achievable DOP performance is understandably considerably lower.

Furthermore, the penetration depth values of an exclusively particulated shaped charge jet (case 3), now blasted at a distance of 16 calibers from the virtual origin, are shown against the three materials in Figure 21. In Table 5 the theoretically derived DOP performances are listed. These can also be easily read from Figure 19, Figure 20 and Figure 21. Three cases were compared with

1. 3 caliber and particulation time $t_p = \infty$,
2. 3 caliber distance and particulation time t_p after $1.3\,\mu s\,mm^{-1}$,
3. 16 caliber distance after a particulation time of $1.3\,\mu s\,mm^{-1}$.

For the three cases with constant minimum effective residual jet velocity $v_{j,\min}$ of $1.5\,mm\,\mu s^{-1}$, the time-to-distance curves against steel, concrete and sand are shown. Table 5 also contains the derivable ratios of the DOP performance $\mathbf{P}_C$ or $\mathbf{P}_S$ in concrete or sand compared to steel $\mathbf{P}_{St}$.

The values of the top line in Table 5 are set in brackets, as they reflect the non-realistic case of an infinitely long elongated shaped charge jet. The second line gives somewhat more realistic values for 3 caliber blasting distance. However, the ratios $\mathbf{P}_C\,/\,\mathbf{P}_{St}$ or $\mathbf{P}_S\,/\,\mathbf{P}_{St}$, with 2.0 or 2.8 respectively, are greater than the ratios of the respective root expressions

$$\sqrt{\frac{\rho_{St}}{\rho_C}} = \sqrt{\frac{7.85}{2.4}} \cong 1.8 \text{ bzw.}$$
$$\sqrt{\frac{\rho_{St}}{\rho_S}} = \sqrt{\frac{7.85}{1.3}} \cong 2.4\,.$$

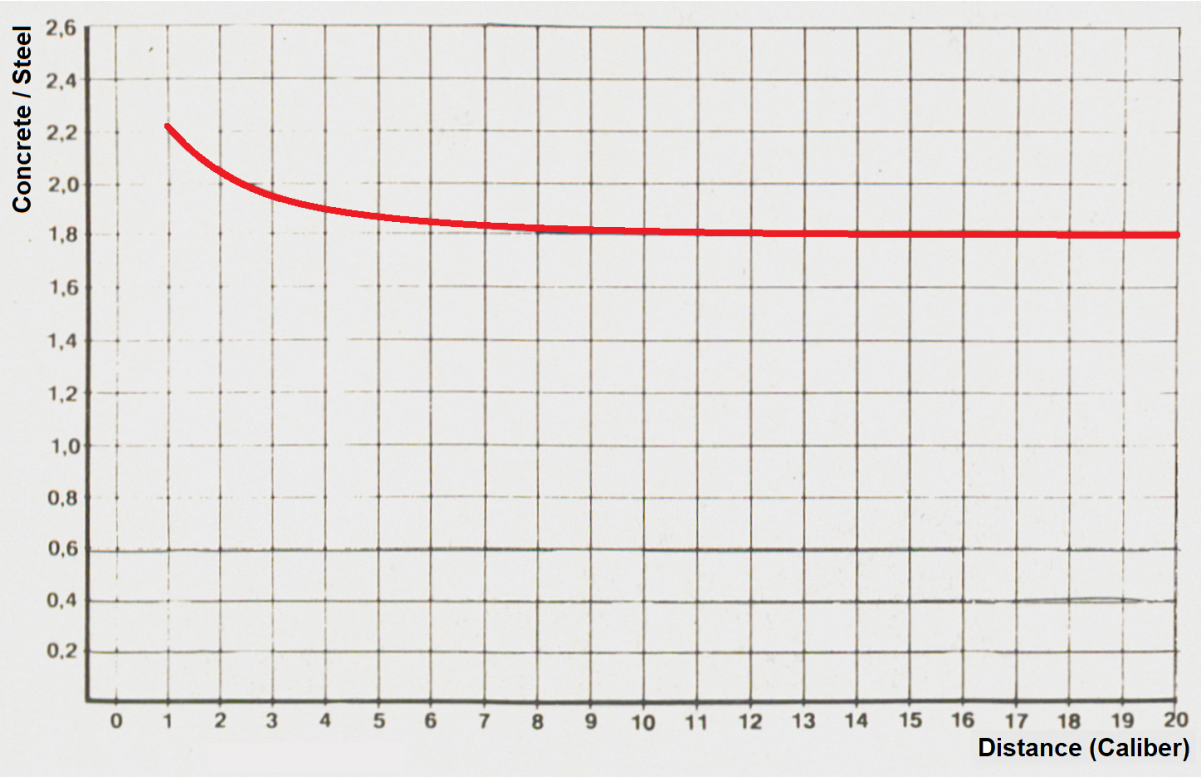

Figure 22: Theoretical ratio of DOP performance in concrete to steel as a function of the distance assuming equal $v_{j,\min}$-values (not correct based on experience)

At close range, the shaped charge jet penetrates the less dense material faster and deeper, so that it then stretches and elongates further than in a denser material. It therefore assumes a greater effective length in the less dense material. In Figure 22, the theoretical ratio $\mathbf{P}_C \,/\, \mathbf{P}_{St}$ is shown as a function of the distance, whereby from a distance of 11 calibers at the given scaled particulation time of $1.3\,\mu s\,mm^{-1}$ and $8.5\,\mu s\,mm^{-1}$ maximum jet tip speed, the ratio is then constant at 1.8 – corresponding to

$$\sqrt{\frac{\rho_{St}}{\rho_C}} = \sqrt{\frac{7.85}{2.4}}$$

The sum of the shaped charge jet particles and thus the actual jet length remains constant from the point of particulation. The last line again gives predictions that should only be seen as rough guide values under the assumptions already given above.

The specified minimum effective residual jet velocity $v_{j,\min}$ of $1.5\,mm\,\mu s^{-1}$ is neither constant for the different materials nor for different blasting distances. At slow residual velocities, the strength of the material can no longer be neglected. On the other hand, the jet elements, which become thicker in diameter as the velocity slows down and which also frequently tumble and drift crosswise due to the particulation process, hit the crater rim, atomize there and thus fail for further crater deepening. The latter effect occurs earlier with firmer material, as the hole-shaped channel becomes smaller in diameter with increasing material strength. This means that $v_{j,\min}$ already changes when different types of steel are changed. In high-strength steel, for example, the shaped charge jet penetrates

DOP Performance					Relations	
Material		Steel, (cal.)	Concrete, (cal.)	Sand, (cal.)		
Density, $\mathrm{g\,cm^{-3}}$		7.85	2.4	1.3		
$v_{j,\min}$, $\mathrm{mm\,\mu s^{-1}}$		3	1.5	1		
$\mathcal{Z}_0$, (cal.)	t_p, $(\mathrm{\mu s\,mm^{-1}})$				$\mathbf{P}_C\,/\,\mathbf{P}_{St}$	$\mathbf{P}_S\,/\,\mathbf{P}_{St}$
3	∞	(7)	(82)	(800)	(12)	(114)
3	1.3	6.5	15	22	2.3	3.4
16	1.3	7.6	18	29	2.4	3.82

Table 6: DOP performance values for the distances of 3 and 16 caliber based on theoretical crater base calculations in steel, concrete and sand

about 20 % less deeply than in soft iron for this reason.

For high-quality steel, effective residual jet velocities $v_{j,\min}$ of $2.5\,\mathrm{mm\,\mu s^{-1}}$ to $3.0\,\mathrm{mm\,\mu s^{-1}}$, are measured for blasting at close range, while this value drops to around $1.5\,\mathrm{mm\,\mu s^{-1}}$ for concrete and below $1\,\mathrm{mm\,\mu s^{-1}}$ for loose sand. With these values, the theoretical crater base calculations for the distances of 3 and 16 calibers then result in the DOP performance values from the diagrams of Figure 18 to Figure 20, which are summarized in Table 6.

From Table 6, realistic, experimentally comparable and thus permissible values basically only result for the middle line with the blasting distance $\mathcal{Z}_0$ of 3 caliber. At a distance of 16 calibers, the specified residual jet velocities $v_{j,\min}$ are again not correct. As previously explained, they are higher, because the deviations of the shaped charge jet from the axis and the wobbling and transverse drift movements of the particulated jet parts are much more significant at larger blasting distances.

It should be emphasized here that the formulæ are based solely on purely hydrodynamic penetration. Start-up phenomena when the particles hit the blast object on the one hand, as well as secondary penetration, [4], and wake effects, [2], when the shaped charge jet particles are already completely consumed, are not taken into account in the present case. However, such effects must be taken into account when a particulated shaped charge jet penetrates into soft and not very firm materials.

4.2 Experiments

4.2.1 Blast Experiments against Blocks of Concrete

The tests were carried out with a shaped charge according to Figure 1 with controlled detonation wave direction and copper lining with a maximum jet tip speed $v_{j,0}$ of $8.5\,\mathrm{mm\,\mu s^{-1}}$ and a mean scaled particulation time t_p of about $1.3\,\mathrm{\mu s\,mm^{-1}}$.

The shaped charge was blasted at different distances from the concrete blocks. Figure 23 shows a typical experimental setup, with a large number of concrete cubes arranged in the direction of action of the shaped charge. To determine the crater base formation as a function of time, contact foils were placed both on the face and between the individual concrete blocks. The pulses as a function of time were recorded with a transient recorder. The individual pulses can be recorded both on the oscilloscope and on a XY recorder. The relatively small but reinforced concrete blocks were completely destroyed by the penetrating shaped charge jet, especially in the initial area (see Figure 24).

The DOP performances of the blasting tests against the concrete blocks used are shown in the distance diagram of Figure 25 with their scatter range, compared to earlier blasting experiments against steel and soft iron. The results show an average DOP performance of around 15.5 calibers at a distance of 2 calibers, which increases to 16 calibers at a blasting distance of 2 to 4 calibers, only to drop again to around 14 calibers at a distance of 10 calibers. However, the results are in any case significantly higher than the root ratio of the densities of steel and concrete, which would result in caliber depths of around 10 to 13, depending on whether the DOP performance in high-quality and solid steel or soft iron is used as a reference Figure 25, medium range).
If one compares the DOP values derived with the square root of the density ratio according to Equation 5 in relation to high-strength steel or soft iron, one finds that the experimental results are around 50 % above the curve for high-strength steel and around 30 % above the curve for soft iron.

The increased perforation performance against concrete compared to soft iron or high-strength steel is constant to a first approximation at the investigated distance of 2 to 10 calibers. Instead of the value 1.8 from the square root ratio of the densities, a factor of about 2.25 results for soft iron and 2.7 for steel (see Figure 26). At least the first value of 2.25 is quite close to that of $\mathbf{P}_C \,/\, \mathbf{P}_{St}$ of Table 6 with 2.30.

This result becomes very clear if the additive perforation performance rates of the shaped charge jet per velocity interval are also drawn into the distance curves, which are supplemented by further tests up to a distance of 20 calibers, and thus finally give the so-called “incremental distance curve” (see Figure 27). From the intersection points of the distance curve with the possible DOP performance values down to the respective velocities, at least an estimate for the minimum effective residual jet velocity $v_{j,\min}$, [10], is obtained. From Figure 27 the $v_{j,\min}$ values for steel, soft iron and concrete listed in Table 7 can be seen as a function of the distance.

Much larger concrete blocks are no longer broken up by the shock waves that occur when the shaped charge jet perforates them. The holes that form when the jet enters and exits with a few rudiments of a spalling layer of the otherwise still completely intact concrete block are shown in Figure 28. The DOP performance values are about 15 % less compared to the smaller blocks. Concrete blocks with different strengths were also investigated. Slightly lower DOP performances were also determined for the large blocks with higher strength. This means that a tinier hole-shaped channel is created in the non-fracturing and higher strength concrete blocks, which no longer allows the residual

$\mathcal{Z}_0$ (cal.)	$v_{j,\min}$ ($\mathrm{mm\,\mu s^{-1}}$) for ..... high strength steel	soft iron	concrete
2	2.5	2.0	1.3
6	3.7	2.8	2.2
10	4.8	3.8	2.8
20	6.7	6.0	4.2

Table 7: Smallest effective minimum effective residual jet velocity $v_{j,\min}$ for steel, soft iron and concrete in dependence of distance $\mathcal{Z}_0$

shaped charge jet to perforate the former. This is then expressed by slightly lower DOP performances or slightly higher $v_{j,\min}$ values. The strength and size of the concrete blocks must be taken into account – especially when comparing tests from the literature with one's own results.

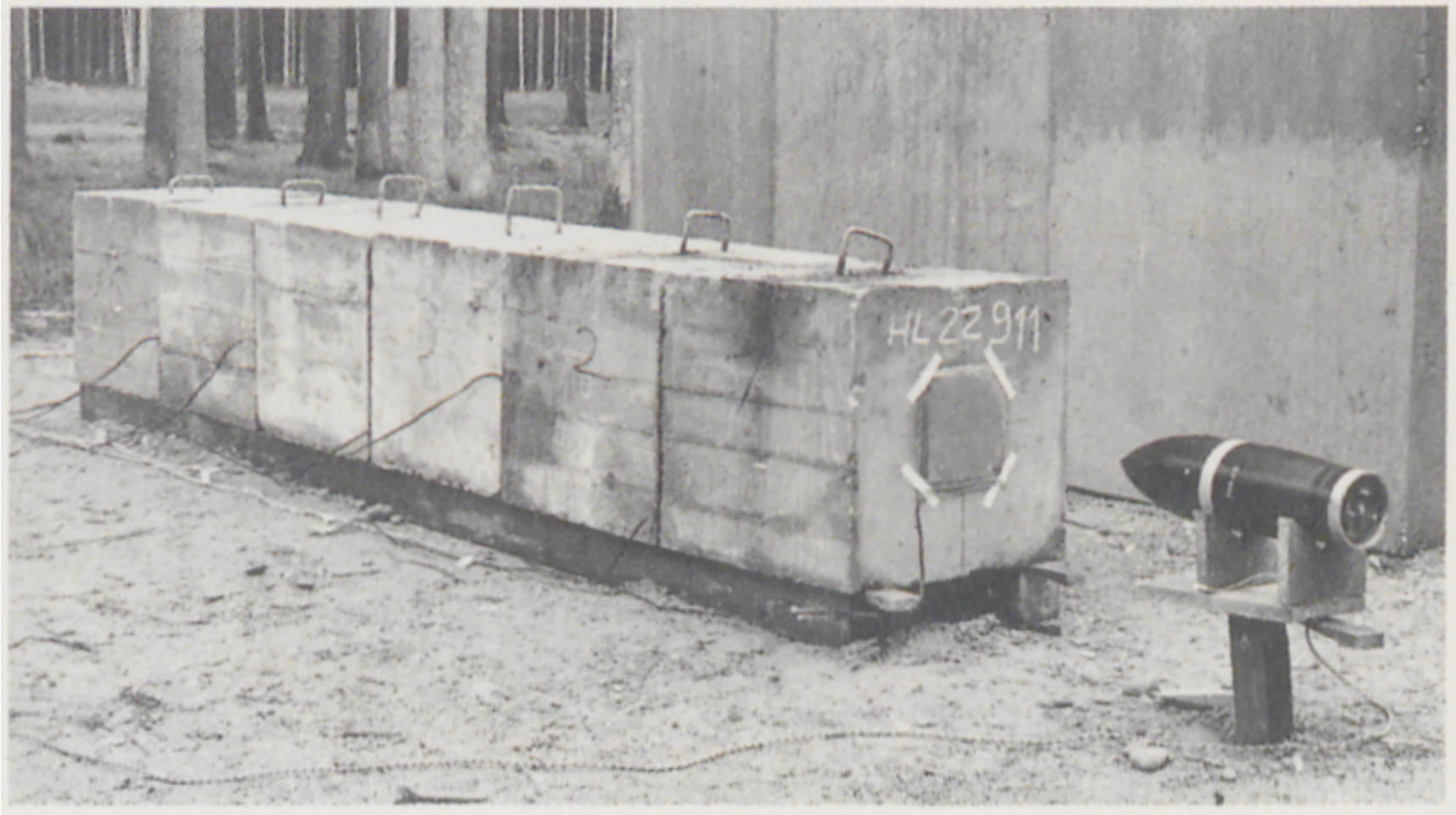

Figure 23: Experimental setup for blasting a shaped charge against concrete blocks with contact foils between them

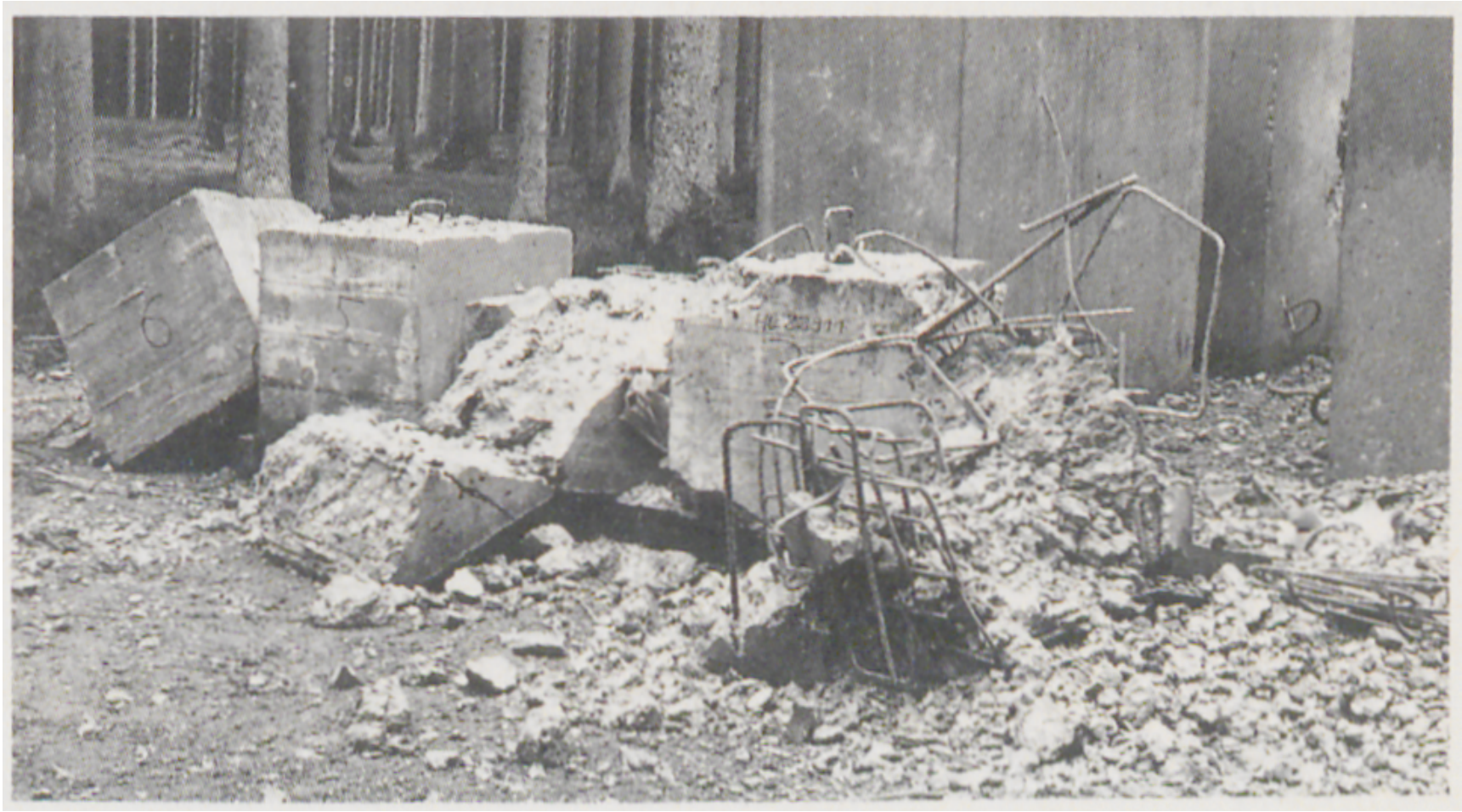

Figure 24: The debris of the concrete blocks in Figure 23 after the blast

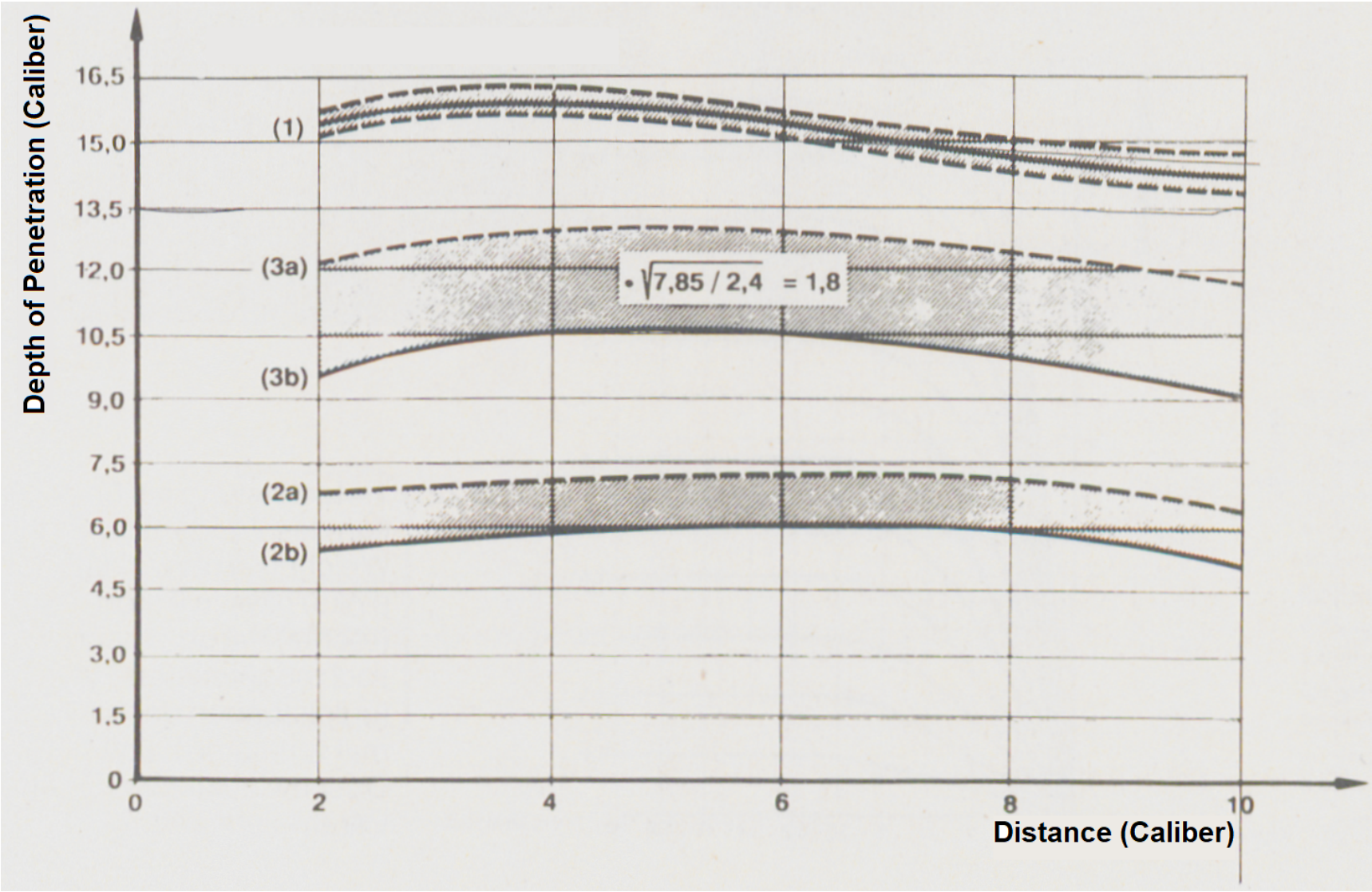

Figure 25: Experimentally obtained DOP performances as a function of the distance in concrete (1), soft iron (2a) and steel (2b). With the "incorrect" extrapolation based on the square root-ρ law, only the DOP performance values relating to soft iron (3a) and high-quality steel (3b) would result

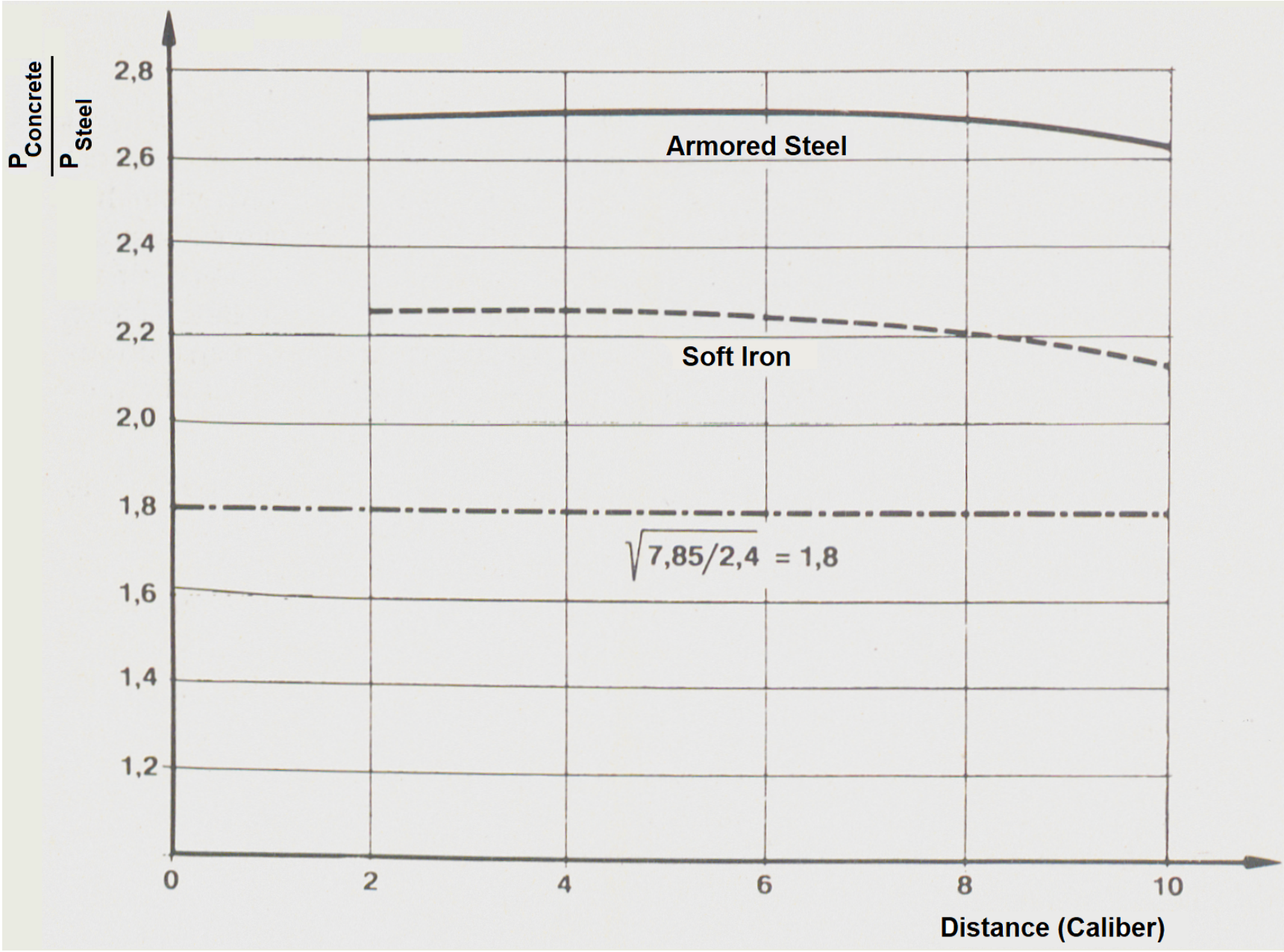

Figure 26: Comparison of the ratios of the experimentally achieved DOP performances in concrete to soft iron or to steel compared to the theoretical square root ratio of 1.8

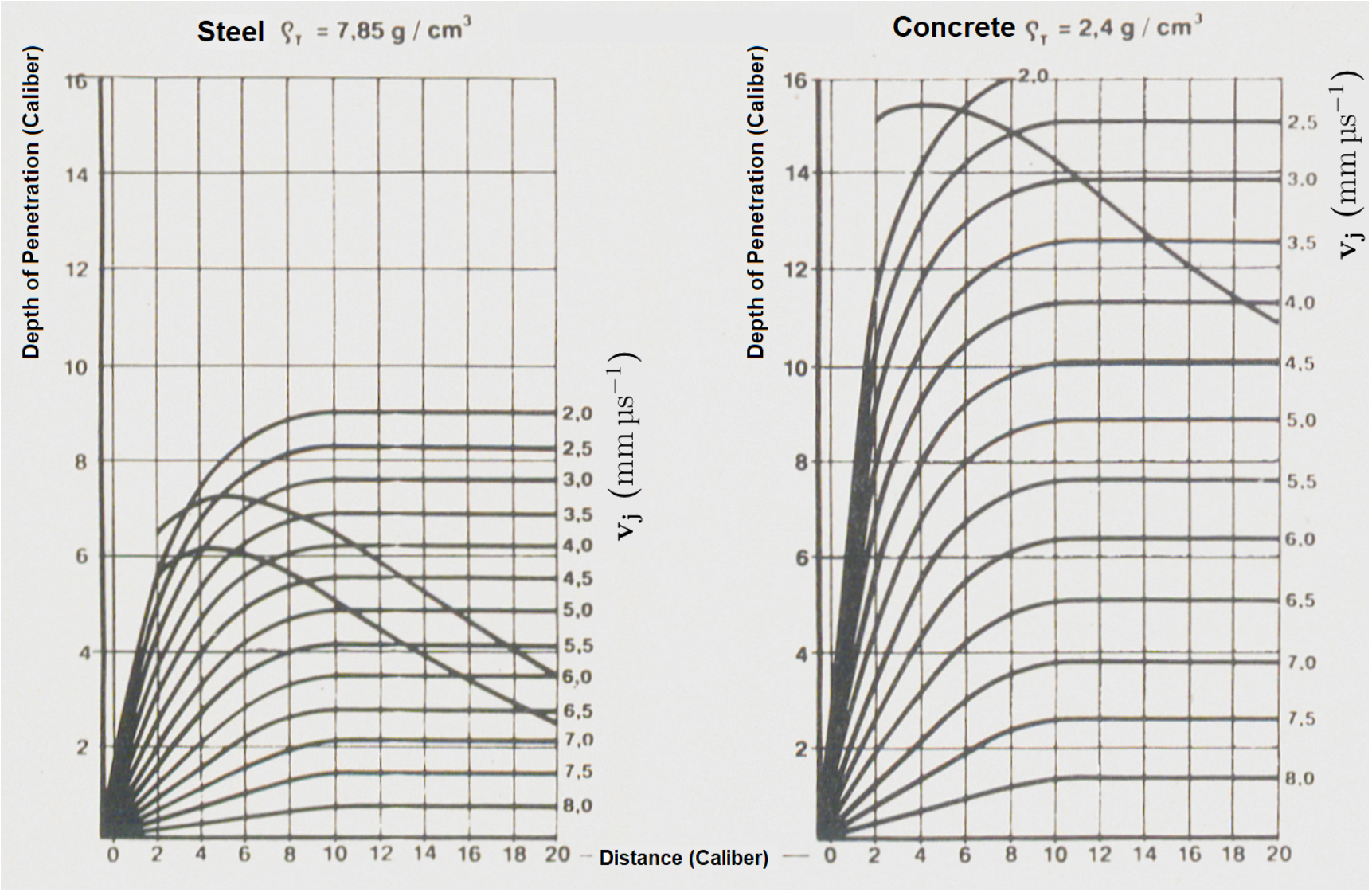

Figure 27: DOP performance as a function of the ignition distance in soft iron or steel (left) or in concrete (right) with the theoretically derived DOP performance of the minimum effective residual jet velocity $v_{j,\min}$ in the form of parameter lines

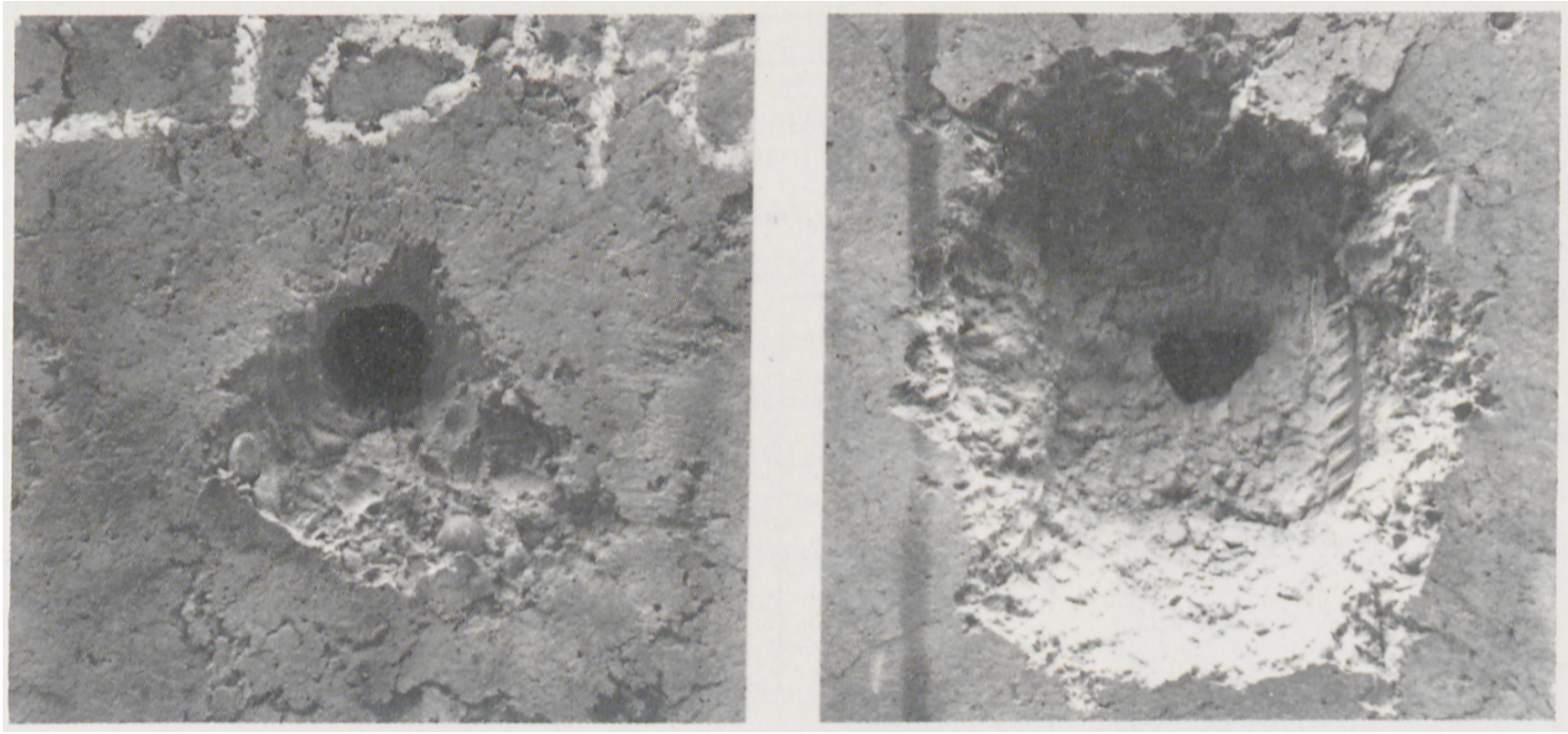

Figure 28: Entry and exit hole of a shaped charge jet in a larger and high strength concrete block than the one shown in Figure 23 and Figure 24

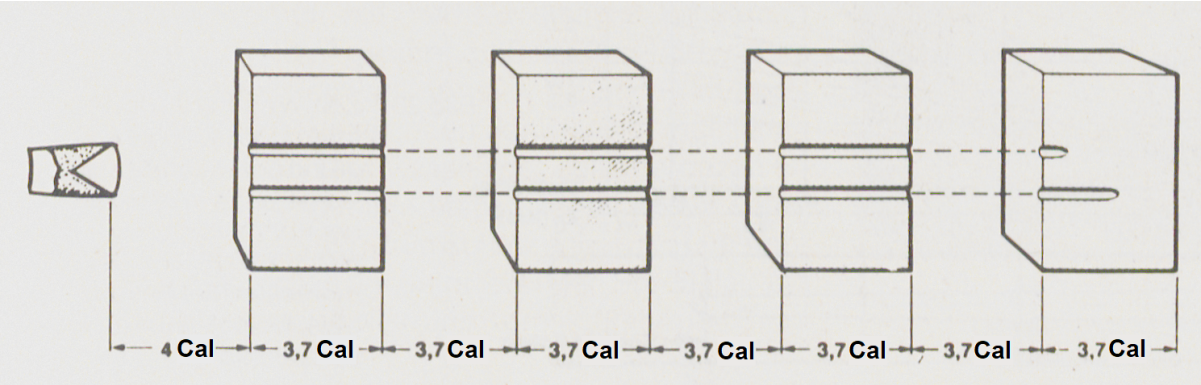

Figure 29: Experimental setup and blasting result with four concrete cubes arranged at defined distances

This type of shaped charge was also used to detonate bulkheaded concrete targets, which consisted of cube-shaped concrete blocks with an edge length of 3.7 times the caliber of the shaped charge, and which were arranged at a distance of 3.7 calibers from each other (see Figure 29). If one compares the results obtained in this experimental setup with a graphical determination of the proportionality method using the distance curve, [10], then the results agree quite well with each other if a reduction factor of about 13 % is taken into account for each distance (Figure 30). This value is a commonly used reduction factor determined from experience for plates made of high-quality steel, which are mounted at defined distances from each other.

In other words, this means that the residual DOP performance against concrete blocks in a bulkhead arrangement can also be determined graphically or mathematically from the distance curve of a shaped charge against concrete targets using the so-called proportionality method.

As explained at the beginning, the perforation times of the shaped charge jet through the concrete blocks were also measured, [8]. Figure 31 shows the experimentally determined distance-to-time curve of the crater base formation, albeit with only four internal measuring points, compared to the theoretical prediction. The experimental values are in good agreement with the theoretically calculated crater base formation, although the constant particulation time of $1.3\,\mu s\,mm^{-1}$ for the entire shaped charge jet is certainly a simplification. The most important measuring point is the one after the fourth block after 14.7 caliber penetration distance. This represents almost the end of the crater base formation. The diagram shows that the jet was effective down to $2.2\,mm\,\mu s^{-1}$. This is in very good agreement with the incremental distance diagram (see Figure 27). For 4.5 caliber distance at 14.7 caliber DOP performance, which is slightly below the distance curve sketched there, which was blasted with smaller concrete blocks, a value of $2.1\,mm\,\mu s^{-1}$ can be read for $v_{j,\min}$.
In Figure 33 the four experimental values are replotted and evaluated statistically. The values can be approximated using an exponential function. The result is:

$$\text{DOP} = 0.472 \cdot e^{\frac{1}{5}x}$$

with fitting parameters according to Table 8.

The measurement of the shaped charge jet perforation times or the respective residual maximum jet tip speeds in concrete blocks, which are arranged at certain (bulkheaded) distances from each other, also agrees well with the theoretical calculations, at least in or after the first two blocks (see Figure 32).
In Figure 34 the experimental values are replotted and statistically evaluated. Also, as in Figure 31 the values can be best approximated with an exponential function according to

$$\text{Distance } = 0.120 \cdot e^{0.237x}$$

and with fitting parameters according to Table 9.

The good agreement between theory and experiment for the temporal crater base formation means that the hydrodynamic theory for the latter, taking into account the jet gradient, also retains its validity for concrete despite the considerable simplifications in the approaches.

sum of quadratic errors (χ^2)	0.0351769
remaining mean square (χ^2/dof)	0.0117256
square root of mean quadratic error (RMSD/SD)	0.108285
coefficient of determination (R^2)	0.998883
corrected coefficient of determination (R^{-2})	0.997766
χ^2-Test ($P > \chi^2$)	0.998
F-Test	2.68E+03
P > F	1.32E-05
mean absolute error (MAE)	0.0647596
Akaik's information criteria (AIC)	-4.59
Bayesian information criteria (BIC)	-5.77

Table 8: Goodness of adaption for plot shown in Figure 33

sum of quadratic errors (χ^2)	1.13025
remaining mean square (χ^2/dof)	0.282562
square root of mean quadratic error (RMSD/SD)	0.531566
coefficient of determination (R^2)	0.97247
corrected coefficient of determination (R^{-2})	0.954117
χ^2-Test ($P > \chi^2$)	0.889
F-Test	141
P > F	0.000195
mean absolute error (MAE)	0.356876
Akaik's information criteria (AIC)	13
Bayesian information criteria (BIC)	12.4

Table 9: Goodness of adaption for plot shown in Figure 34

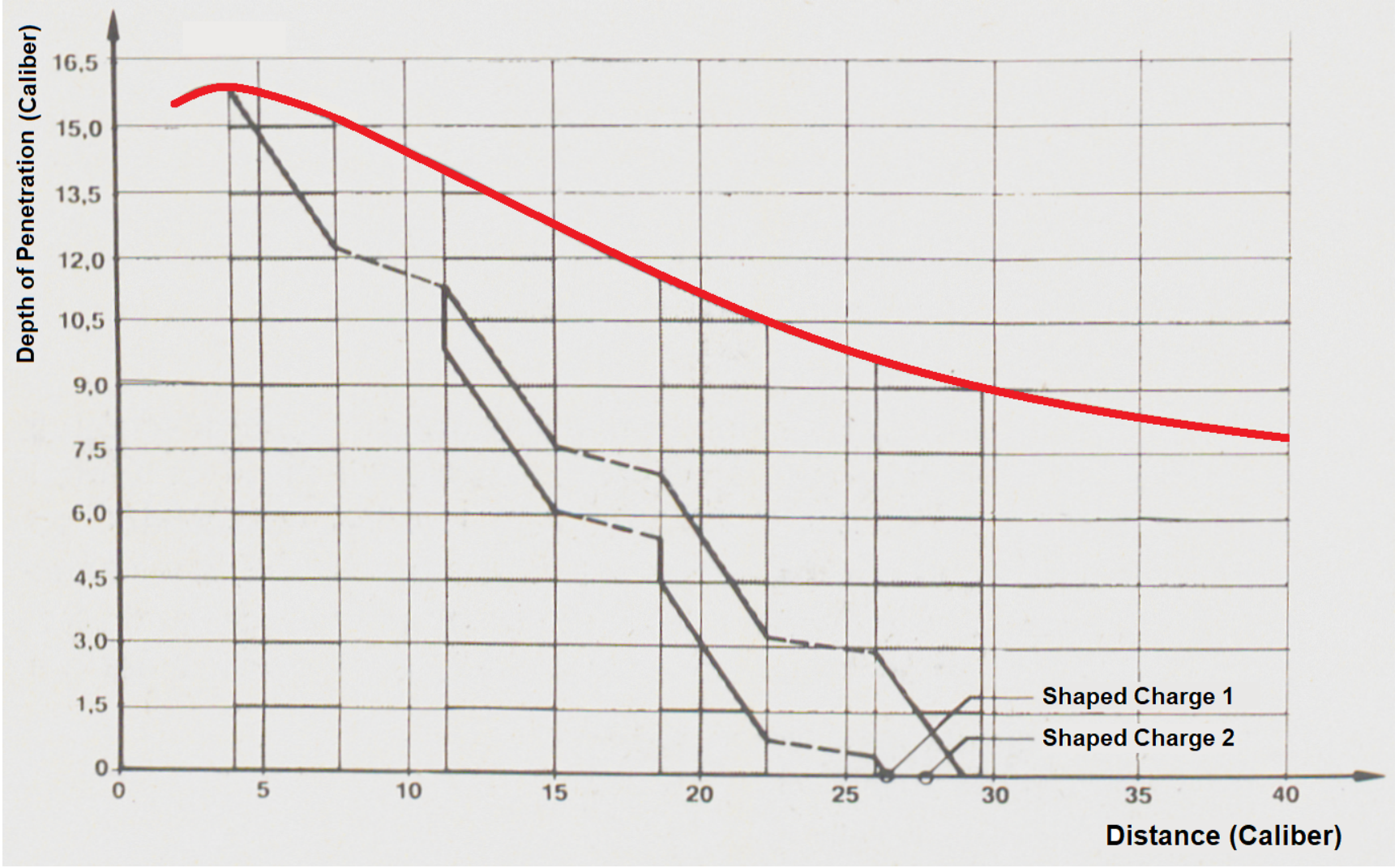

Figure 30: Penetration depth as a function of distance with extended distance curve and determination of the perforation capability of the shaped charge jet against four concrete blocks in bulkhead arrangement according to the proportionality method. This method also agrees quite well with the experimental results of two tests

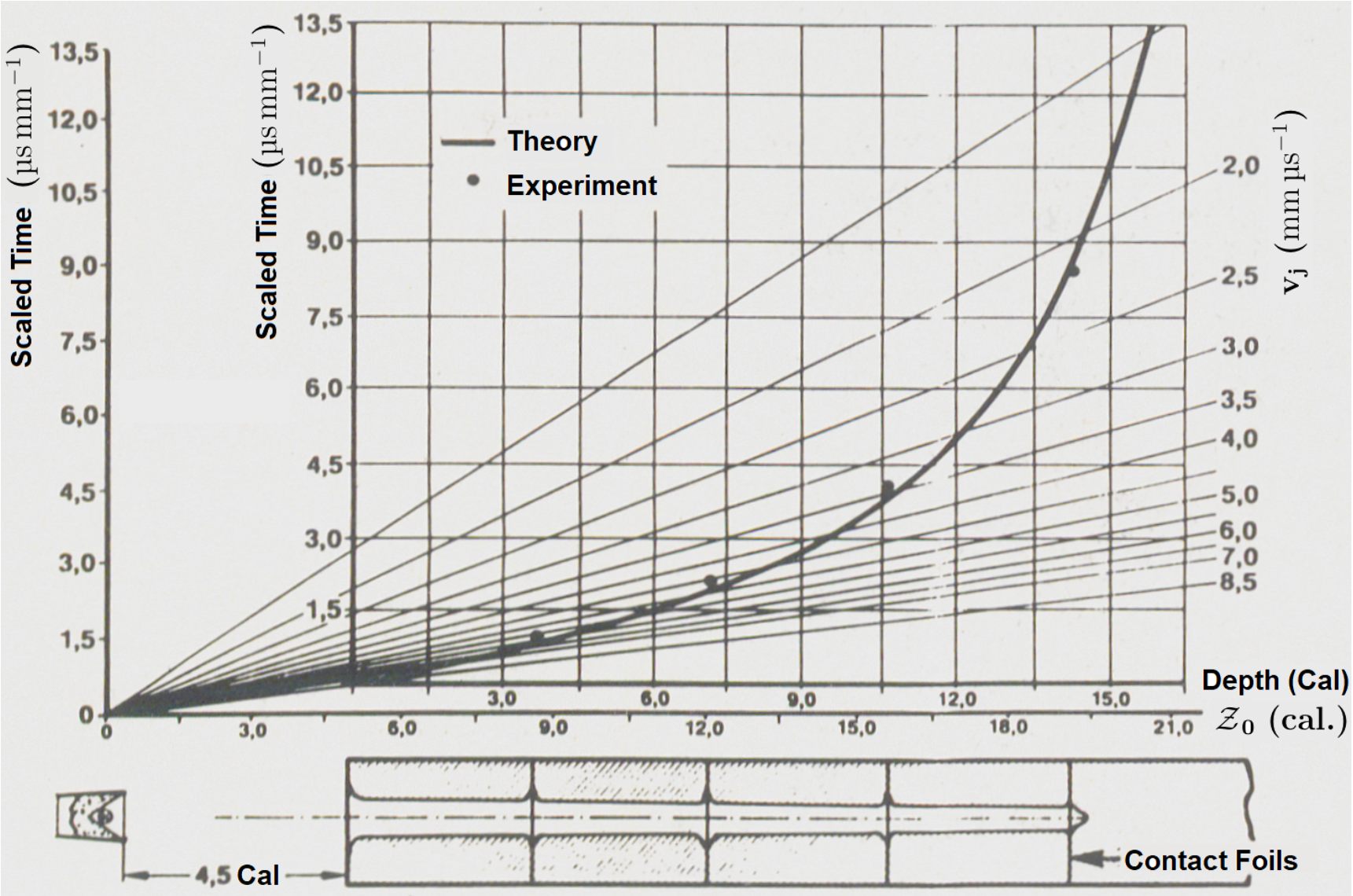

Figure 31: Time-to-distance curve of the crater base formation based on the theoretical prediction (solid bold curve) compared to the four experimental measured values in the solid block after experimental setup according to Figure 23

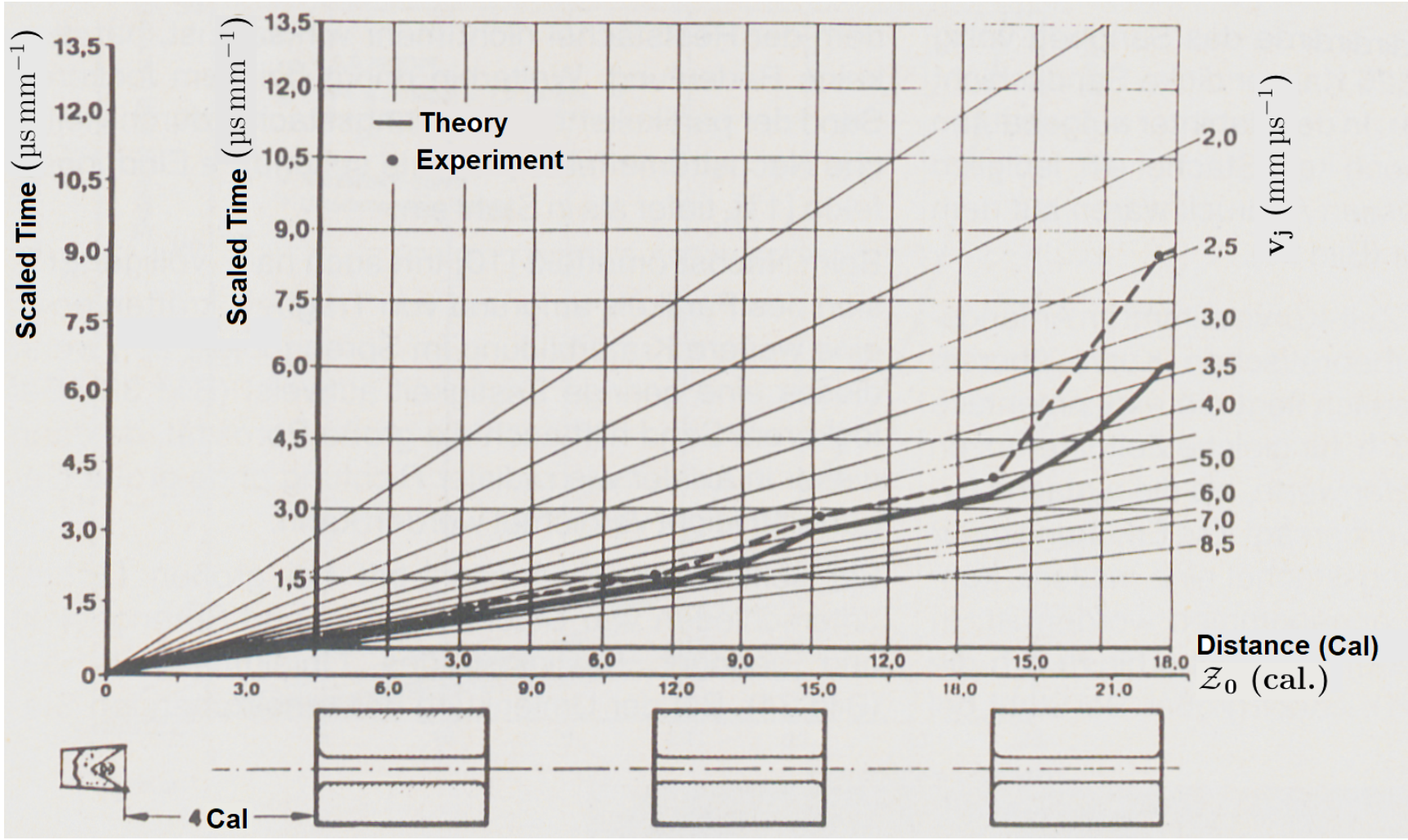

Figure 32: Time-to-distance diagram of the experimentally obtained values compared to the theoretical prediction in a setup with bulkheaded concrete targets (see Figure 29 and Figure 30)

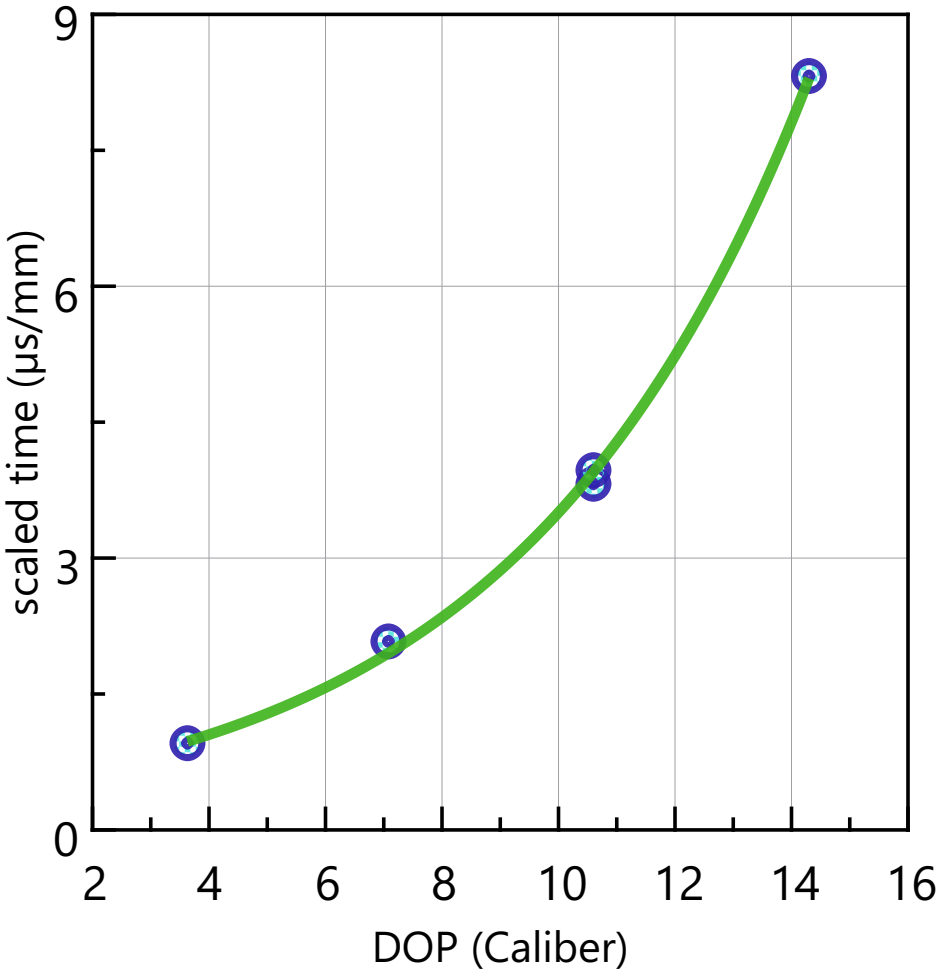

Figure 33: Replotted time-to-distance curve of Figure 31 of the crater base formation with the four experimental measured values in the solid block after experimental setup according to Figure 23

4.2.2 Blast Experiments in Sand

Loosely poured sand with a relatively constant density of $1.3\,\mathrm{g\,cm^{-3}}$ (Figure 35) was blasted with a shaped charge of a slightly different design and different base diameter, whereby both contact and interruption foils were inserted into the sand at each measuring point to record the formation of the crater base. The time differences were measured individually for each measuring point using a so-called logic analyzer. The insulated foils and contact wires were covered with sand (Figure 36) to protect them from the air blast wave and plumes of the detonating explosive charge.

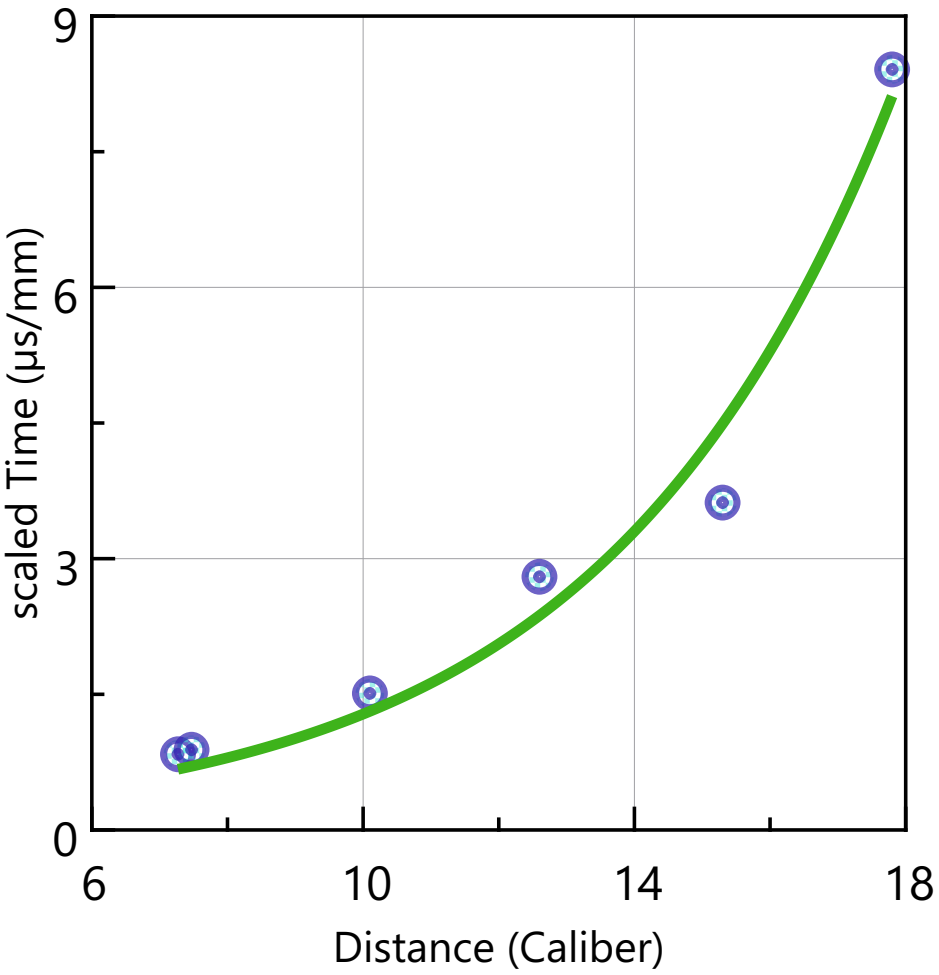

Figure 34: Replotted Time-to-distance diagram of Figure 32 of the experimentally obtained values in a setup with bulkheaded concrete targets (see Figure 29 and Figure 30)

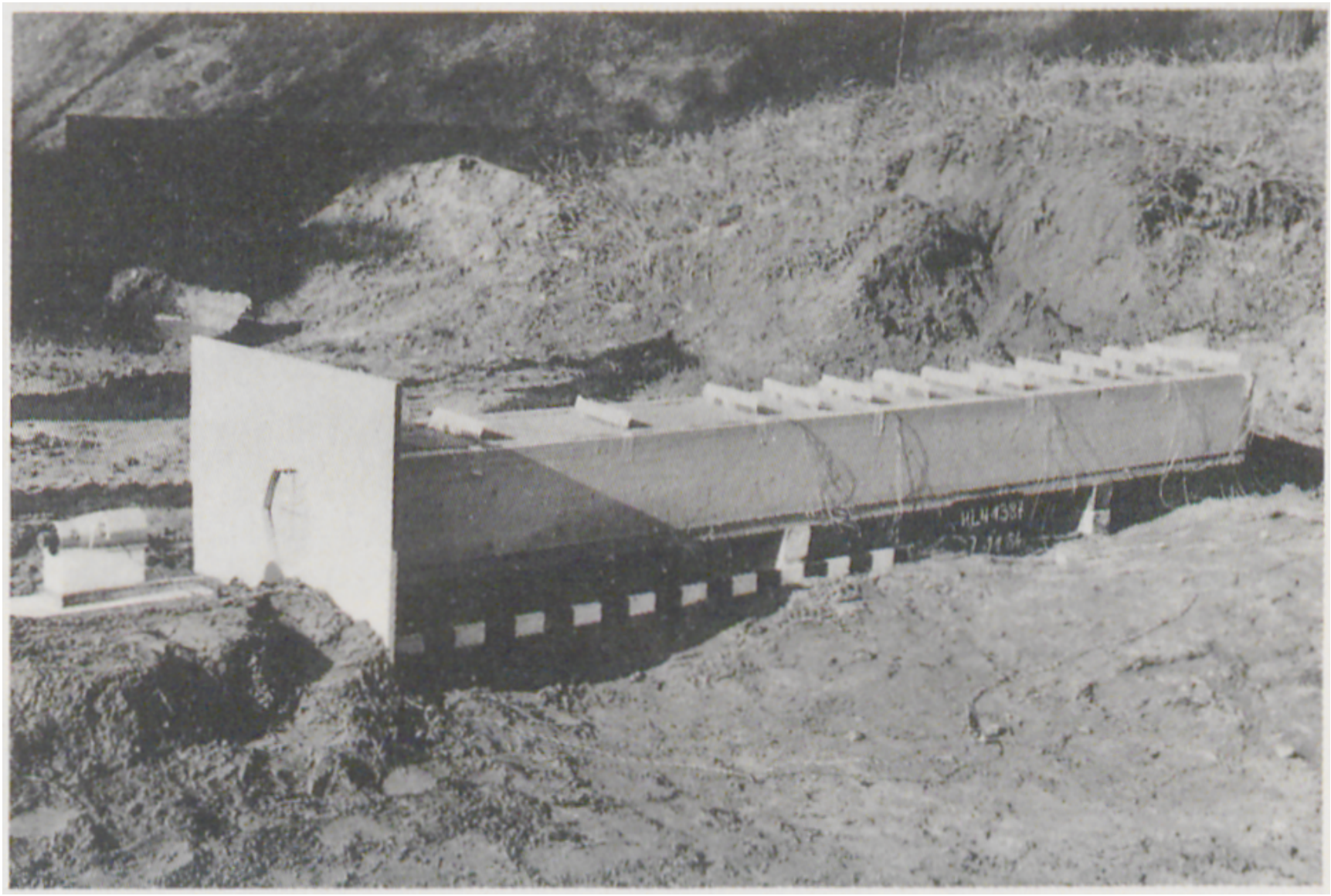

Figure 35: Experimental setup for determining the blasting performance of a shaped charge against sand with contact and interrupter foils, respectively

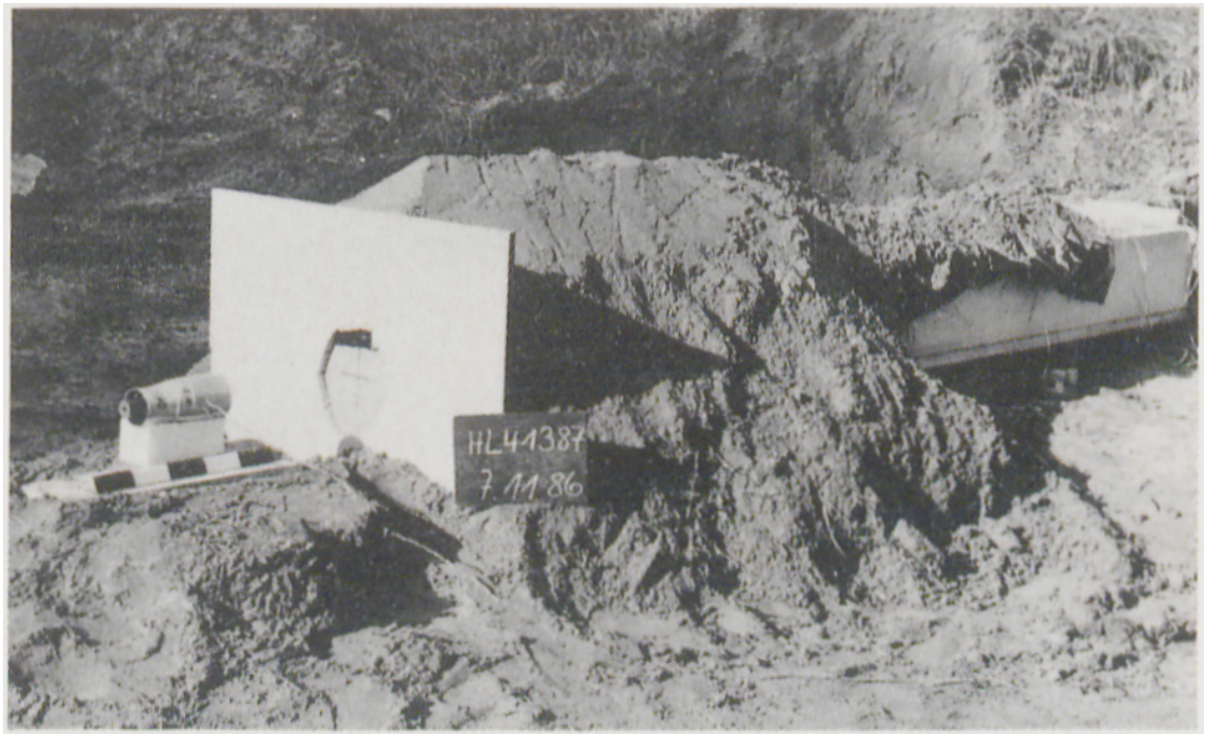

Figure 36: The Experimental setup was covered with sand to protect the contact and interrupter foils, which were used to measure the crater base formation as a function of time

The sand bed was completely destroyed by the jet perforating it (Figure 37) and the 26-caliber-thick layer of sand was also completely perforated. However, no jet entered the soft iron block behind it, only the bolt itself and its imprint were visible on the soft iron block (Figure 38).

The recorded time-to-distance curve corresponds exactly to the theoretical curve at the beginning (see Figure 39), where the experimental values were also as before replotted in Figure 40 to be statistically evaluated. The values can be best approximated by an exponential function that reads

$$\text{DOP} \ = 0.534 \cdot e^{0.112x}$$

with fitting parameters according to Table 10. In the further range, however, the experimental curve is more favorable, i.e. for the same time differences, larger DOP performance values result than the simple hydrodynamic theory predicts. The explanation for this is that an average, constant particulation time has been assumed for the shaped charge jet. In reality, the former increases towards the residual jet, i.e. the residual jet length is actually greater. In the case of steel, where the residual jet is no longer effective, this is of no significance. Furthermore, in the case of loose sand, the particulated shaped charge jet penetrates deeper than in steel due to multiple wake effects, [4], such as secondary penetration effects, [2].

Figure 37: Result of blast experiment

In the case of the wake effect according to [4], further cratering occurs in the blast object even after complete erosion of the particle due to inertial forces if it has low strength (Figure 41). In the case of loose sand, the high porosity also favors this effect, as it can then be easily compacted in the axial and radial direction without great counterforce.

Figure 38: Impression of the impact of the bolt (in the picture above) on the soft iron block after 35 caliber of sand distance. A residual jet no longer had an effect on the target block

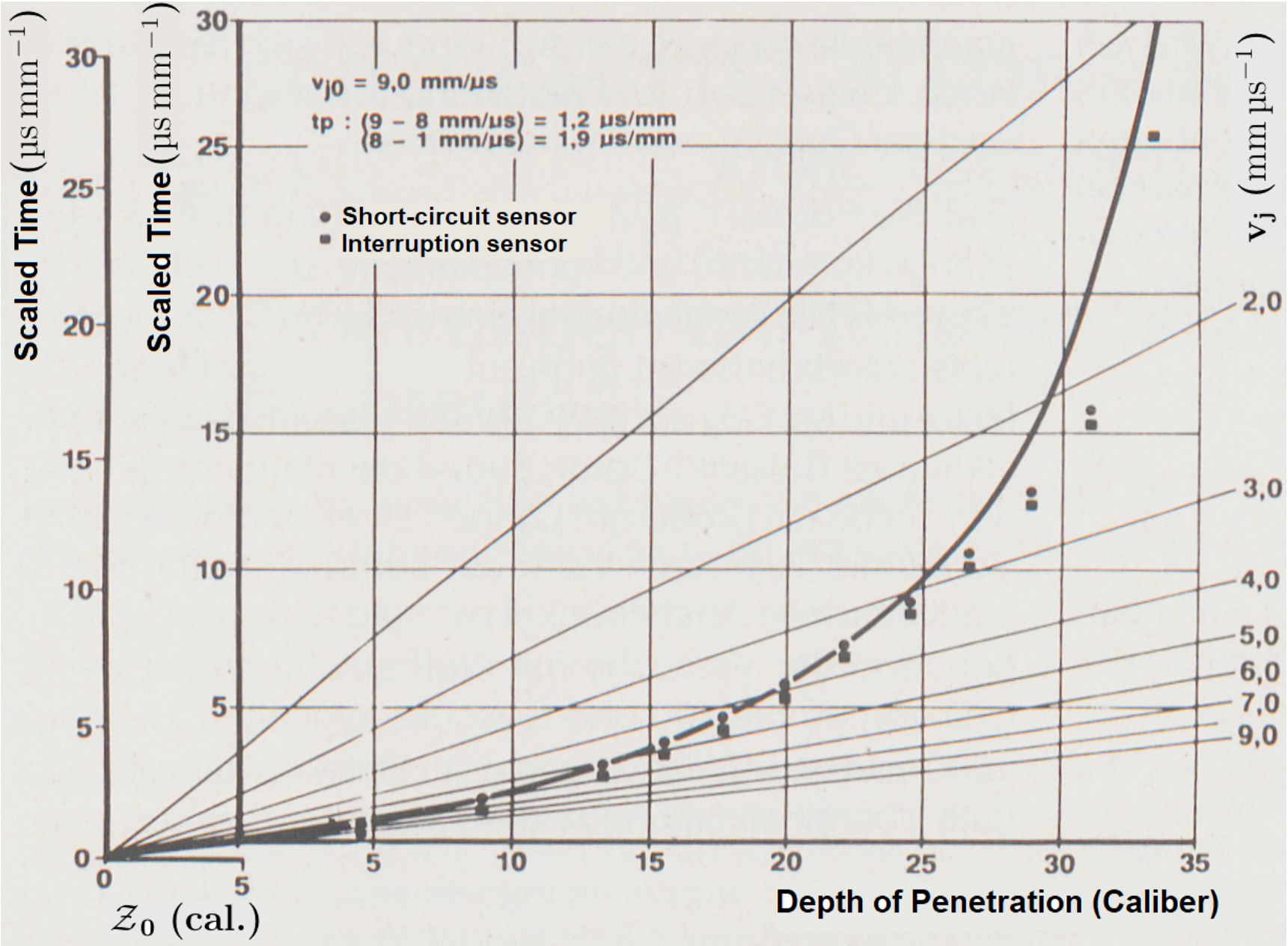

Figure 39: Time-distance diagram of crater base formation for the copper jet in sand, measured with contact and interruption foils

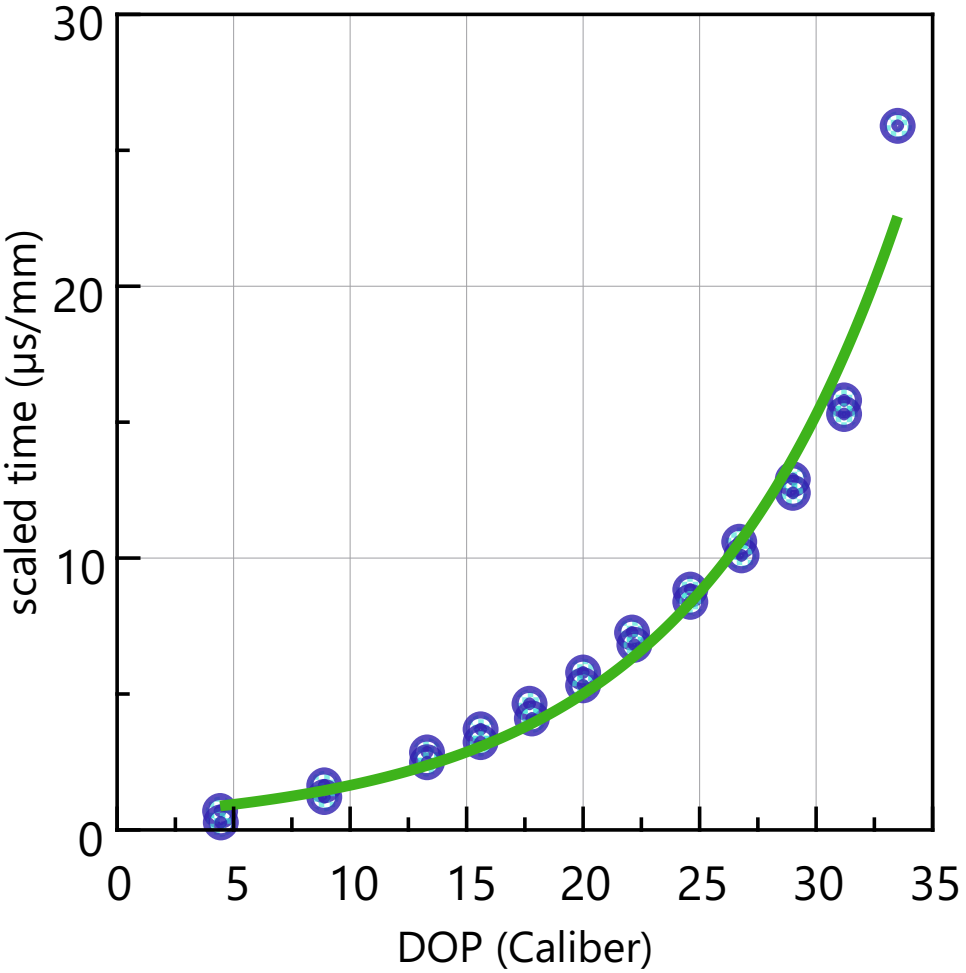

Figure 40: Replotted time-to-distance curve of Figure 39 for the copper jet in sand, measured with contact and interruption foils

Secondary penetration occurs when there are large differences in the density of the barbed material and the blasting object and when the target material exhibits a low strength (Figure 42). When the jet particle flowing in is deflected at the stagnation point of the crater base, a pipe is formed that takes on zero velocity in the laboratory system if the density of the jet and object material is the same. However, if the density of the jet particles is greater in relation to the object density, a velocity u' results for the pipe in the laboratory system according to [2] in the form

$$u' = 2 \cdot u - v_j \,. \tag{94}$$

With the crater base velocity

$$u = \frac{v_j}{(1+\gamma)}$$

according to Equation 7 then also according to Equation 94 there results the expression

$$u' = \frac{(1-\gamma)}{(1+\gamma)} \cdot v_j \,. \tag{95}$$

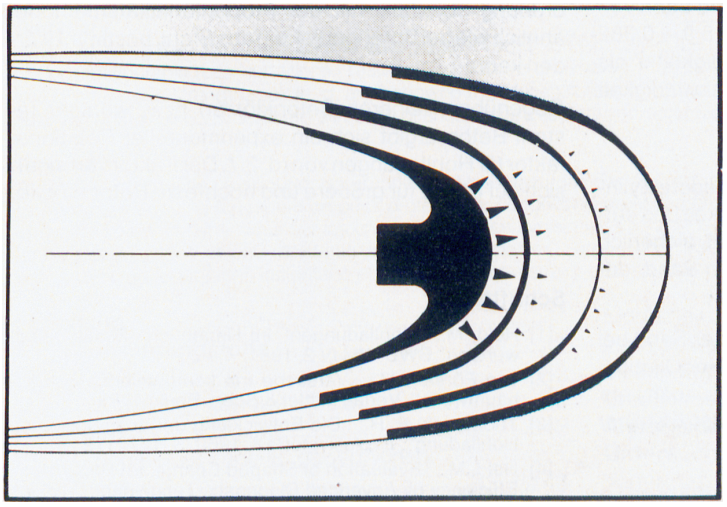

Figure 41: Wake effects during penetration of particles into a blast object, especially with low strength, [4]

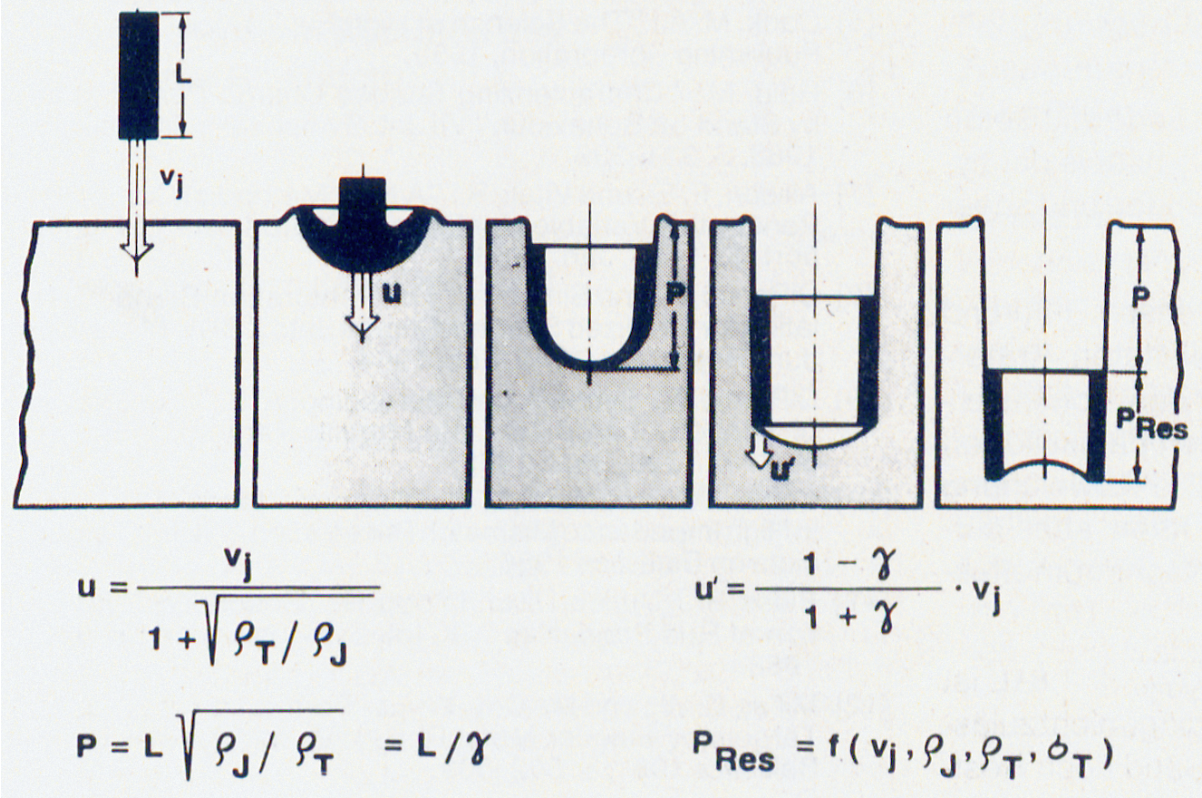

Figure 42: Secondary penetration by the tube formed from a particle during hydrodynamic penetration, which results in additional cratering, especially if there are large differences in density between the particle and the target material and if the target is of low strength, [2]

sum of quadratic errors (χ^2)	24.8236
remaining mean square (χ^2/dof)	1.18207
square root of mean quadratic error (RMSD/SD)	1.08723
coefficient of determination (R^2)	0.969724
corrected coefficient of determination (R^{-2})	0.966697
χ^2-Test ($P > \chi^2$)	0.255
F-Test	673
P > F	0
mean absolute error (MAE)	0.709209
Akaik's information criteria (AIC)	73
Bayesian information criteria (BIC)	76.4

Table 10: Goodness of adaption for plot shown in Figure 40

With the density of copper of $8.9\,\mathrm{g\,cm^{-3}}$ and Sand with a value of $1.3\,\mathrm{g\,cm^{-3}}$ we obtain for

$$\gamma = \sqrt{\frac{\rho_\mathrm{T}}{\rho_j}} = \sqrt{\frac{1.3}{8.9}} = 0.382$$

a constant for the downstream velocity u' as a function of the inflowing jet velocity of

$$u' = 0.45 \cdot v_j\,.$$

This means that the cylinder formed from the jet particle still has about half the velocity of the impacting jet particle. This certainly also leads to additional cratering in sand, which still has practically no strength.

On the other hand, even loosely packed sand at densities of $1.3\,\mathrm{g\,cm^{-3}}$ already consumes the jet of a shaped charge, which can also be seen very clearly from this test result. Just 26 calibers of loose sand are sufficient for this.

5 Summary

The penetration and piercing of sand and concrete with shaped charge jets can be understood and even well predicted using hydrodynamic penetration theory.

The experimentally determined and theoretically derived crater base velocities based on the hydrodynamic theory are in complete agreement for the continuous penetration process and in approximate agreement for the particulated part of the jet. However, the deviation of the particulated penetration behavior can be well understood due to secondary penetration or wake effects.

However, the simple trend formula $\mathbf{P}_m = L \cdot \sqrt{\rho_j/\rho_\mathrm{T}} = 1.8 \cdot L$ is not valid for the transition from steel to concrete, as single residual jet parts are still effective in concrete and especially in sand, which changes the jet length L, but which are not effective in steel, especially high-quality steel.

The work of Miller and Mc Coy shows that the formula $\sqrt{\rho_j/\rho_\mathrm{T}}$ is correct if the projectile length is constant and continuous, i.e. does not exhibit a changing or interrupted length as in the case of a shaped charge jet. These scientists shot, in a way that is called "reverse ballistics", concrete against rods which were kept stationary and with a larger length L to diameter D ratio. This avoids the otherwise occurring and highly disruptive angle of attack. The results of the tests with tungsten bars with a L/D of 40 to 100 and velocities between $1000\,\mathrm{m\,s^{-1}}$ and $4500\,\mathrm{m\,s^{-1}}$ give relatively good average agreement with the root-ρ-law.

Furthermore, it was demonstrated that the DOP performance through concrete blocks in a bulkhead arrangement can also be determined using the proportionality method, similar to that used for steel blast objects.

Compared to smaller concrete blocks or concrete with less strength, the experimental relationship factor for shaped charges is about 2.7. The factor decreases to about 2.2 for larger and high-strength concrete blocks.

References

[1] F. E. Allison and R. Vitali. A New Method of Computing Penetration Variables for Shaped-Charge Jets. Technical Report 1184, Ballistic Research Laboratories, Aberdeen Proving Ground, Maryland, 1963.

[2] S. J. Bless, D. Jurick, and B. Yoon. Secondary Penetration of Rod Projectiles. In *Proceedings of the 9th International Symposium on Ballistics*, pages 345–350, Royal Military College of Science, Shrivenham, UK, 1986.

[3] M. A. Cook. *The Science of High Explosives*. Reinhold Publishing Corporation, New York/London, 1st edition, 1958.

[4] I. G. Cullis and M. A. Nash. The Importance of Afterflow in High Impedance Mismatch Penetration. In *Proceedings of the 9th International Symposium on Ballistics*, Royal Military College of Science, Shrivenham, UK, 1986.

[5] R. DiPersio and J. Simon. The Penetration-Standoff Relation for Idealized Shaped Charge Jets. Technical Report Memorandum Report 1542, Ballistic Research Laboratories, Aberdeen Proving Ground, Maryland, 1964.

[6] R. DiPersio, J. Simon, and A. Merendino. Penetration of Shaped-Charge Jets into Metallic Targets. Technical Report 1296, Ballistic Research Laboratories, Aberdeen Proving Ground, Maryland, 1965.

[7] M. Förster. *Versuche mit komprimierter Schießbaumwolle*. Verlag Mittler & Sohn, Berlin, 1st edition, 1883.

[8] M. Held. Evaluation of Shaped Charge Jet Penetration Efficiency by Advanced Diagnostic Techniques. In *Proceedings of the 6th International Symposium on Ballistics*, pages 480–493, Orlando, Florida, USA, 1981.

[9] M. Held. *Hohlladungen*. Bundesamt für Wehrtechnik und Beschaffung, Waffen und Munitionstechnik IV 2, Koblenz, Germany, 1981.

[10] M. Held. Characterizing Shaped Charge Performance by Stand-off Behaviour. In *Proceedings of the 7th International Symposium on Ballistics*, pages 331–339, Den Haag, Netherlands, 1983.

[11] MIT Libraries. `https://libraries.mit.edu/150books/2011/04/19/1963/1963-cross-section/`.

[12] F. R. Thomanek. Die Entwicklung der ausgekleideten Hohlladung. *Explosivstoffe, Zeitschrift für das Spreng-, Schieß-, Zünd-, Brand- und Gasschutzwesen*, 8:177–179, 1960.

[13] ToughSF. `https://toughsf.blogspot.com/2017/05/nuclear-efp-and-heat.html`.

[14] W. Walters. Introduction to Shaped Charges. Technical Report ARL-SR-150, Army Research Laboratory, 2007. `https://apps.dtic.mil/sti/pdfs/ADA469696.pdf?trk=public_post_comment-text`, page 5.

[15] Y. Wang, J. Yin, X. Zhang, and J. Yi. Study on Penetration Mechanism of Shaped-Charge Jet under Dynamic Conditions. *Materials (Basel)*, 15:1–15, 2022.